Title

Enhanced Stability of Nanocrystalline Metals with Amorphous Grain Boundary Complexions via Compositional Manipulation

Permalink

https://escholarship.org/uc/item/3qd5b297

Author

McDevitt, Charlette Grigorian

Publication Date

2020

Peer reviewed|Thesis/dissertation

UNIVERSITY OF CALIFORNIA,
IRVINE

Enhanced Stability of Nanocrystalline Metals with Amorphous Grain Boundary Complexions via Compositional Manipulation

DISSERTATION

submitted in partial satisfaction of the requirements
for the degree of

DOCTOR OF PHILOSOPHY

in Chemical and Biomolecular Engineering

by

Charlette Grigorian McDevitt

Dissertation Committee
Professor Timothy J. Rupert, Chair
Professor Martha Mecartney
Professor Julie Schoenung

2020

COPYRIGHT

Sections of this dissertation have been previously published and are re-used here with appropriate permissions:

DEDICATION

I dedicate this thesis to my family. You are my greatest inspiration and motivation, and the hardest working people I know. Without your endless encouragement and love, I would not be the person I am today.

TABLE OF CONTENTS

LIST OF TABLES

LIST OF FIGURES

ACKNOWLEDGMENTS

First, I would like to thank my advisor, Professor Timothy Rupert, for being a constant source of support and guidance throughout my doctoral studies. He has truly challenged me to become more inquisitive and creative in my approach to research. His dedication and passion for his work is contagious, and has motivated me to persevere through several difficult research problems. I could not ask for an advisor who is more supportive, understanding, and inspiring.

I would like to thank my thesis committee members, Professor Schoenung and Professor Mecartney. Their insight and constructive criticism throughout the development of this thesis has been invaluable. I would also like to thank the staff at LEXI and IMRI for their training on a variety of characterization techniques, and for taking the time to help me improve my own microscopy skills. My labmates in the Rupert research group have helped to make my time in graduate school so enjoyable, whether we were chatting about our days, or having in-depth discussions about our research ideas. I will sincerely miss working with such a fun group of people every day.

CURRICULUM VITAE

Charlette Grigorian McDevitt

2015 B.S. in Chemical Engineering, University of California, Riverside

2017 M.S. in Chemical and Biochemical Engineering, University of California, Irvine

2020 Ph.D. in Chemical and Biomolecular Engineering, University of California, Irvine

PUBLICATIONS

Grigorian CM, Rupert TJ. “High entropy complexions: Stabilizing nanocrystalline grains with thick amorphous complexions” (In preparation)

Grigorian CM, Rupert TJ. “Estimation of critical cooling rates for amorphous-to-ordered complexion transitions in nanocrystalline alloys” (Submitted to *Acta Materialia*)

Zhou X, Schuler JD, **Grigorian CM**, Tweddle D, Rupert TJ, Li L, Thompson GB. “Comparison of Solute Partitioning between Nanocrystalline Thin Films and Ball Milled Cu(Zr)” *Journal of Materials Science* (2020) In Press.

Schuler JD, **Grigorian CM**, Barr CM, Hattar K, Boyce BL, Rupert, TJ. “Amorphous intergranular films mitigate radiation damage in nanocrystalline Cu-Zr.” *Acta Materialia* (2020) 1-14

Grigorian CM, Rupert TJ. “Thick amorphous complexion formation and extreme thermal stability in nanocrystalline Cu-Zr-Hf alloys” *Acta Materialia* (2019) 172-182.

Balbus GH, Echlin MP, **Grigorian CM**, Rupert TJ, Pollock TM, Gianola DS. “Femtosecond laser rejuvenation of nanocrystalline metals” *Acta Materialia* (2018) 156-183

PRESENTATIONS

Grigorian CM, Rupert TJ. “Thick Amorphous Complexions Enabled by Compositional and Thermal Manipulation” TMS 2020, San Diego, CA. February 2020.

Grigorian CM, Rupert TJ. “Extreme Thermal Stability in Ternary Nanocrystalline Cu-Zr-Hf and Cu-Zr-Al Alloys with Amorphous Complexions” MS&T 2018, Columbus, OH. October 2018.

ABSTRACT OF THE DISSERTATION

Enhanced Stability of Nanocrystalline Metals with Amorphous Grain Boundary Complexions via Compositional Manipulation

by

Charlette Grigorian McDevitt

Doctor of Philosophy in Chemical and Biomolecular Engineering

University of California, Irvine, 2020

Associate Professor Timothy J. Rupert, Chair

The implementation of nanocrystalline metals is of growing interest in a variety of applications due to the enhancement of mechanical properties with the reduction of grain size. However, the significant grain boundary volume in these materials is associated with thermal instability and a lack of ductility. Recent studies have focused on manipulating the grain boundary structure and chemistry in an attempt to address these issues. Grain boundary complexions describe interfacial phases which exist in equilibrium only with their abutting phases. Amorphous complexions, in particular, have been previously proven to improve the thermal stability of binary nanocrystalline alloys, while simultaneously improving their ductility due to their great capacity for dislocation absorption. However, this type of complexion is only stable at high temperatures and requires very high quench rates to be retained in the microstructure during cooling, limiting the practicality of these materials for use in lower temperature applications. Investigating the formation of these interfacial phases is also of particular interest in multicomponent alloys, as most alloys used in engineering applications are composed of more than two elements.

In this thesis, we seek to improve the utility of nanocrystalline metals by manipulating the composition of the amorphous grain boundary complexion in order to maximize their thickness and stability against transformation to ordered grain boundaries upon cooling. First, the formation of thick amorphous intergranular films is demonstrated in nanocrystalline ternary alloys. Hf additions to a binary Cu-Zr alloy are shown to contribute to the thermal stability of the alloy, while also facilitating the formation of thicker amorphous complexions than the binary analogs. The concept of developing materials with high-entropy complexions is also explored, with further improvements to thermal stability and complexion thickness shown in a Cu-Zr-Hf-Nb-Ti alloy. Finally, the influence of grain boundary composition on complexion transformations is investigated. We find that ternary alloy compositions form amorphous complexions which are more stable against transformation to thinner or ordered grain boundaries than binary alloys, reducing the critical cooling rate necessary to retain the equilibrium structure at high temperatures and therefore improving the potential for their use in lower temperature applications. In summary, we find that careful alloy design can lead to the formation of thick amorphous complexions which are stable against transitioning upon cooling, which can further improve the mechanical properties and enhance the utility of nanocrystalline metals.

1 Introduction

1.1 Introduction to Nanocrystalline Metals

The study of nanocrystalline metals has recently generated significant research interest due to interesting properties compared to their coarse-grained counterparts. With a reduction in grain size below 100 nm, mechanical properties such as high yield strength [1] and hardness [2] are dramatically improved. Nanocrystalline metals have shown also desirable chemical and physical properties such superior resistance to corrosion [3] and irradiation [4]. The enhancement of these properties is attributed to the high volume of grain boundary material associated with the reduction of grain size. The relation between grain boundary volume and grain size can be described by

$$V_{gb} = 1 - \left(\frac{d - t}{d}\right)^3$$

where V_{gb} is the grain boundary volume, d is the average grain size, and t is the grain boundary thickness [5]. Figure 1-1 plots the volume fraction of both grain boundary material and material found at the grain interior assuming a grain boundary thickness of 1 nm.

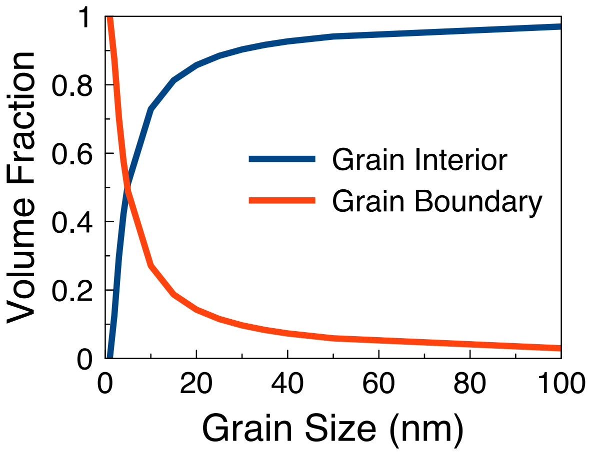

Figure 1-1: Plot of grain and grain boundary volume as a function of grain size [5]. The volume of grain boundary material present within a microstructure increases drastically within the nanocrystalline grain size regime.

Of the enhanced properties of nanocrystalline metals listed above, perhaps the most notable and well-studied is the significant increase in strength with reduction in grain size. The Hall-Petch equation [6, 7],

$$\sigma_y = \sigma_0 + \frac{k}{\sqrt{d}}$$

where σ_y is the yield stress, d is the grain diameter, and k and σ_0 are material-dependent constants, describes this behavior. The strengthening of a material with a reduction in grain size occurs due to the presence of a high number of grain boundaries, which act as a barrier to dislocation motion. Figure 1-2 demonstrates this effect in pure Ni, where the open circles represent yield strength measurements measured using compression or tension tests, while the closed circles represent strength values calculated from hardness values obtained by Vickers and nanoindentation hardness testing, divided by a Tabor factor of 3 [8, 9].

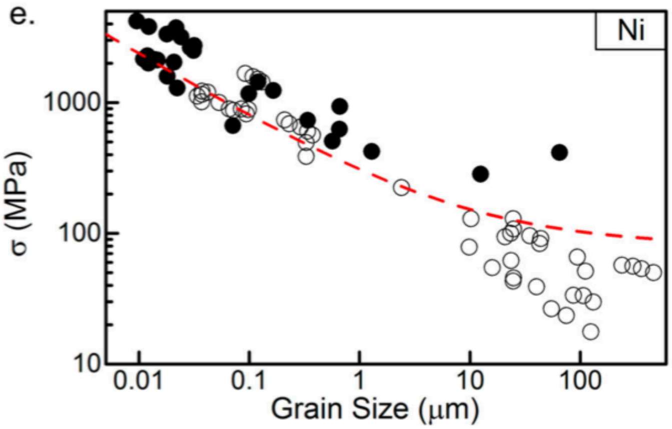

Figure 1-2: Hall-Petch behavior in Ni, demonstrating an increase in strength with reduction in grain size. Data represented by open circles were obtained by compression or tension tests, while full circles are calculated from hardness tests. [8]

Although nanocrystalline metals are extremely strong [1, 10], they are commonly plagued by two major problems: (1) poor thermal stability and (2) limited ductility. The characteristically large volume fraction of grain boundaries in nanocrystalline metals has excess energy, providing a large driving force for grain growth [11]. Significant grain growth at temperatures well below those typically required for materials processing (e.g., powder consolidation or sheet-metal forming) has been reported [12, 13], with some studies even reporting coarsening at room temperature [14-16].

In addition, nanocrystalline metals are usually much more brittle than coarser-grained metals [1, 17]. This issue has been traced to the fact that dislocations must be nucleated and absorbed at grain boundaries, which can eventually lead to crack nucleation at relatively small plastic strains [18, 19]. In order for nanocrystalline metals to be fully utilized in applications which may benefit from their enhanced properties, the issues of microstructural instability and lack of ductility must be addressed. Ideally, one would like to find a solution that can resolve both of these persistent issues simultaneously.

1.2 Improving the Thermal Stability of Nanocrystalline Metals

The thermal stability of nanocrystalline metals can be enhanced by using dopant elements that segregate to grain boundaries to reduce the grain boundary free energy, thereby reducing the driving force for grain growth. Weissmuller first proposed the deliberate segregation of solute atoms to the grain boundaries as a method of improving thermal stability in order to reduce the excess grain boundary energy to zero [20]. More recently, Polyakov et al. showed that a sputtered Hf-Ti alloy retained an average grain size of 50 nm after annealing for 96 h at 800 °C due to the segregation of Ti to the grain boundaries [21]. Similarly, Chen et al. demonstrated that the segregation of C in ball milled Fe-C alloys improved thermal stability and helped to maintain grain sizes under 15 nm after annealing for 1 h at 573 K [22]. These studies agree on the effect of the dopant atoms on thermal stability but provide limited criteria for selecting this chemistry. These criteria were addressed generally by Murdoch and Schuh, who developed an approach for calculating segregation enthalpies of many binary alloy systems, allowing for a general estimation of whether a dopant alloy will segregate to the grain boundary [23]. In addition, stability maps developed by Darling et. al. determine, for a given grain size and temperature, the minimum solute concentration required to reduce grain boundary free energy to zero [24]. While manipulating the chemistry of grain boundaries has led to marked improvements to thermal stability, this phenomenon alone is not likely to significantly affect the ductility of nanocrystalline materials.

Kinetic approaches to prevent grain growth in nanocrystalline metals include mechanisms such as Zener pinning [25-27] or solute drag [28-30], where the limited mobility of a second phase between crystallites prevents excessive grain boundary motion. It is not uncommon for microstructures to simultaneously be stabilized both thermodynamically and kinetically through the addition of segregating dopant elements, where both grain boundary segregation and the formation of second phase particles which pin grain boundaries are observed [31-33]. While these methods have been proven to limit grain growth in nanocrystalline metals, the inherent lack of ductility characteristic of these materials remains an issue.

1.3 Grain Boundary Complexions

A potential solution to both the limited thermal stability and ductility inherent to nanocrystalline metals is to also consider the effects of grain boundary structure. Recently, characterization and classification of atomic structure at grain boundaries has generated detailed models and an understanding of how these important properties are influenced, especially in ceramics [34-36]. The recent classification and characterization of grain boundary complexions, also termed grain boundary phases by some researchers [37-40], have helped elucidate previously unexplained phenomena in materials science. Grain boundary complexions are phase-like interfacial structures which exist in thermodynamic equilibrium with their abutting phases [34, 35]. Dillon et al. classified six different types of grain boundary complexions originally found in undoped and doped alumina systems, varying in thickness as well as structural and chemical disorder and illustrated in Figure 1-3: (a) single layer segregation (type I), (b) clean grain boundary (type II), (c) bilayer segregation (type III), (d) multilayer segregation (type IV), (e) nanoscale intergranular films (type V), and (f) wetting films (type VI). However, a greater number of complexion types have been hypothesized given the various degrees of freedom available in a grain boundary [34]. Complexions can be classified by their composition, i.e. whether they form in a pure system where the complexion composition matches that of the bulk, or whether they form in systems which have been exposed to impurities or purposefully doped, creating a difference in composition between the grain boundary phase and bulk phase. Additionally, they can be characterized by the presence or lack of long-range compositional or chemical order.

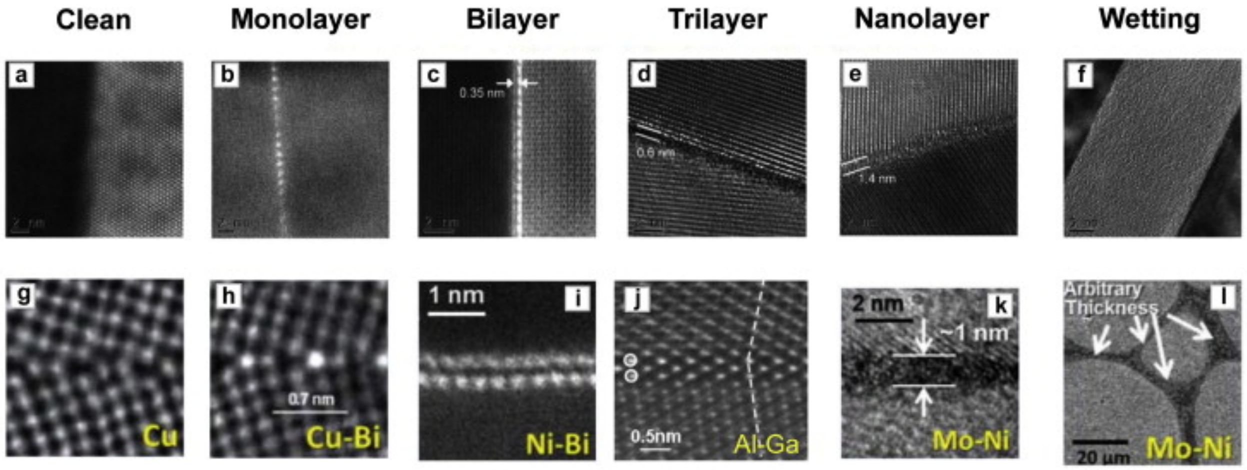

Figure 1-3: Grain boundary complexions found in silica-doped alumina samples and various binary alloys, in order of increasing thickness and disorder. [36]

Several recent studies have focused on the effects of certain complexion types on the densification of materials as the first step in utilizing complexions in the possible retention of a desired microstructure and bulk properties [41-43]. One such study investigated the densification of alumina-zirconia composite ceramics found that the addition of trace titania led to the formation of grain boundary liquid phases through Ti segregation to grain boundaries, fitting the Dillon-Harmer description of a type V complexion [44]. Composites doped with titania were reported to undergo significantly enhanced densification compared to those composites with undoped grain boundaries, a type II complexion.

Transitions between these different complexion types are also possible [45, 46], enabling control of the dominant complexion type in a microstructure, which in turn determines material properties [47-49]. For example, the fracture toughness of alumina with ordered complexions is greater than alumina doped with yttria, which is prone to disordered complexions and an associated embrittlement of grain boundaries [50]. An understanding of complexion transitions is necessary to gain an understanding of previously unexplained phenomena, such as abnormal grain growth [49, 51]. Transitions between complexion types can be triggered by changes in grain boundary chemistry, pressure, and temperature [34, 52]. Excess free energy associated with a particular complexion, $\boxed{\gamma}$, plays an important role in determining the dominant complexion and the associated transitions between these structures. Through these transformations, a system can approach its minimum energy, i.e. if $\gamma^{\beta} > \gamma^{\alpha}$, then complexion α will be considered the equilibrium complexion type [34] and species beta will transform to this structure. Grain boundary structures can exist in thermodynamic equilibrium if they have the same free energy, i.e. $\gamma^{\beta} = \gamma^{\alpha}$ [34, 52, 53]. Computational and experimental studies have demonstrated that complexion types of greater structural disorder such as amorphous complexions are stable at high temperatures, and below a particular grain boundary energy, a transition from an ordered to disordered complexion, or grain boundary premelting, will not occur [54]. Additionally, due to the effects of anisotropy in grain boundary energy, transitions between different complexion types are not immediate and do not occur simultaneously at all grain boundaries [41]. Efforts to further the understanding of complexion transitions have been taken, with the most notable being the development of grain boundary complexion diagrams in order to predict the conditions at which these transitions will take place. Figure 1-4 shows one such example of a grain boundary complexion diagram developed for a Ni-Bi alloy, which was developed using density functional theory calculations and was proven experimentally to accurately predict the grain boundary complexion present [55].

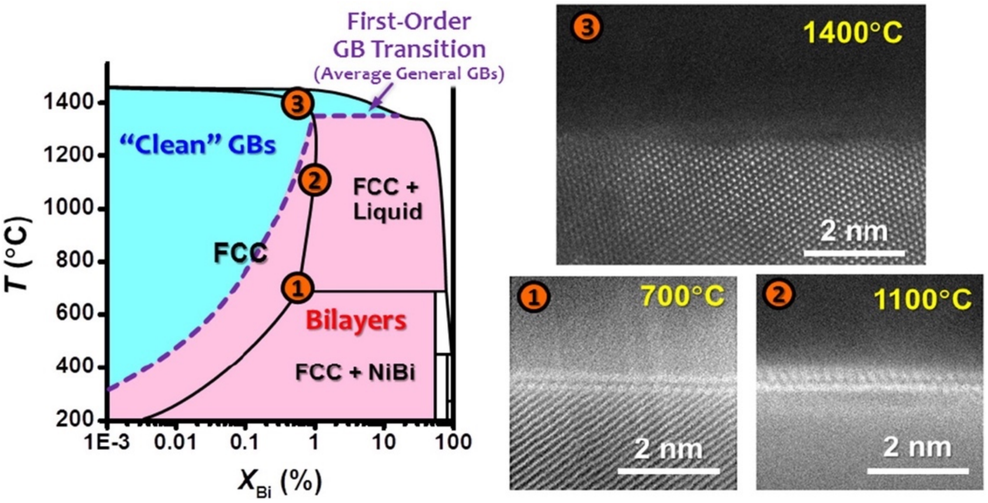

Figure 1-4: A grain boundary complexion diagram for a Ni-Bi alloy, with scanning transmission electron microscopy (STEM) images verifying the predicted grain boundary phase at each composition and temperature [55].

The kinetic aspects of complexion transitions are better understood through time-temperature-transformation (TTT) diagrams [55, 56]. Exact characteristics regarding complexion transitions, for example, temperatures at which discrete complexion transitions occur in a given alloy, or critical cooling rates necessary to avoid a particular complexion transition, are largely unknown or loosely defined. A study by Cantwell et al. explored the formation of complexion TTT diagrams by carefully observing grain growth kinetics in Y_2O_3 co-doped with Er and Yb [56].

The onset of abnormal grain growth during sintering was used as a marker of the occurrence of a complexion transition, and was investigated at a variety of sintering temperatures and times in order to construct a TTT diagram for the complexion transition. A deeper understanding of the specifics of complexion transitions is crucial in order to enable the fine-tuning of material properties through grain boundary structure.

1.4 Amorphous Complexions in Nanocrystalline Metals

Amorphous complexions form and are thermodynamically stable at elevated temperatures where a premelting transition occurs at grain boundaries [57, 58]. In contrast, ordered boundary structures are preferred at low temperatures. While amorphous complexions were first discovered in ceramic systems [43, 59-62], their formation in a variety of binary metallic alloys has been demonstrated recently, including Mo-Ni [63], W-Ni [64], Ni-W [65], Cu-Bi [66], Ni-Zr, Cu-Zr, and Cu-Hf [67]. Schuler and Rupert have developed rules to predict complexion evolution, highlighting the tendency of dopant elements with a positive enthalpy of segregation and negative enthalpy of mixing in their parent phase to form thick amorphous complexions [67]. This is analogous to bulk metallic glass (BMG) formation guidelines, which benefits especially from three or more elements, a negative heat of mixing, and an atomic size mismatch greater than 12% [68, 69]. The positive enthalpy of segregation ensures that dopant elements will segregate to grain boundaries, while the negative enthalpy of mixing is necessary to prevent the precipitation of a second phase throughout the microstructure. Large atomic size mismatches, as well as the addition of multiple dopant elements, may also be beneficial in frustrating the crystallization of the amorphous complexion upon cooling from high temperatures.

The formation of amorphous complexions in nanocrystalline metals may allow for the issues of thermal stability and low ductility to be addressed simultaneously. The effect of amorphous complexions on nanocrystalline metal properties was first observed in nanocrystalline Cu-Zr alloys created by ball milling, with these materials displaying superior hardness, strength, and ductility [70, 71] compared to undoped nanocrystalline Cu [72, 73]. This Cu-Zr alloy was also reported to retain an average grain size of 54 nm even after a week of annealing at 98% of the solidus temperature, as illustrated in Figure 1-5. The findings described above demonstrate the capacity for amorphous complexions to both stabilize the microstructure and improve ductility in nanocrystalline metals.

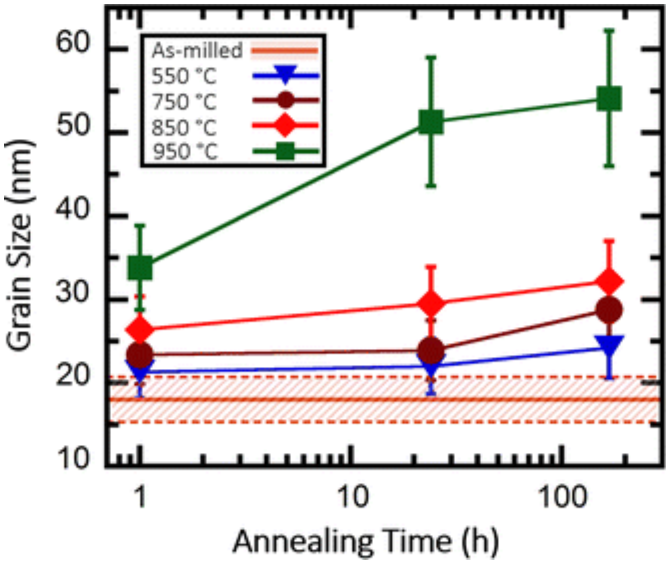

Figure 1-5: XRD grain sizes vs. annealing time for Cu-3Zr alloys containing amorphous complexions. [71]

In addition to improving the thermal stability and ductility of nanocrystalline metals, amorphous complexions have also been proven to impart further improvements to the strength of metals. A study by Zhao et al. [74] demonstrated an increase in the strength of a Cu-Zr alloy associated with an increase in the concentration of Zr in the alloy, due to the formation of a greater number of amorphous-crystalline interfaces. Molecular dynamics simulations by Turlo et al. [75] suggest that the increased strength of nanocrystalline metals with amorphous complexions enhances the dislocation pinning effect of grain boundaries due to the presence of areas of reduced stress, increasing the stress required for dislocation propagation.

Thick amorphous grain boundary complexions are of particular interest in nanocrystalline metals due to their ability to improve thermal stability with reduced grain boundary energy and a smaller driving force for grain growth [65, 71, 76]. Activated sintering is also observed in materials containing amorphous complexions, due to the enhanced diffusion which takes place with this type of grain boundary complexion [42, 77-79]. Prior work by Donaldson and Rupert has shown that amorphous complexions create fully dense bulk nanocrystalline samples through activated sintering while maintaining enhanced thermal stability from the grain boundary phase [79]. These amorphous complexions have also been shown to improve resistance to radiation effects by limiting the size and number of defect clusters formed during irradiation [80, 81]. It is desirable to sustain very thick amorphous complexions within a material's microstructure due to their ability to enable unique mechanical properties – for example, the ability of an amorphous complexion to absorb dislocations, and consequently increase a materials toughness, has been shown via molecular dynamics simulation by Pan and Rupert to increase with increasing amorphous complexion thickness [18].

The stability of these amorphous grain boundary phases is of particular interest, as well as the processing necessary to lock in the high temperature grain boundary structure. To maintain amorphous complexions at ambient conditions and their associated benefits, a material should be quenched such that the high temperature structure is stabilized at standard conditions. This presents a practical impediment to widespread deployment of materials with grain boundary enhanced properties. Additionally, it is of interest to develop materials with very thick amorphous grain boundaries in order to maximize the dislocation absorption capability and microstructural stabilization capacity. An important consideration is that alloys developed to form amorphous complexions do not typically form them at every single grain boundary within a given microstructure, so careful alloy selection may also allow for the development of an alloy in which all grain boundaries are amorphous.

While the vast majority of studies on amorphous complexions focus on their formation in binary alloys, there are demonstrated benefits in the literature associated with incorporating additional dopant elements. The Gibbs adsorption theory [82],

$$d\gamma_{GB} = S^{XS}dT - \sum_i \Gamma_i d\mu_i$$

where γ_{GB} is the grain boundary energy, S^{XS} is the entropy, T is the temperature, Γ is the amount of adsorption, and μ is the chemical potential, implies that a reduction in the grain boundary energy can be achieved through the addition of multiple dopant elements at grain boundaries. A study by Zhou and Luo found that alloys with high-entropy grain boundary compositions, which are generally comprised of four or more constituent elements, tend to retain nanocrystalline microstructures at high temperature longer than Ni-based binary counterparts [83]. These authors hypothesized that the greatly enhanced thermal stability of these alloys is due to high-entropy grain boundary complexions, allowing for greater reduction of GB energy at higher temperatures [84]. Experimental and computational studies from Zhou and Luo have also shown that multicomponent alloys enable activated sintering due to the increased disorder at the GB caused by co-segregation of dopant atoms [85].

The segregation of multiple dopant elements is expected to also improve the stability of amorphous complexions by enhancing their resistance to phase transition in a manner similar to BMGs. BMGs are similarly unstable under ambient conditions and we may draw parallel strategies from their processing to stabilize amorphous complexions. Increasing the number of constituent elements used to form bulk metallic glasses has been proven to enhance their stability against crystallization upon cooling in multiple studies [86-90]. A study by Men et al. demonstrates this behavior in CuZr-based BMGs, where the addition of Ti decreased the glass transition temperature, T_g, from 670 K to 640 K [91]. Amorphous complexion formation has been qualitatively investigated in a variety of binary and multicomponent alloys, however, the resistance to amorphous-to-ordered complexion transitions has not yet been compared across chemistries. Therefore, a thorough understanding of this transformation and the dependence on GB chemistry is necessary to enable the formation of thick and stable amorphous complexions in bulk materials, in addition to their utilization in a variety of conditions.

1.5 Problem Statement and Research Objectives

The unique properties of nanocrystalline metals make them suitable for use in a variety of potential applications, however their lack of thermal stability and brittle failure severely limit the feasibility of their use. Tuning the grain boundary chemistry and structure in order to create materials with very thick amorphous complexions enables the formation of nanocrystalline metals with high strength, ductility, and thermal stability. While the formation of amorphous complexions in binary alloys has been widely studied, the study of their formation in multicomponent alloys has been limited and limits the practicality of use of these materials, considering the majority of alloys used in engineering applications are composed of more than two elements. Further complicating the grain boundary chemistry may enable the formation of thicker and more stable amorphous complexions, allowing for the formation of these grain boundary phases in multicomponent alloys. Therefore, it is the goal of this thesis to investigate the effects of complicating the grain boundary chemistry on the thickness and stability of amorphous complexions. The thesis is organized as follows:

Chapter 2: First, we explore the effect of adding a second dopant element to the thickness of complexions which form in a Cu-Zr alloy. Amorphous complexions in a ternary Cu-Zr-Hf alloy were found to be roughly 9% thicker on average than those in the binary Cu-Zr alloy, due to the co-segregation of Zr and Hf atoms to grain boundaries in the ternary alloy. The significant improvement to complexion thickness can also be described by the shift in thickness distribution, where complexions with thicknesses greater than 4 nm comprised of only 3.9% of the population observed in the Cu-Zr alloy, as opposed to 10% of the complexions observed in Cu-Zr-Hf.

Chapter 3: Building on the results of the previous chapter demonstrating that more complex grain boundary chemistries can lead to the formation of thicker amorphous complexions, three quinary alloys are formed and characterized to determine whether we can maximize this effect. We find that amorphous complexions with high-entropy grain boundary compositions are able to form in a Cu-Zr-Hf-Nb-Ti alloy which are 32% thicker than those formed in the Cu-Zr-Hf alloy and 41% thicker than those formed in the Cu-Zr alloy reported on in Chapter 2. 17% of amorphous complexions observed in the quinary alloy had thicknesses greater than 4 nm, showing a significant increase in the number of thick amorphous complexions which form associated with greater chemical complexity at the grain boundary.

Chapter 4: Now that the correlation between chemical complexity at grain boundaries and amorphous complexion thickness has been well established, the stability of these grain boundary phases against transformation upon cooling is explored. The thicknesses of amorphous complexions in binary Cu-Zr and ternary Cu-Zr-Hf alloys when exposed to a variety of cooling rates. The relation between amorphous complexion thickness and cooling rate provides insight as to whether the complication of grain boundary chemistry makes these amorphous complexions more resistant to transformation to thinner or ordered grain boundaries upon cooling. Estimates for critical cooling rates necessary to avoid complexion transitions upon cooling are also presented.

2 Thick amorphous complexion formation and extreme thermal stability in ternary nanocrystalline Cu-Zr-Hf alloys

2.1 Introduction

In this chapter, we investigate the effects of the manipulation of grain boundary chemistry by studying the difference in complexion formation behavior between binary and ternary alloys. Building on the discovery of tough nanocrystalline Cu-Zr alloys with amorphous intergranular films, this chapter investigates ternary nanocrystalline Cu-Zr-Hf alloys with a focus on understanding how alloy composition affects the formation of disordered complexions. Hf has a positive enthalpy of segregation and negative enthalpy of mixing in Cu, and the Cu-Hf alloy has been previously proven to form amorphous complexions [67]. Additionally, the chemical similarity between Hf and Zr, in addition to their similarity in atomic size, makes Hf an attractive dopant choice. This allows for the most direct observation of the effects of grain boundary chemistry on amorphous complexion formation. Binary Cu-Zr and Cu-Hf alloys with similar initial grain sizes were also fabricated, to gain an understanding of the distribution of dopants throughout each sample and their contributions to thermal stability. The thermal stability of the nanocrystalline alloys was evaluated by annealing at 950 °C (>95% of the solidus temperatures), followed by detailed characterization of the grain boundary structure. All of the ternary alloys exhibited exceptional thermal stability comparable to that of the binary Cu-Zr alloy, and remained nanocrystalline even after two weeks of annealing at this extremely high temperature. Despite carbide formation and growth in these alloys during milling and annealing, the thermal stability of the ternary alloys is mainly attributed to the formation of thick amorphous intergranular films at high temperatures. Our results show that ternary alloy compositions have thicker boundary films compared to the binary alloys with similar global dopant concentrations. While it is not required for amorphous complexion formation, this work shows that having at least three elements present at the interface can lead to thicker grain boundary films, which is expected to maximize the previously reported toughening effect.

2.2 Materials and Methods

To begin, we must select alloying elements and compositions which will allow for dopant segregation to the grain boundaries and possibly transformation into amorphous complexions. As mentioned previously, Schuler and Rupert developed materials selection guidelines for AIF formation which emphasized a positive enthalpy of segregation and a negative enthalpy of mixing [67]. Bulk metallic glass formation guidelines suggest that multicomponent systems with three or more elements, a negative heat of mixing, and an atomic size mismatch greater than 12% encourage the formation of amorphous phases [68]. The thermal stability and mechanical behavior of nanocrystalline Cu has been widely studied [15, 92, 93], and both Zr and Hf dopants have already been shown experimentally to exhibit strong tendencies to segregate to grain boundaries in Cu [67, 71]. Zr and Hf both possess positive enthalpies of segregation and negative enthalpies of mixing with respect to Cu [23, 94] and have atomic radii that are 25% and 24% larger than Cu, respectively. Although Zr and Hf have nearly identical atomic radii, it has been shown in prior studies that the addition of small amounts of Hf in Zr-based bulk metallic glasses enhances the glass forming ability [95, 96]. In addition, binary phase diagrams for Cu-Zr and Cu-Hf both show deep eutectic points at nearly identical temperatures and concentrations [97, 98]. The similarity of the binary phase diagrams allows for a relatively clear comparison of the ternary mixtures with the two binary baseline systems. Although the ternary phase diagram would be helpful for choosing temperatures and compositions, we could not find a reliable source in the literature.

Binary Cu-Zr, binary Cu-Hf, and ternary Cu-Zr-Hf alloys were produced using elemental Cu (Alfa Aesar, 99.99%, -170 + 400 mesh), Zr (Micron Metals, 99.7%, -50 mesh), and Hf (Alfa Aesar, 99.8%, -100 mesh) powders as starting materials. The powders were ball milled in a SPEX SamplePrep 8000M high-energy ball mill using hardened steel milling media for 10 h under inert atmosphere (99.99% pure Ar) in order to force dopant atoms into solid solution with the Cu matrix, and to ensure grain size refinement. A ball-to-powder weight ratio of 10:1 was employed and 1 wt.% stearic acid was added to the powder mixture prior to milling as a process control agent in order to prevent excessive cold welding. While stearic acid was used for all of the samples discussed in detail here, limited additional powders were processed using hexane, methanol, and toluene as alternative process control agents to observe the effect on contamination during milling. Before milling the targeted alloys, Cu powder and 1 wt.% stearic acid was ball milled for 2 hours and then disposed of in order to coat the vial and milling media with a thin layer of Cu, which helps to minimize Fe contamination from the collisions with the vial walls and media. For the binary alloys, we created samples with low (4-5 at.%) and high (10-11 at.%) dopant concentrations. The Zr concentration in the ternary alloys was kept relatively constant at 4-5 at.% in order to make a direct comparison of their thermal stability and complexion formation behavior to binary alloys. The Hf concentration of the ternary alloys was then varied from 1 to 5 at.%. Sample compositions were determined using energy dispersive X-ray spectroscopy (EDS) in a Tescan GAIA3 scanning electron microscope (SEM) and are displayed in Table 2-1.

Table 2-1: Chemical compositions, XRD grain sizes, and TEM grain sizes of each alloy investigated in this study. All samples were annealed for 1 h, 24 h (1 day), 168 h (1 week), and 336 h (2 weeks) at 950 ℃. The average TEM grain sizes of samples annealed for 168 h (1 week) agree with the XRD grain sizes for the same samples. Dopant concentrations obtained with EDS are typically subject to measurement error of ~1 at.%.

Specimen Nominal Composition (at. %)	EDS dopant concentration (at. %)		XRD grain size (nm)					TEM grain size (nm)
			Annealing Time					
	Zr	Hf	0 h	1 h	24 h	168 h	336 h	168 h
Cu	0	0	25	108	109	-	132	-
Cu-5Zr	4.7	0	20	34	44	51	66	50
Cu-4Hf	0	3.9	19	50	59	68	113	63
Cu-10Zr	9.8	0	12	23	24	49	47	39
Cu-11Hf	0	11.3	25	80	90	117	134	103
Cu-4Zr-1Hf	4.2	0.9	24	44	44	52	62	48
Cu-5Zr-3Hf	4.9	2.7	21	41	45	45	67	52
Cu-5Zr-5Hf	4.8	4.7	22	39	54	47	60	50

The milled powders were then encapsulated under vacuum in SiO_2 tubes, annealed at 950 °C, and then rapidly quenched by immediately dropping into water to freeze in the microstructure which is stable at high temperature. Annealing of the samples encourages the diffusion of Zr and Hf atoms from the Cu matrix to Cu grain boundaries, allowing for the formation of the amorphous phase at the grain boundary through a premelting transition. Such an extreme annealing temperature, greater than 95% of solidus temperature for both binary alloys, was chosen in order to investigate the thermal stability of all samples at temperatures where AIFs are able to form. Annealing times of up to two weeks or 168 h were employed in order to probe the long-term stability of the nanocrystalline alloys. The various dopant concentrations in each sample and anneal times are tabulated in Table 2-1. All samples were analyzed using X-ray diffraction (XRD), with phase identification, volume fraction, and grain size measurements for both Cu and any second phases made via Rietveld analysis [99]. XRD patterns were collected with a Rigaku SmartLab X-ray diffractometer equipped with Cu Kα radiation and a 1D D/teX Ultra 250 detector. A LaB_6 standard sample was used to calibrate instrumental parameters, including contributions to peak profile (axial divergence, instrumental broadening) and position (goniometer alignments).

Specimens for investigation with the transmission electron microscope (TEM) were prepared by the lift-out method using a Tescan GAIA3 SEM that is also equipped with a focused ion beam (FIB). A final 2 kV polish of all specimens was performed using a Fischione Model 1040 NanoMill in order to remove excess Ga^+ ion beam damage or amorphization of the surface that may have been caused by earlier preparation steps. A JEOL JEM-2800 TEM equipped with dual EDS detectors was used to perform detailed microstructural characterization and chemical analysis. Selected area electron diffraction (SAED) patterns, high resolution imaging, and high-angle annular dark field scanning TEM mode were also employed for further phase identification and microstructural characterization. To confirm the validity of grain sizes obtained via Rietveld refinement of XRD scans, the average grain sizes from at least 100 grains were measured from TEM micrographs for each sample that had been annealed for one week (Table 2-1). In order to observe solute and second phase distribution throughout the sample, chemical analysis was performed with EDS in order to observe dopant and second phase distribution throughout the microstructure. EDS line scans across grain boundaries were performed in order to confirm segregation of both dopant elements to the grain boundaries in each sample. It is important to note that overlapping grains and slight misalignments from a perfect edge-on condition could not be completely ruled out for these EDS measurements, so the data should be interpreted as a qualitative measurement of boundary chemistry. In order to investigate the effects of the addition of a ternary alloy composition on AIF thickness, at least 50 AIFs were imaged from each the Cu-5Zr, Cu-4Hf, and Cu-4Zr-1Hf samples after annealing for one week. Care was taken to ensure that the grain boundaries investigated were in an edge-on condition by using stage tilting and Fresnel fringe imaging.

2.3 Results and Discussion

2.3.1 Microstructural Evolution during Annealing

XRD patterns and the associated phase identification of all as-milled powders are shown in Figure 2-1.

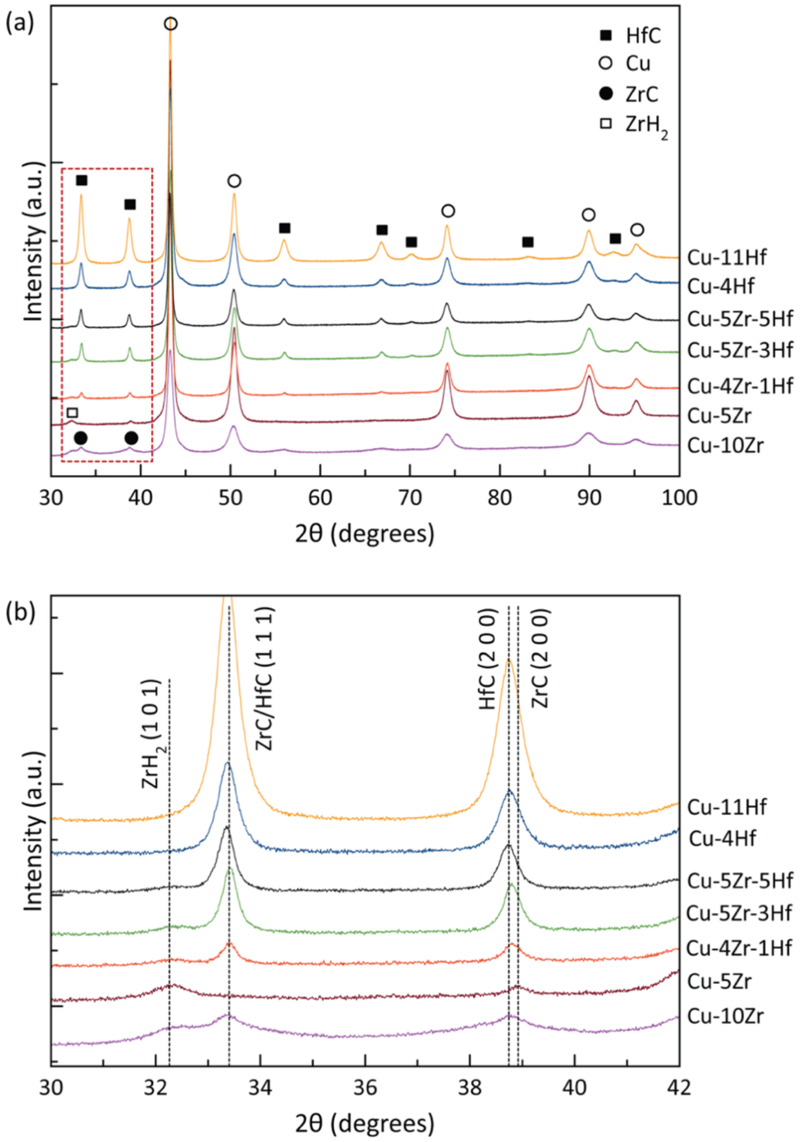

Figure 2-1: (a) X-ray diffraction patterns of the as-milled samples. Phase identification shows the presence of HfC phases for all samples containing Hf, as well as ZrC and ZrH_2 phases in Zr-containing samples. (b) Zoomed view of the low angle region where carbide and hydride phases can be seen.

The nanocrystalline metallic phase is face centered cubic (fcc) in all cases. ZrC and HfC phases have also formed during ball milling and are present in the microstructure for all alloys (Figure 2-(b)), even before heat treatment. The formation of carbide phases is likely due to the C-containing process control agent used during mechanical alloying. Possible alternative process control agents were explored (methanol, hexane, and toluene), but these all contain C and lead to similar amounts of carbide formation. Small peaks corresponding to the ZrC phase are evident in the diffraction pattern for the Cu-5Zr but are wider and more prominent in Cu-10Zr. Pronounced HfC peaks are present in all Hf-doped samples, with the intensities of the HfC peaks increasing with increasing Hf concentration. The volume fraction and evolution of the carbide precipitates in each sample will be described in more detail later in the paper. A very small amount of ZrH_2 phase is present in all of the as-milled specimens containing Zr, although this phase disappears after annealing.

The average grain size of the fcc phase was calculated from XRD and is displayed in Figure 2-2 as a function of annealing time.

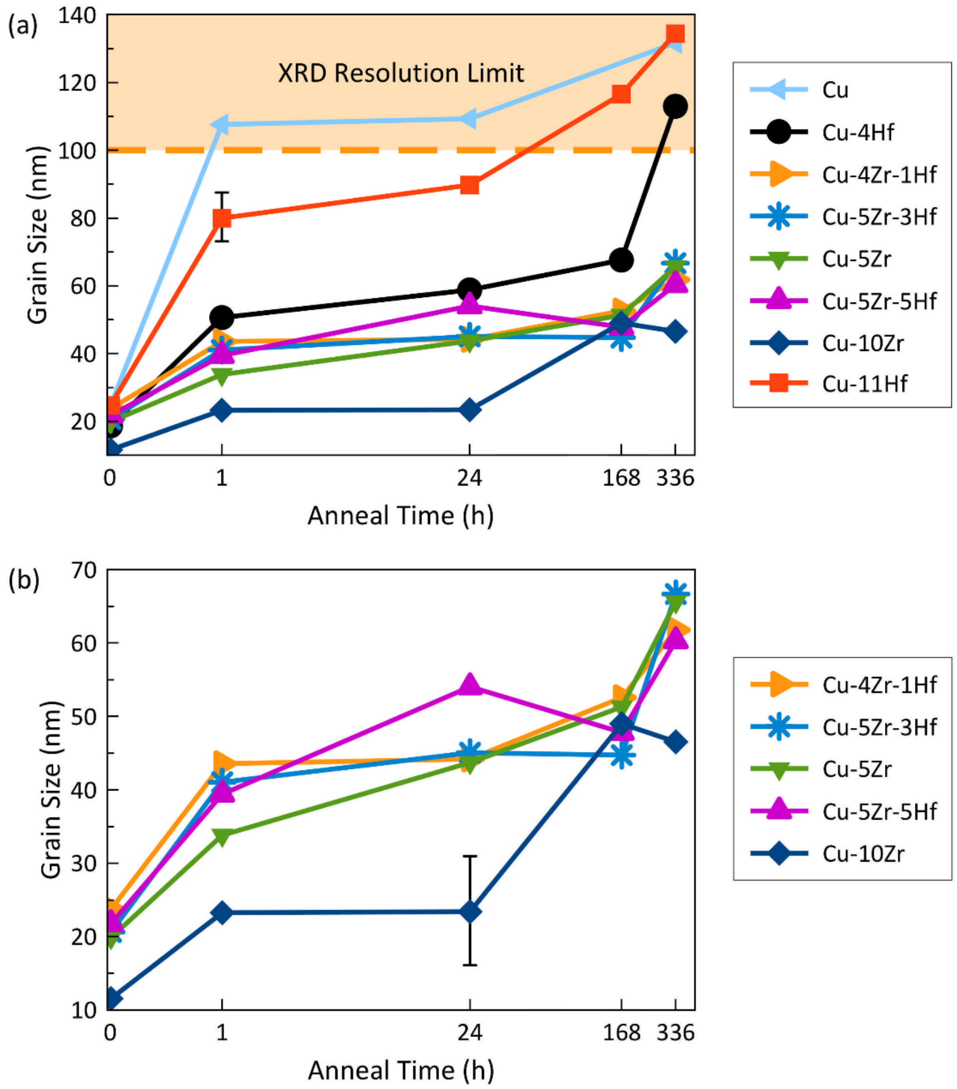

Figure 2-2: (a) Grain sizes for all alloys calculated from XRD patterns as a function of anneal time. Binary Cu-Zr and ternary Cu-Zr-Hf alloys display greater thermal stability than the Cu-Hf alloys. (b) Zoomed view of the grain size data for the Cu-Zr and Cu-Zr-Hf alloys. The 15 nm error bar shown in (a) represents the error in XRD grain size from the results of Rietveld refinement.

Figure 2-2(a) presents all data, while Figure 2-2(b) presents a zoomed view of the Cu-Zr and Cu-Zr-Hf alloys. Grain sizes of ball-milled, pure Cu are also included for comparison. For all annealing times, the vast majority of the alloyed samples exhibit superior thermal stability as compared to the pure Cu sample, with the exception of Cu-11Hf after 336 h (i.e., 2 weeks). Grain sizes calculated via XRD pattern refinement are reliable up to roughly 100 nm [100], which is marked by the orange dashed line in Figure 2-2. The pure Cu sample grows beyond the XRD resolution by the first measurement (1 h), while the binary Cu-Hf alloys all exceed the XRD resolution by the end of the tests. In contrast, both the Cu-Zr and Cu-Zr-Hf alloys remain nanocrystalline with grain sizes in the range of ~50-65 nm after annealing for 2 weeks at 950 °C. The ternary alloys exhibit grain growth trends that closely track the behavior of the Cu-5Zr alloy (their binary analog, since it has a similar amount of Zr). These results represent a significant increase in thermal stability for nanocrystalline alloys as compared to prior studies. For example, Darling et al. investigated the thermal stability of ball-milled Cu-Ta alloys, reporting an average grain size of 167 nm after annealing for 4 h at 97% of the melting temperature for Cu [101]. In addition, a thermal stability study of a ball-milled W-20 at.% Ti alloy reported an average grain size of 24 nm after annealing at 1100 °C for one week [102]. It is important to note, W is an extremely refractory metal and 1100 °C is only ~32% of the melting temperature of pure W. In comparison, all ternary alloys investigated in this study remain well within the nanocrystalline regime even after 2 weeks of annealing at 96-98% of solidus temperature of the binary alloys.

Figures 3(a-d) present bright field TEM micrographs of the Cu-4Hf and Cu-Zr-Hf alloys that were annealed for 1 week, as well as SAED patterns for phase identification. The SAED patterns confirm the presence of HfC phase dispersed throughout the microstructure in all Hf-doped samples, which can be visually observed in the micrographs at the grain boundaries of the larger Cu grains. No intermetallic phases were found in any of the samples in this study. Grain size distributions measured by TEM for each sample annealed for 1 week are shown in Figure 2-3(e), and the average values are listed in Table 2-1.

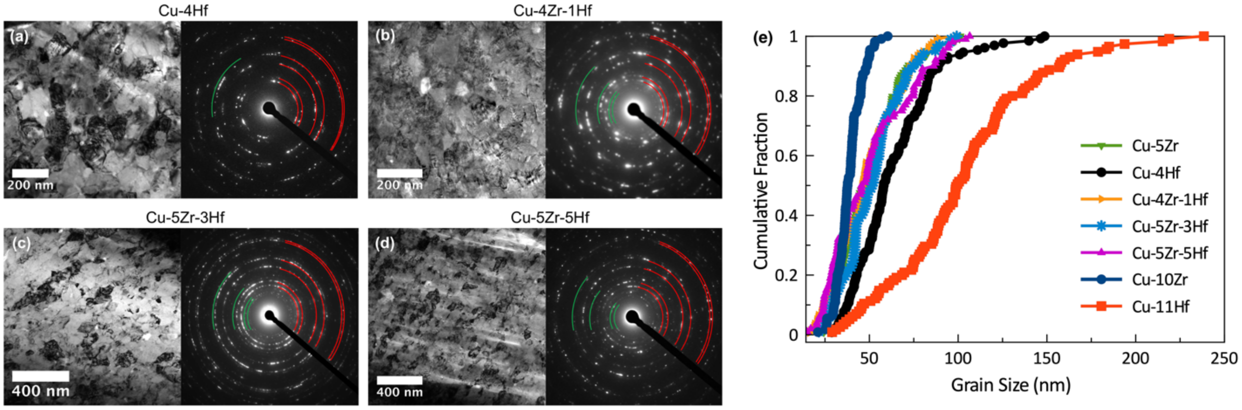

Figure 2-3: Bright field TEM images and SAED patterns for (a) Cu-4Hf, (b) Cu-4Zr-1Hf, (c) Cu-5Zr-3Hf, and (d) Cu-5Zr-5Hf samples that have been annealed for 1 week at 950 ℃. SAED patterns confirm the XRD phase identification results, showing the presence of HfC particles. Cu and HfC phases in the SAED patterns are represented by red and green lines, respectively. Grain size distributions after 1 week of annealing at 950 ℃ are shown in (e). At least 100 grains were measured from TEM micrographs of each sample. A narrow grain size distribution and an average grain size in the nanocrystalline range (<100 nm) is observed for the majority of the samples, with the Cu-11Hf sample being the exceptio

The grain size measurements and phase identification from XRD agree with TEM analysis. Abnormal grain growth, which presents as a bimodal distribution of grain size [36, 46, 103], was not observed. The inhibition of abnormal grain growth in these alloys is in stark contrast to many other materials possessing AIFs, particularly in several ceramic systems [103-105] where the presence of AIFs is associated with rampant abnormal grain growth. Dillon, Harmer, and coworkers reported abnormal grain growth associated with AIF formation in calcia and silica-doped alumina [36, 106]. Abnormal grain growth in alumina without planned dopants due to AIF formation has also been reported to occur, due to exposure to very small amounts of impurities during the sintering process [17]. However, for the alloys in this present study, the presence of AIFs actually serves to stabilize the microstructure. With the exception of Cu-11Hf, which has a very broad distribution of grain sizes from 30 nm up to 250 nm, all alloys have narrow grain size distributions and retain nanocrystalline grain sizes after 1 week of annealing (Figure 2-3(e)). This finding is in agreement with previously reported results from a study of a binary Cu-Zr alloy [70, 71]. The formation of AIFs has also been achieved in a variety of other metallic alloy systems, such as Mo-Ni [63], Ni-W [65], and Cu-Hf [67], with no abnormal grain growth reported.

Average carbide particle sizes and volume fractions measured from XRD patterns, are shown in Figure 2-4(a) and 4(b) respectively.

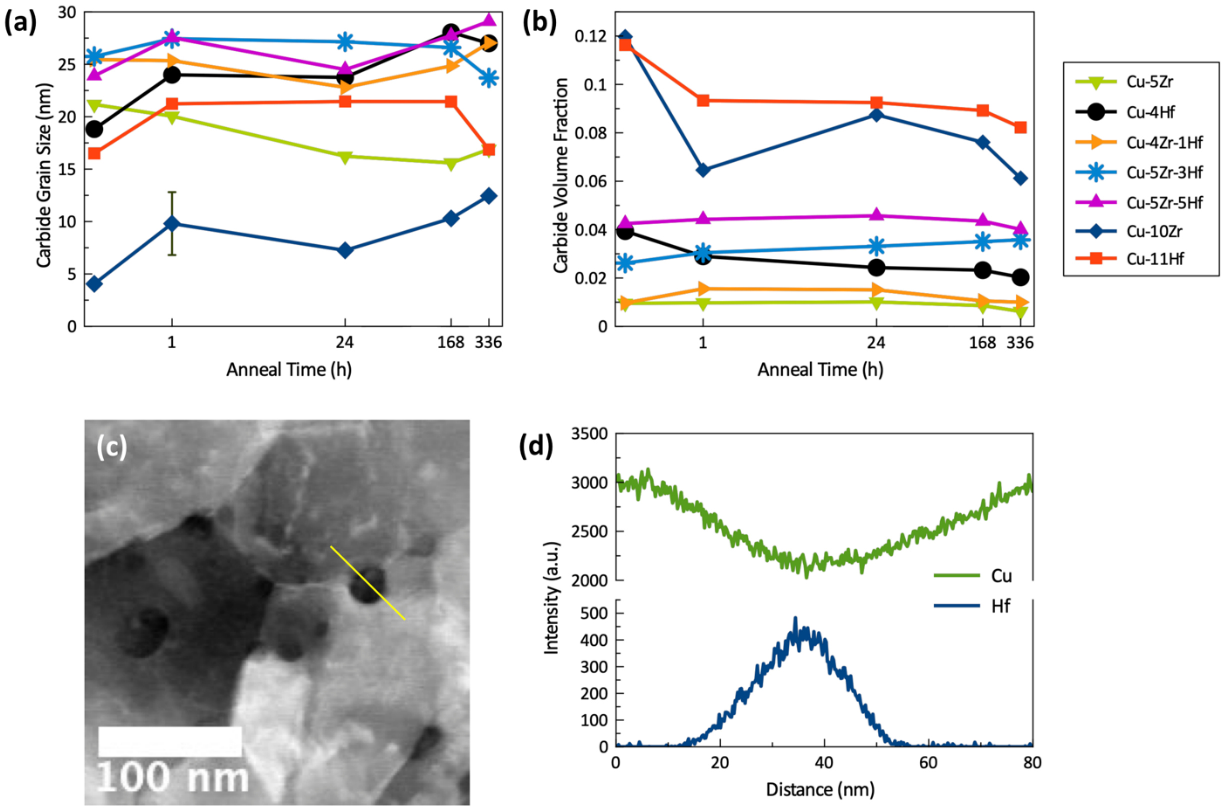

Figure 2-4: (a) Carbide grain size and (b) volume fraction from XRD as a function of anneal time. The carbide grain sizes in (a) stay relatively constant during annealing, with any fluctuations being within the expected error (shown as a black error bar) of the XRD measurements. The carbide volume fractions in (b) also stay constant during annealing, with the exception of Cu-10Zr and Cu-11Hf which experience a slight decrease in carbide volume fraction during the early stages of annealing. (c) HAADF STEM micrograph and (d) EDS line scan from a Cu-4Hf sample annealed for one week, showing the presence of carbides with various sizes.

It is evident that the grain size of the carbide precipitates stays relatively constant in each sample during annealing, with any fluctuations being within the measurement error of XRD grain size measurements. The carbide volume fractions shown in Figure 2-4 (b) also stay constant for most samples, except for the Cu-10Zr and Cu-11Hf samples, where a decrease in carbide phase fraction is found after annealing for 1 h. Despite having 1 at. % less dopant, the Cu-4Hf sample has a significantly higher volume fraction of carbides than the Cu-5Zr sample; after one week of annealing, the Cu-4Hf sample had a carbide volume fraction of 0.023, which is more than double the carbide volume fraction of 0.009 found in Cu-5Zr. This provides an explanation for the difference in thermal stability behavior between these two samples, as there are fewer Hf atoms available to segregate to grain boundaries and thermodynamically stabilize the microstructure. In general, the Cu-Hf alloys have higher volume fractions of the carbide phase than the Cu-Zr alloys with similar overall dopant concentration, suggesting that HfC is easier to form than ZrC under similar processing conditions. This observation is supported by the calculated formation enthalpies of ZrC (-207 kJ/mol) and HfC (-226 kJ/mol) [107]. In contrast, the Cu-5Zr and Cu-4Zr-1Hf alloys have nearly identical carbide phase volumes and also the lowest amounts of all samples investigated in this study, meaning that they should have the same number of dopant atoms free to segregate to grain boundaries to stabilize the microstructure. This is highlighted by the nearly identical thermal stability behavior exhibited by these two samples in Figure 2-2.

HfC phase distribution throughout the microstructure was further investigated using STEM imaging and EDS. Figure 2-4(c) shows a high angle annular dark field STEM micrograph of a carbide precipitate at a grain boundary in the Cu-4Hf alloy, which are observed throughout the sample microstructure. An EDS line scan across one of these precipitates in Figure 2-4(d) demonstrates a high Hf concentration, suggesting that these are HfC particles. While smaller precipitates are indeed scattered throughout the microstructure along the grain boundaries of the Cu-rich, fcc phase, we also occasionally find much larger HfC particles that are ~100-200 nm in diameter. These large precipitates are more common in the samples with larger dopant concentrations.

The microstructures of the Cu-5Zr and Cu-4Zr-1Hf samples annealed for one week were subjected to a more rigorous analysis of the carbide phase distribution throughout the samples. These two specimens were chosen due to their very low, and nearly identical, phase volume fractions, as well as their similar thermal stability behavior. A representative micrograph of the carbide phase distribution in Cu-5Zr annealed for one week is shown in Figure 2-5(a), showing the presence of slightly larger precipitates at the grain boundaries, but also particles scattered in the grain interiors.

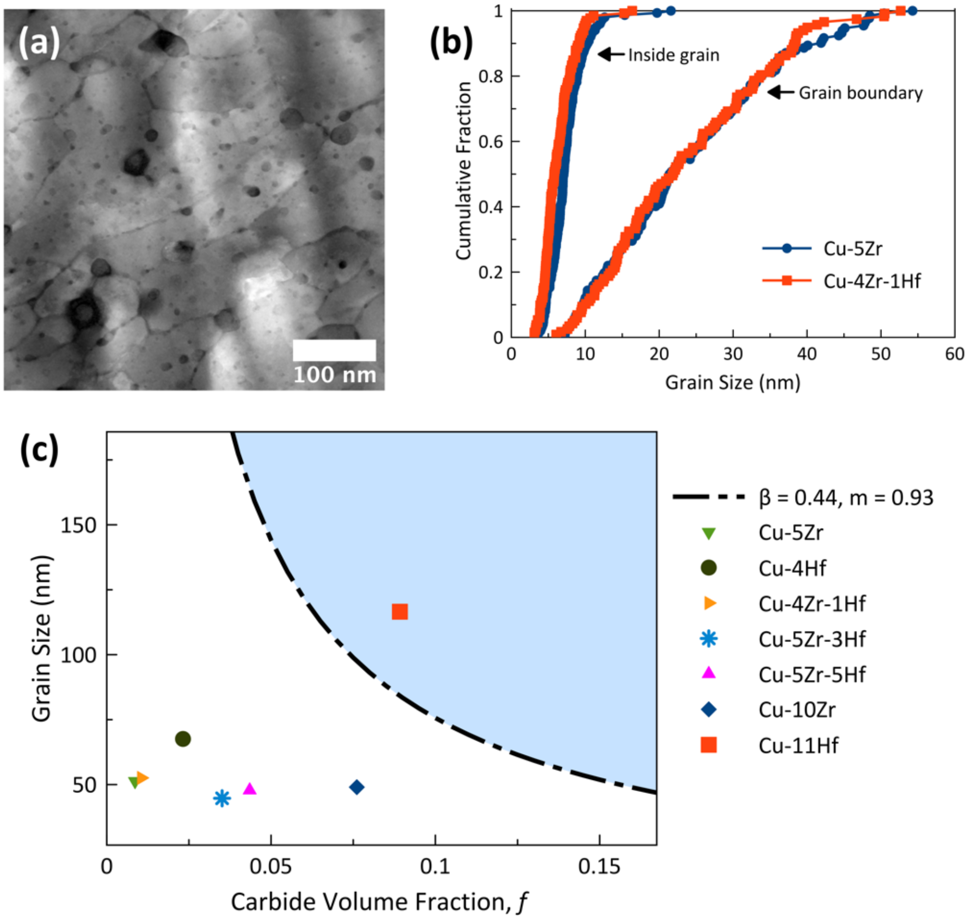

Figure 2-5: (a) HAADF STEM micrograph showing the distribution of carbides within grain interiors and at grain boundaries in the Cu-5Zr alloy annealed for 1 week at 950 °C. (b) Cumulative distribution functions demonstrating the similarity in carbide size distribution at both the grain boundaries and grain interiors for the Cu-5Zr and Cu-4Zr-1Hf alloys. (c) Grain size estimated by the Zener equation for an average second phase (carbide in this case) particle size of 20 nm, versus second phase volume fraction, f. *The black dashed line represents the predicted grain size for Zener-pinned grains from Equation 2. TEM grain sizes for samples annealed for 1 week as a function of* f *are plotted on this figure. With the exception of Cu-11Hf, all alloys have grain sizes much smaller than that predicted by the Zener equation, indicating that microstructural stabilization by boundary doping and AIF formation plays a significant role in their thermal stability.*

Figure 2-5(b) shows that the size distribution of the carbide particles in the Cu-5Zr and Cu-4Zr-1Hf samples, both at the grain boundaries and within the grain interior, are identical between the two samples. The average size of these particles measured from STEM images agrees well with that measured using XRD. The following discussion will focus primarily on the Cu-5Zr and Cu-4Zr-1Hf samples due to their similarity in microstructure and thermal stability, allowing for the clearest possible investigation of the effects of the addition of a second dopant element on the grain boundary structure.

Since all of the alloys studied here do contain second phase carbide precipitates, it is reasonable to ask whether the thermal stability we observe can be attributed to these particles. Grain size stabilization by Zener pinning can be modeled by [25]:

$$d_Z = \beta \frac{D}{f^m}$$

where d_Z is the estimated grain size of Zener-pinned grains, D is the second phase particle size, f is the volume fraction of second phase particles, and both β and m are constants. Hillert [108] suggested that the constants $\beta = 0.44$ and $m = 0.93$ be used. The grain sizes of Zener-pinned grains for all alloys annealed for one week are shown in Figure 2-5(c). Grain sizes that are at or above the predictions of Equation 2, in the region that is shaded blue, can possibly be explained as a purely kinetic stabilization caused by second phase particles. On the other hand, grain sizes below these values must be either stabilized by predominantly thermodynamic effects (reduction in grain boundary energy) or, most likely, a combination of kinetic and thermodynamic effects. Of the alloys studied here, only the Cu-11Hf sample falls in the blue region. All of the other samples have grain sizes that are much too small for only kinetic stabilization alone. As such, we next move to confirm dopant segregation to grain boundaries in the different alloys, and investigate the effects of a second segregating dopant element on grain boundary structure; specifically, the formation of thicker amorphous intergranular films which can account for the extreme thermal stability demonstrated by these alloys.

2.3.2 Dopant Segregation and Amorphous Complexion Formation

Previous studies by Khalajhedayati and coworkers [70, 71] reported the formation of amorphous intergranular films in nanocrystalline Cu-Zr alloys processed under conditions similar to those used to create the alloys studied here. To study this behavior, grain boundary segregation of the dopants was observed via STEM and EDS, confirming the conditions necessary for AIF formation. Figure 2-6(a) shows a HAADF STEM micrograph of the microstructure of Cu-4Zr-1Hf, annealed for 1 week.

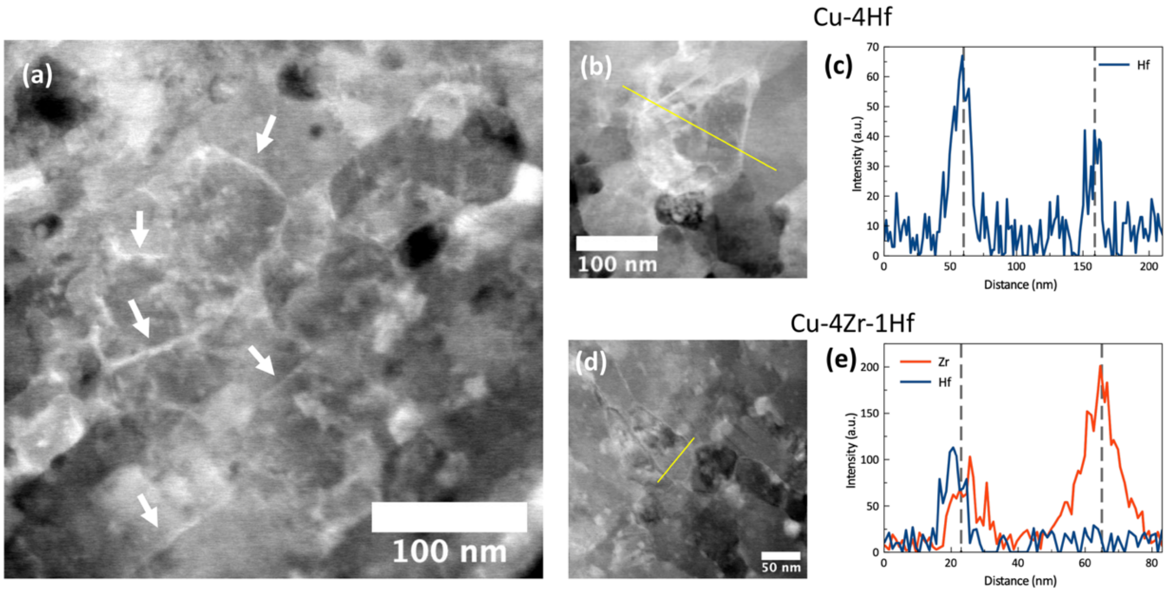

Figure 2-6: (a) HAADF STEM micrograph showing heavily doped boundaries in a Cu-4Zr-1Hf alloy annealed for 1 week. Arrows point to regions of brighter contrast associated with Zr and Hf segregation to these grain boundaries. (b) HAADF STEM micrograph and (c) corresponding EDS line scan showing Hf segregation to grain boundaries in a Cu-4Hf sample annealed for 1 week. (d) HAADF STEM micrograph and (e) corresponding EDS line scan showing segregation of both Zr and Hf to grain boundaries in a Cu-4Zr-1Hf sample annealed for 1 week. In both cases, the grain boundaries are heavily decorated with the dopants. The location of the grain boundaries in parts (c) and (e) are indicated with grey dotted lines.

Regions of bright contrast are seen along several grain boundaries, suggesting segregation of higher Z atoms (Zr and/or Hf) to those boundaries. To confirm dopant segregation, EDS line scans were performed across grain boundaries in Cu-4Zr and Cu-4Zr-1Hf samples annealed for one week, shown in Figures 6(b-e). It is apparent that there are significant spikes in dopant concentration above the noise level inside of the crystals at the grain boundaries, supporting the hypothesis that thermodynamic effects from dopant segregation are also working to stabilize the microstructure. Special care was taken to avoid precipitated secondary phases and ensure that all line scans were taken across grain boundaries only. Even though carbides have formed in the samples doped with Hf, as shown in Figure 2-4, there remains sufficient unreacted Hf in the alloy to segregate to the grain boundaries. Figure 2-6(e) also demonstrates the variability of dopant segregation behavior that can occur within a given microstructure, where one boundary is co-doped with both Zr and Hf, while another boundary is doped only by Zr. The occurrence of co-doping of grain boundaries is promising for the hypothesis that thicker, more stable AIFs will form in ternary alloys as compared to binary alloys, since it demonstrates that the multiple added elements have a synergistic effect where the segregating dopants attract each other to the interface rather than compete for segregation sites [109]. This behavior is not surprising, as Zr and Hf have very similar chemical properties with nearly identical atomic and ionic radii [110], and exhibit attractive interactions as evidenced by the fact that they are commonly found together in nature in the same ores [94, 110-112].

Following the confirmation of grain boundary segregation in binary and ternary alloys doped with Hf, high resolution TEM was used to investigate the details of grain boundary structure in each alloy. Figure 2-7 presents representative examples of complexions found in various alloys annealed for 1 week at 950 °C.

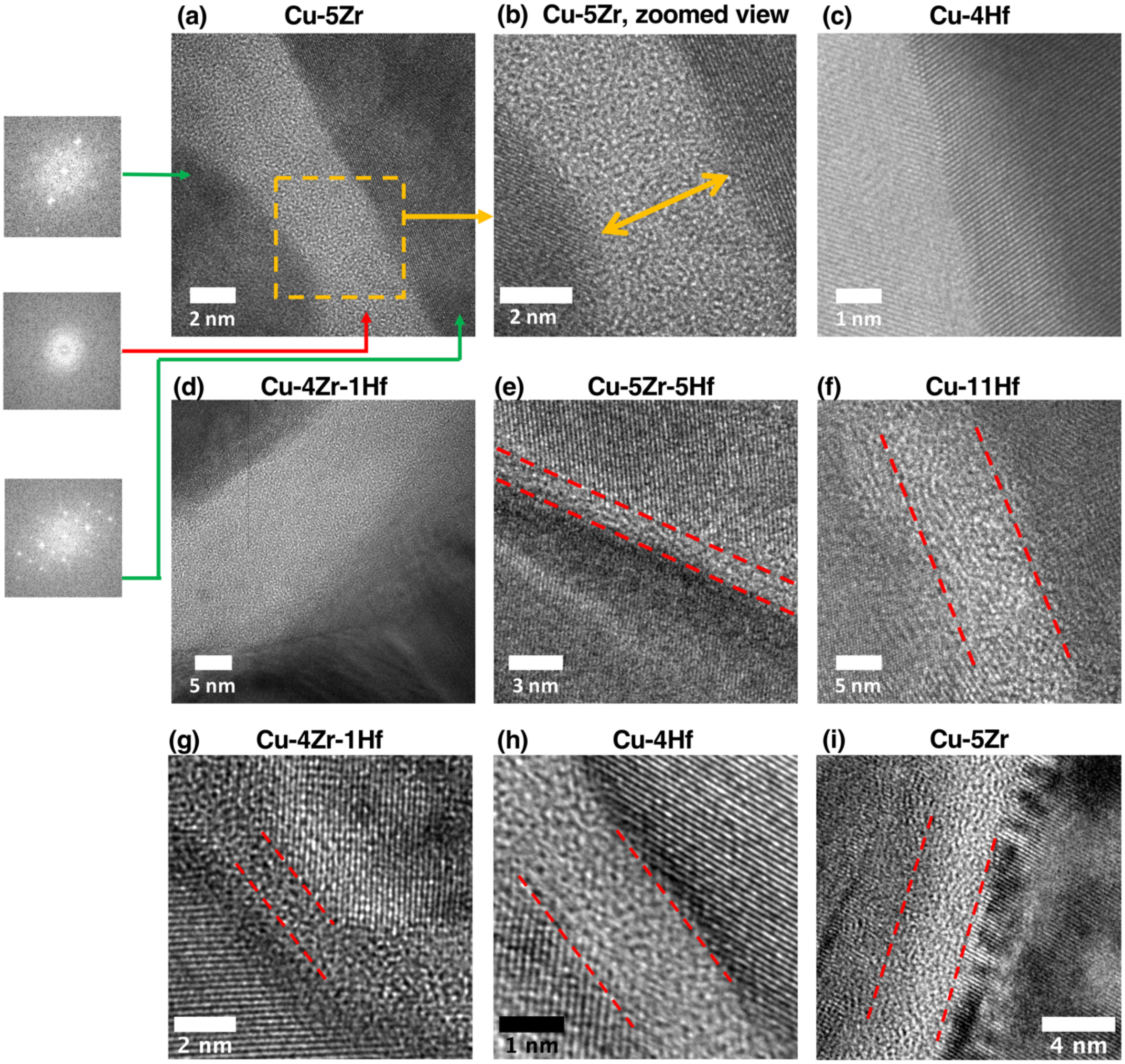

Figure 2-7: HRTEM micrographs of various complexions found in binary and ternary alloys annealed for 1 week. Dotted red lines denote AIFs between two crystalline regions. In (a), fast Fourier transforms of the crystalline and amorphous regions are shown on the left and the region that is edge-on is highlighted by a dashed yellow box. In (b), a zoomed view of the complexion in (a) to display the region of the grain boundary complexion where thickness measurements are made. The thickness of the complexion shown in (a) and (b) is 4.1 nm. A clean boundary in Cu-3Hf is shown in (c).

Figure 2-7(a) shows an example of a thick AIF in the binary Cu-5Zr sample, where fast Fourier transforms confirm the amorphous structure of the grain boundary region and the crystallinity of the abutting grains. Obvious AIFs were found in all of the samples presented in this work. However, Figure 2-7 also makes it clear that these AIFs had a variety of thicknesses. Figure 2-7(d) shows the thickest AIF found in this study, having a thickness of ~9 nm. On the other hand, the boundary from the Cu-5Zr-5Hf sample that is shown in Figure 2-7(e) is amorphous but relatively thin in comparison. An important consideration to note is that the grain boundary should be edge-on when measuring the thickness of an AIF in order to ensure accuracy of the measurement. Figure 2-8(a) shows an example of an AIF found in the Cu-5Zr sample annealed for 1 week, with a thickness of 3.4 nm. Images of the complexion at defocus values of -6, -3, 0, 3, and 6 nm are also shown in order to demonstrate an edge-on imaging condition where the thickness of the AIF does not vary, and guarantees integrity of the measurement. Figure 2-8(b) shows a similar image series for an AIF in the Cu-4Zr-1Hf sample.

To allow for a meaningful discussion of AIF thickness for different samples, the thicknesses of at least 50 grain boundary complexions from each of the Cu-5Zr, Cu-4Hf, and Cu-4Zr-1Hf alloys annealed for one week from HRTEM micrographs of grain boundaries in an edge-on condition were measured, and are plotted in Figure 2-9. These three samples were selected for detailed inspection because this allows for the direct observation of the effect of global dopant concentration on AIF thickness, as well as a comparison between binary and ternary alloy compositions with the same global dopant concentration. Additionally, these samples have relatively low carbide volume fractions (all are < 3 vol.%). Since the specimens with a great deal of carbides may have less dopant available for possible segregation, this allows us to make the cleanest possible comparison of grain boundary structure between the samples. It is important to note that the thicknesses of all AIFs from all samples were measured from the thinnest observable region in the edge-on portion of each grain boundary, in order to make conservative measurements and reliable comparisons across all three samples. Taking thickness measurements from the edge-on region of the grain boundary helps to ensure that we do not report artificially high thickness values that come from a boundary being inclined with respect to the viewing direction. An instructive example of the potential error that could be introduced by taking measurements from an improperly aligned region is found in Figure 2-7(a). Although it may look as though there is a significant variation in thickness across the length of this AIF, only the region of the AIF denoted in the dashed box is in an edge-on condition. In fact, if the region near the top of this figure is inspected at greater magnification, we find evidence of small regions where lattice fringes are visible, suggesting that this is a projection of both a crystal and an amorphous region (i.e., an AIF that is inclined with respect to the viewing direction). Therefore, thicknesses taken from such a region would not be reliable measurements. Figure 2-8 shows the process by which thickness measurements are reported for each AIF investigated in this study.

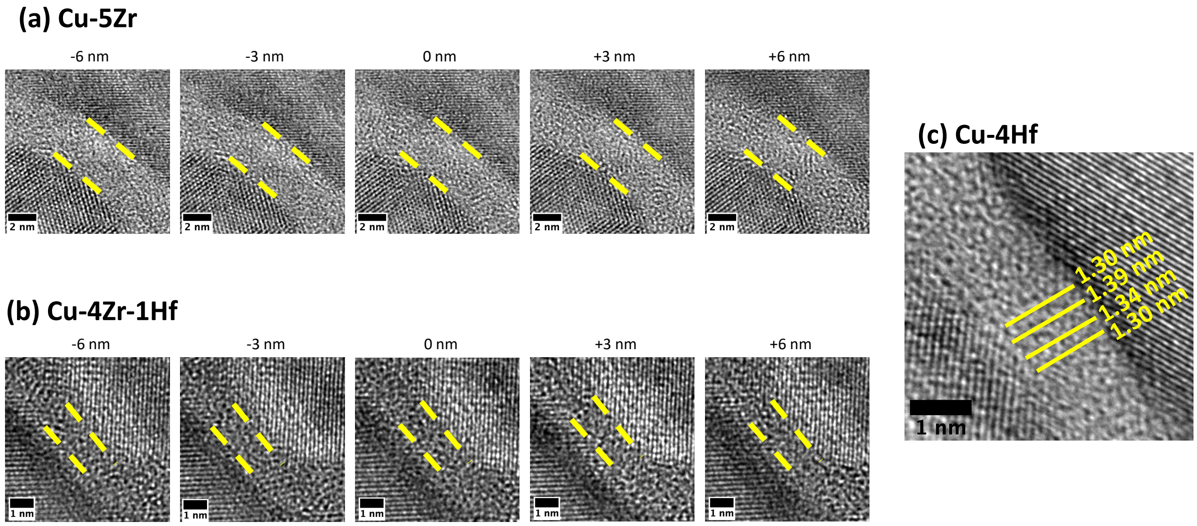

Figure 2-8: HRTEM micrograph of complexions in (a) a Cu-5Zr sample (scale bar 5 nm), (b) a Cu-4Zr-1Hf sample (scale bar 2 nm), and (c) a Cu-4Hf sample annealed for one week at 950 °C. The AIF thicknesses of 3.4 nm in the (a) Cu-5Zr sample and 1.2 nm in the (b) Cu-4Zr-1Hf sample remains unchanged in under-focused, focused, and over-focused imaging conditions, demonstrating that the grain boundary complexion is edge-on. (c) HRTEM image of an AIF in Cu-4Hf, showing the potential measurement error when taking care to measure from the thinnest region of the AIF. A maximum thickness variation of less than 0.1 nm is found.

Measurements are taken from the thinnest observed region of the AIF, with care taken to ensure a perfect edge-on viewing condition. Figure 2-8(c) shows that the maximum variation in thickness is less than 0.1 nm, meaning that the human error introduced from the thickness measurement is extremely small. The data in Figure 2-9 is plotted with both a linear scale and a logarithmic scale along the X-axis, to better show the differences in the curves.

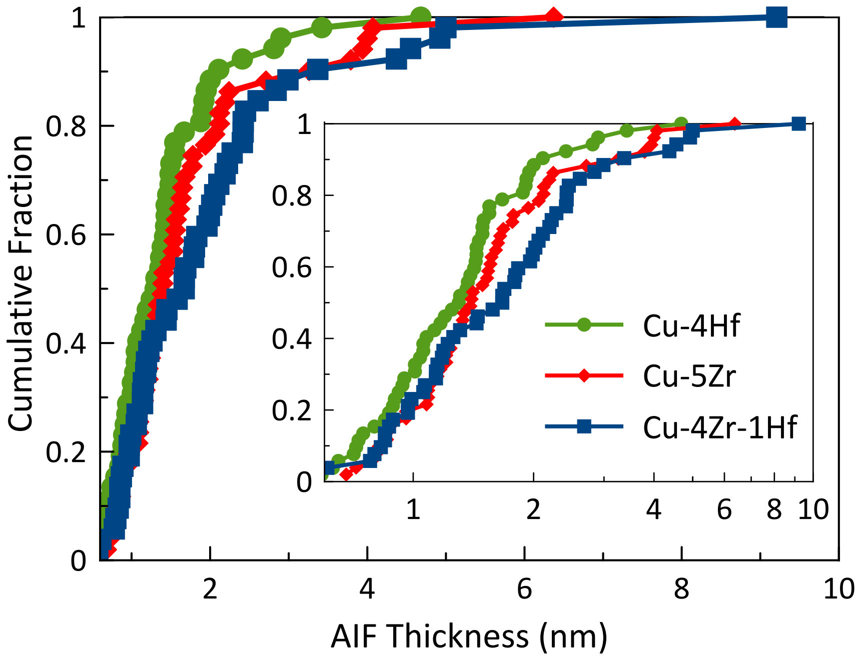

Figure 2-9: Cumulative distribution function of AIF thicknesses in Cu-5Zr, Cu-4Hf, and Cu-4Zr-1Hf alloys annealed for 1 week. At least 50 AIFs were measured from HRTEM micrographs of grain boundaries in an edge-on condition in each of the three samples. Distributions pushed to the right indicate thicker AIFs. Complexions in the Cu-4Zr-1Hf alloy are noticeably thicker than those found in binary alloys.

This data shows that the ternary Cu-4Zr-1Hf alloy is able to form the thickest AIFs, with the cumulative fraction curve furthest to the right in the figure. Analysis of the mean AIF thickness shows that the ternary Cu-4Zr-1Hf alloy (average AIF thickness of 1.85 nm) has AIFs that are on average ~9% thicker than the binary Cu-5Zr alloy (average AIF thickness of 1.7 nm). However, the usage of the mean suppresses some detail, and a more nuanced analysis can be performed on the data set. The cumulative distribution functions of AIF thickness diverge significantly for the thickest ~60% of AIFs observed. The fact that the top half of the AIF thickness curve for the ternary alloy does not overlap at all shows that this material has a population of significantly thicker AIFs. To give another perspective, only 3.9% of AIFs measured in binary Cu-5Zr had thicknesses greater than 4 nm, while 10% of AIFs measured in Cu-4Zr-1Hf had thicknesses greater than 4 nm. It is important to note that this is the cleanest possible comparison among samples in this study, as the only difference between the Cu-5Zr and the Cu-4Zr-1Hf samples is the complexity of the dopant chemistry (the two samples have identical grain size, global dopant concentration, carbide volume fraction, carbide size, and carbide distribution throughout the sample), and a clear difference is found. Although a comparison to the Cu-4Hf sample is not as clean, since this specimen has a higher carbide volume fraction which can reduce the amount of dopant available for grain boundary segregation, we include this data for completeness. There is very little quantitative data about the distribution of AIF thickness available in the literature, so we believe it does add some value to include the raw data.

The advantages of introducing a second dopant element in order to create a ternary alloy composition has important implications regarding grain boundary segregation and the formation of thick, stable AIFs. The bulk metallic glass research clearly shows that a multicomponent composition helps to reduce the free energy penalty associated with the formation of an amorphous phase, and also stabilizes the amorphous phase by lowering the critical cooling rate necessary [68]. In addition, a previous study by Luo et al. has demonstrated that thicker AIFs are able to more easily accept dopant atoms, further increasing the grain boundary dopant concentration and AIF thickness due to this reduction in the free energy penalty [43]. We hypothesize that the ternary alloy composition most directly affects the AIF thickness, which in turn means that more dopant can be accepted by the boundary. This contrasts with a situation where the ternary composition directly leads to higher boundary concentrations, with the higher concentration leading to thicker films. However, a definitive answer to which event happens first or drives the overall behavior is beyond the scope of the present study.

Although we hypothesize that more heavily doped boundaries can sustain thicker AIFs, it is important to remember that alloys with higher global dopant concentrations may also have more precipitation, which can compete with grain boundary segregation. The data regarding the Cu-10Hf alloy in Figure 2-2 actually show that beyond a certain dopant concentration, the thermal stability of the alloy will be reduced due to the formation of a significant amount of larger carbide particles which do not assist in the pinning of grain boundaries and potentially wick away excess dopant from the fcc phase grain boundaries. It is apparent that in this alloy there is a significant propensity for HfC phase to form, so care must be taken to determine an ideal Hf concentration at which the thick AIFs still play the dominant role in stabilizing the microstructure. Similar behavior was observed in a study by Donaldson et al., in which it was found that annealing of nanocrystalline W-Cr led to the formation of Cr-rich grains similar in size to the W-rich grains, whereas the use of Ti as the dopant led to Ti segregation to grain boundaries upon annealing [19]. The decreased thermal stability of W-Cr as compared to the W-Ti system was attributed to the formation of the large dopant-rich particles throughout the microstructure, which essentially "stole" dopant atoms out of the grain boundaries. In addition to the global dopant concentration, the concentration ratio of dopant elements in ternary alloys is also an important factor that should be considered. Simulations in a prior study by Hu et al. demonstrated a correlation between global dopant concentration and AIF thickness in a binary Al-Cu and a ternary Al-Zr-Cu alloy with a 1:1 Cu:Zr concentration ratio [113]. However, it was also demonstrated that the film thickness could be substantially increased by increasing the ratio of Cu to Zr atoms, while still maintaining the same global dopant concentration.

The Cu-5Zr and Cu-4Zr-1Hf samples investigated in this study provide the cleanest possible comparison of the influence of dopant chemistry on amorphous film thickness. These two samples have the same grain size, carbide volume fraction, carbide size distribution, and spatial distribution of carbides throughout the microstructure, as previously shown in Figures 4(b) and 5(b). The only difference is that there are two types of atoms at the grain boundaries in Cu-5Zr (Cu and Zr atoms), while the boundaries are decorated with three types of atoms in Cu-4Zr-1Hf (Cu, Zr, and Hf atoms). Figure 2-9 shows that the ternary Cu-4Zr-1Hf alloy has significantly thicker AIFs, which can only be explained by the increased complexity of the grain boundary chemistry.

The formation of AIFs in ternary and multicomponent alloys will have some additional complications compared to similar complexions in binary alloys or single-phase systems. Complicating factors to consider include the potential competition between dopants for grain boundary adsorption sites, as well as attractive or repulsive interactions between different dopant elements [84] , both of which can significantly influence the propensity of an alloy to form AIFs. Previous studies by Zhou and coworkers have investigated the development and experimental validation of grain boundary phase diagrams for binary and multicomponent alloys [85]. These studies show that attractive interactions between dopant elements in the liquid phase led to higher grain boundary excess concentrations, which overpower any effects of site competition and promote grain boundary pre-wetting transitions and disordering at grain boundaries [84, 85]. The evidence of thicker AIFs in the Cu-4Zr-1Hf alloy than the Cu-5Zr alloy possessing the same global dopant concentration supports these findings. The formation of thicker AIFs on average is a sign that the free energy penalty for the formation of an amorphous phase has been reduced by the switch to a ternary grain boundary composition, since AIF thickness is inversely proportional to this energy [43]. The ternary alloy is found to have thicker complexions on average, indicating that the introduction of a second dopant element further stabilizes the amorphous complexion at the grain boundaries. The complexions found in the Cu-Zr-Hf are thicker than any found in metallic systems to date, including Ni-W [65], W-Ni [64], Mo-Ni [63], and Ni-Zr .

Schuler et al. [67] recently showed that AIFs can act to stabilize a nanocrystalline grain structure. AIFs fundamentally form because they have a lower overall energy compared to the "normal" type of grain boundary, which will consequently reduce the driving force for grain growth. In addition, heavy levels of dopant segregation should also kinetically limit grain boundary migration, as these dopants would have to diffuse along with the interface as it moves (or there would be an increase in system energy). The introduction of thicker AIFs to nanocrystalline metals is also desirable due to their demonstrated ability to significantly improve the ductility and fracture toughness of these materials [18, 70]. Pan and Rupert [18] showed that thicker AIFs can absorb more incoming dislocations before cracking, meaning that a polycrystalline sample should be more ductile with thicker AIFs distributed within its microstructure.

2.4 Conclusions

In this study, nanocrystalline Cu-Zr-Hf alloys were created by mechanical alloying in order to gain an understanding of their thermal stability and ability to form amorphous complexions. The microstructures of these alloys were compared to baseline binary Cu-Hf and Cu-Zr alloys to gain insight on the role of each dopant element in stabilizing the microstructure. We draw the following conclusions from the results reported here:

- All ternary alloys investigated in this study showed excellent thermal stability, retaining grain sizes well within the nanocrystalline regime after annealing for two weeks at a temperature above 95% of the solidus temperature for binary Cu-Zr and Cu-Hf alloys. The thermal stability is primarily attributed to the formation of thick amorphous intergranular films, with a minor contribution from HfC and ZrC precipitates located at the grain boundaries.
- Amorphous intergranular films were observed to form in all binary and ternary alloys investigated in this study. Thicker films were found in the ternary Cu-4Hf-1Zr, even when possessing the same global dopant concentration as a binary Cu-5Zr alloy. The introduction of a second dopant element to form a ternary composition in the grain boundary region reduces the energy penalty for AIF formation. Finally, the ternary alloy contained the thickest amorphous complexions observed to date in metallic materials.

The results of this study highlight the enhanced ability to form thick, stable amorphous intergranular films in nanocrystalline alloys by utilizing a ternary composition. Although the grain sizes for the Cu-5Zr and the Cu-Zr-Hf alloys were found to be very similar, the presence of many thick AIFs is advantageous for improving the ductility of a nanocrystalline material. The ability of AIFs to serve as dislocation sinks which can delay crack nucleation and therefore increase fracture toughness is a significant motivator in fabricating nanocrystalline materials for structural applications. The results of this study motivate future work into the investigation of the mechanical properties of ternary alloys with thick AIFs versus binary alloys with thinner, less stable AIFs.

3 High entropy complexions: Stabilizing nanocrystalline grains with thick amorphous intergranular films

3.1 Introduction

In Chapter 2, the addition of a second dopant element was found to increase the thickness of amorphous complexions as compared to binary alloys with the same dopant concentration. It was concluded that an increase in the chemical complexity at grain boundaries was found to allow for the formation of thicker amorphous complexions. Chapter 3 serves to extend this idea to multicomponent alloys. As most metals used in engineering applications are composed of more than three elements, the study of the formation of amorphous complexions in materials in which multiple alloying elements are present is of significant interest. In this chapter, three alloys (Cu-Zr-Hf-Mo-Nb, Cu-Zr-Hf-Nb-Ti, and Cu-Zr-Hf-Mo-W) are studied to compare the influence of chemical complexity on thermal stability of the nanocrystalline structure and the precipitation of secondary phases. As the co-segregation behavior of Zr and Hf to grain boundaries was already demonstrated to lead to the formation of thicker amorphous complexions, the Cu-Zr-Hf alloy is used as a base. Mo, Nb, Ti, and W are predicted to segregate well due to their large atomic size mismatches with Cu of 39%, 38%, 28%, and 40%, respectively. We find that the Cu-Zr-Hf-Nb-Ti alloy is the most thermally stable alloy of the three, with this alloy therefore chosen for more in-depth characterization of the grain boundary chemistry and structure. Zr, Nb, and Ti are observed to heavily segregate to the grain boundary in this alloy, creating a quaternary interfacial composition, which prevents significant grain growth even after 1 week at >95% of the melting temperature. This level of thermal stability is attributed to the high levels of chemical disorder at the grain boundary that is a consequence of the multi-component segregation. High resolution electron microscopy of the grain boundary structure shows that this quinary alloy contains amorphous complexions which are much thicker than those reports in the prior binary and ternary Cu-rich alloys. The amorphous complexions formed in the Cu-Zr-Hf-Nb-Ti alloy are found to be 32% thicker on average than those formed in the Cu-Zr-Hf alloy studied in Chapter 2, and 41% thicker on average than the Cu-Zr alloy discussed in the same chapter. The results discussed in this chapter demonstrate a direct correlation between chemical disorder at the grain boundaries and complexion thickness.

3.2 Materials and Methods

Alloy compositions were selected in order to maximize dopant segregation to grain boundaries, creating a high-entropy grain boundary composition. Schuler and Rupert [67] have outlined specific alloy selection criteria to maximize the ability to form amorphous complexions at grain boundaries in binary alloys, including a positive enthalpy of segregation, a negative enthalpy of mixing, and a large atomic size mismatch with the bulk phase. The formation of thick amorphous intergranular films has been previously demonstrated in a ternary Cu-Zr-Hf alloy, due to the co-segregation of Zr and Hf dopants to grain boundaries [76]. In order to investigate the effects of adding multiple dopant elements on the formation of amorphous complexions with high entropy compositions, Cu doped with 2 at.% Zr and 2 at.% Hf was used as a base alloy. Two additional dopant elements were added to the base Cu-2Zr-2Hf alloy in the amount of 2 at.% each to investigate interactions between different dopant elements and the influence on grain boundary segregation and thermal stability. Specifically, Mo, Nb, Ti, and W were chosen as dopant elements, due to the demonstrated segregation behavior of these dopants in binary Cu-Mo [67], Cu-Nb [114, 115], Cu-Ti [116], and Cu-W [117] binary alloys. Additionally, Mo, Nb, Ti, and W are predicted to segregate well due to the large atomic size mismatches with Cu of 39%, 38%, 28%, and 40%, respectively. While the large atomic size mismatch of dopant elements with Cu is an important consideration, the relative atomic size mismatch amongst dopant atoms themselves provides additional disordering at the grain boundary and may also help improve the disordering of the grain boundary phase. The atomic sizes of Zr and Hf are larger than Cu by 25% and 24%, respectively. While these dopant atoms are smaller than Mo, Nb, and W, the large variation in atomic size in these multicomponent alloys may also allow for a higher packing density and further frustration of the crystallization of amorphous complexions which are able to form.

Cu-2Zr-2Hf-2Mo-2Nb, Cu-2Zr-2Hf-2Nb-2Ti, and Cu-2Zr-2Hf-2Mo-2W alloys were formed via mechanical alloying in a SPEX SamplePrep 8000M Mixer/Mill. Starting Cu (Alfa Aesar, 99.99%, -170 + 440 mesh), Zr (Micron Metals, 99.7%, -50 mesh), Hf (Alfa Aesar, 99.8%, -100 mesh), Mo (Alfa Aesar, 99.95%, -100 mesh), Nb (Alfa Aesar, 99.8%, -325 mesh), Ti (Alfa Aesar, 99.5%, -325 mesh), and W (Alfa Aesar, 99.9%, -100 mesh) powders were alloyed in an argon atmosphere with a hardened steel mixing vial and milling media. A 10:1 ball-to-powder mass ratio, and an addition of 1 wt.% of stearic acid as a process control agent in order to prevent excessive cold welding. Prior to milling each of the desired alloys, pure Cu powder and 1 wt. % stearic acid was milled for 2 h and subsequently disposed of to coat the vial walls and milling media with a thin layer of Cu, limiting the contamination of the alloy with Fe from collisions with the hardened steel during milling. Confirmation of the chemical composition of the powders was performed using energy dispersive X-ray spectroscopy (EDS) in a Tescan GAIA3 scanning electron microscope (SEM). Measured compositions for each sample from EDS are shown in Table 1. While there is some deviations of the measured compositions from the target values, these are within the ~1 at.% error of EDS estimates and we quote the nominal composition values from here on out.

Alloy powders were sealed inside of quartz tubes under vacuum prior to annealing, in order to limit exposure to atmosphere which could cause the formation of additional phases such as oxides during heat treatment. The powders were first annealed at 500°C for 5 h in order to encourage the segregation of the various dopant elements to Cu grain boundaries. This was followed by an additional annealing treatment at 950 °C for 5 min (0.083 h), 1 h, and 1 week (168 h) to allow for the formation of amorphous complexions. We only quote the second annealing step when describing the powder microstructures in subsequent text, but remind the reader that all samples were first exposed to the lower temperature annealing treatment. The high temperature annealing step should provide the correct conditions for grain boundary premelting while also allowing for the investigation of the thermal stability of the microstructure. The powder samples were quenched at the end of the anneal in order to freeze in the equilibrium grain boundary structure at high temperatures, including any amorphous complexions that were able to form. The as-milled and annealed powders were then characterized using a Rigaku SmartLab X-ray diffractometer (XRD) with Cu Kα radiation and a 1D D/teX Ultra 250 detector. Phase identification, grain size measurements, and volume fraction determination of all phases were extrapolated from XRD patterns via Rietveld analysis using MAUD software [118]. The grain sizes of the Cu-rich phase in all as-milled alloy powders were in the range of 19-32 nm.

A sample of the Cu-2Zr-2Hf-2Nb-2Ti sample that was annealed at 950 °C for 5 min was created for inspection via transmission electron microscopy (TEM) via the focused ion beam (FIB) lift-out method using a Tescan GAIA SEM/FIB. Excess Ga^+ ion beam damage of the lamella caused during sample preparation was removed with a final 5 kV polish. Detailed characterization of the microstructure of this sample was performed in the TEM, including bright field TEM, selected area electron diffraction (SAED), high resolution transmission electron microscopy

(HRTEM) of the grain boundary structure, high-angle annular scanning transmission electron microscopy (HAADF STEM), and EDS were performed using a JEOL JEM-2800 TEM equipped with dual EDS detectors. The presence of second phases extracted from the XRD pattern was confirmed with SAED. The average grain size obtained from the XRD pattern was also confirmed by measuring >160 grains imaged using bright field TEM. The distribution of dopant elements throughout the sample microstructure was observed using EDS. Line scans allowed for the observation of dopant segregation or depletion at grain boundaries where amorphous complexions are expected to form. The influence of alloy chemistry on the thickness of amorphous complexions is investigated by measuring the thickness of 46 amorphous complexions imaged with HRTEM in an edge-on condition. The edge-on condition of each grain boundary was confirmed by verifying that no change in amorphous complexion thickness is observed when viewing it in under- and over-focused conditions.

3.3 Results and Discussion

XRD patterns of each of the three alloys in their as-milled state, as well as after annealing for 5 h at 500 °C, followed by anneals at 950 °C for 5 min, 1 h, and 1 week, are shown in Figure 3-1.

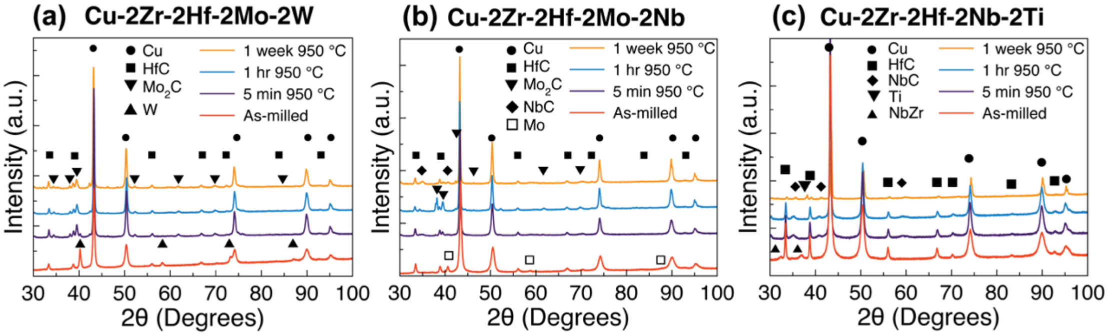

*Figure 3-1***:** *X-ray diffraction patterns of the (a) Cu-2Zr-2Hf-2Mo-2W, (b) Cu-2Zr-2Hf-2Mo-2Nb, and (c) Cu-2Zr-2Hf-2Nb-2Ti samples. Patterns are shown of the as-milled powders, as*

well as samples subject to an initial heat treatment at 500 ℃ for 5 h, followed by an anneal at 950 ℃ for 5 min, 1 h, and 1 week. Phase identification shows the presence of carbide phases and intermetallic phases which either formed during mechanical alloying or during annealing.

During mechanical alloying, HfC forms in all three alloys investigated in this study. The formation of carbide phases in the alloy during ball milling is due to the addition of stearic acid as a process control agent, which is necessary to resist cold welding [119]. However, in the patterns of the as-milled Cu-Zr-Hf-Mo-W and Cu-Zr-Hf-Mo-Nb powders in Figure 3-1(a) and Figure 3-1 (b), peaks for Mo and W are also seen, indicating that these alloying additions did not completely mix to form a solid solution with Cu during the mechanical alloying process. In the Cu-Zr-Hf-Nb-Ti sample, a very small amount of NbZr intermetallic phase (~1 vol.%) is seen in the as-milled powder, indicating its formation during the mechanical alloying process. In order to attempt to force all dopant atoms into the Cu matrix to form a solid solution and therefore have a more consistent starting point for the dopant atoms prior to annealing, the three alloys were mechanically alloyed once more for 20 h and 40 h. However, additional milling time did not help to further improve the alloying of these samples. The second phase volume fractions and XRD grain sizes of the second phases for the three alloys as a function of annealing time at 950 °C are shown in Figure 3-2.

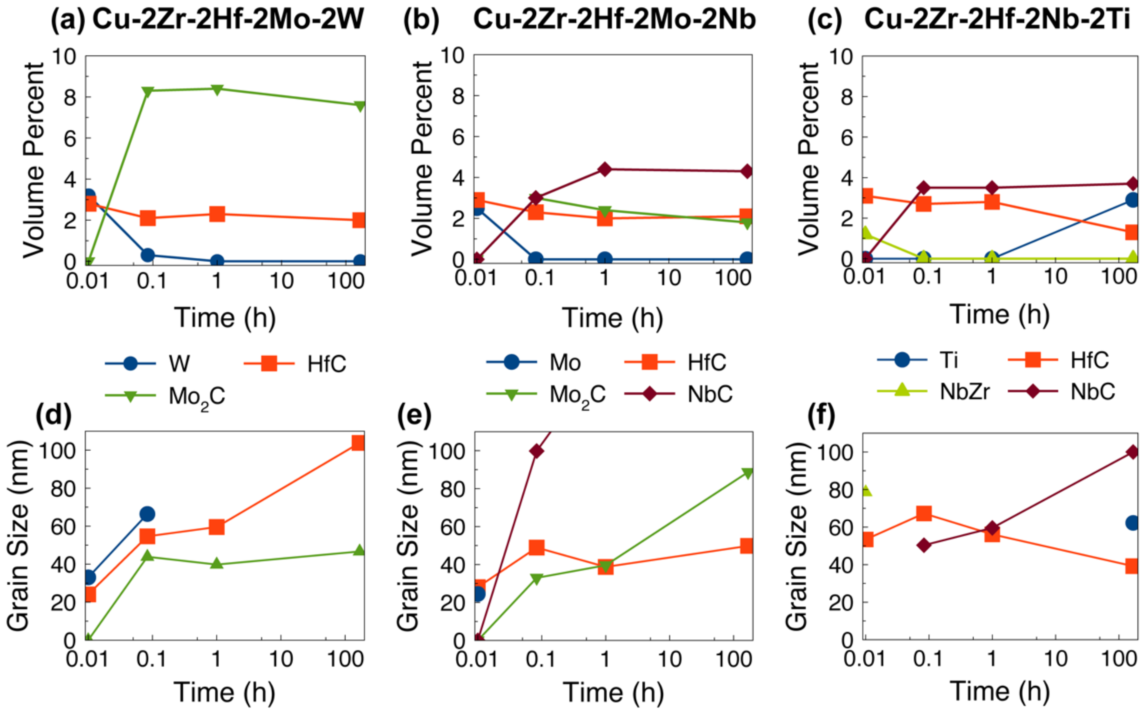

Figure 3-2: The volume fractions of second phases present in the (a) Cu-2Zr-2Hf-2Mo-2W, (b) Cu-2Zr-2Hf-2Mo-2Nb, and (c) Cu-2Zr-2Hf-2Nb-2Ti alloys are plotted as a function of annealing time at 950 °C. Grain sizes of these phases for each of the three alloys are shown in parts (d), (e), and (f). The Cu-2Zr-2Hf-2Mo-2W alloy has the greatest total volume fraction of second phases, while the Cu-2Zr-2Hf-2Nb-2Ti has the lowest volume fraction.

During heat treatment, the unalloyed W in the as-milled Cu-Zr-Hf-Mo-W becomes greatly reduced after 5 min at 950 °C and is fully gone after 1 h at 950 °C, while Mo_2C precipitates form during annealing. In the Cu-Zr-Hf-Mo-Nb alloy, the peaks for unincorporated Mo disappear while Mo_2C peaks appear, in addition to the formation of a new NbC phase. Upon annealing the Cu-Zr-Hf-Nb-Ti sample, the NbZr intermetallic phase is no longer found within the microstructure, but a small amount of NbC phase appears. The amount of the NbC phase present stays constant at 3.5 vol.%, with a slight increase in grain size of this carbide phase as annealing time increases. After annealing for 1 week, a small amount of Ti-rich hexagonal close packed phase also begins to precipitate.

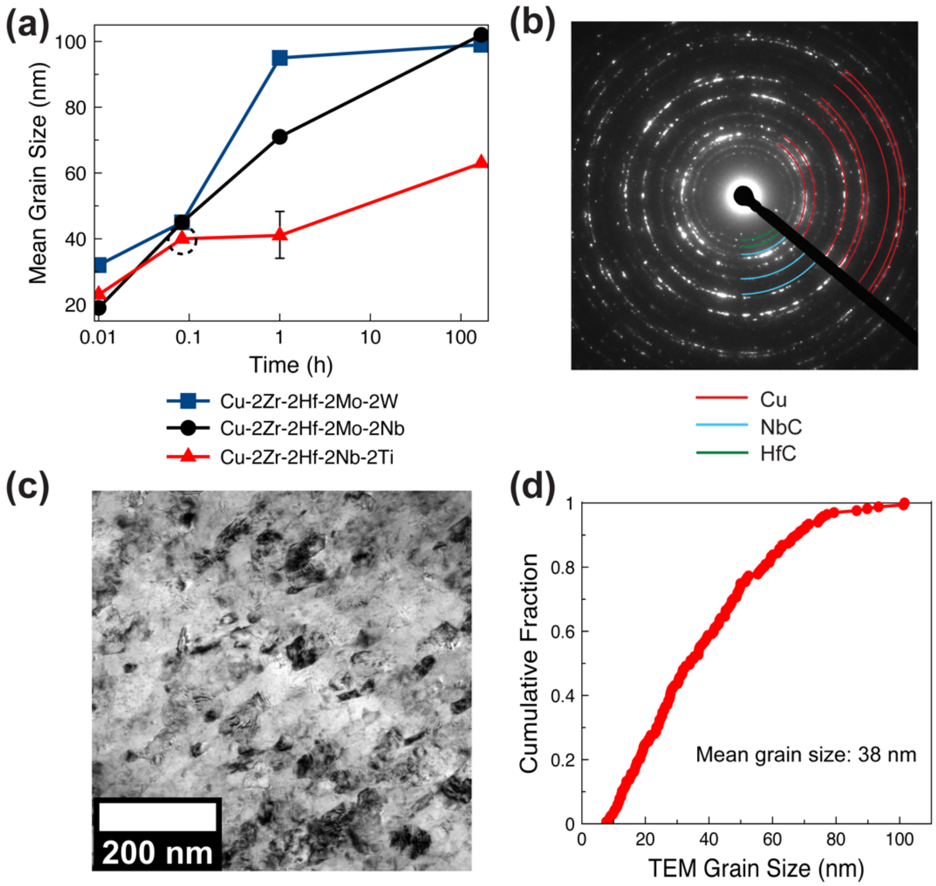

Figure 3-3: (a) Grain size of each of the three alloys plotted as a function of annealing time at 950 °C. The Cu-2Zr-2Hf-2Nb-2Ti alloy is the most stable against grain growth in this study, retaining a grain size of 63 nm after a week of annealing. (b) SAED pattern confirming the presence of NbC and HfC phases in the Cu-2Zr-2Hf-2Nb-2Ti alloy annealed for 5 min at 950 °C. (c) Bright field TEM micrograph of the microstructure of the Cu-2Zr-2Hf-2Nb-2Ti sample annealed for 5 min. Grain size distributions for this sample are shown in (d), after measuring 167 grains.

The XRD grain sizes of the face centered cubic Cu-rich phase (the majority or matrix phase) as a function of annealing time at 950 °C are reported in Figure 3-3(a). After 5 min of annealing at 950 °C, the grain sizes of all three alloys are very similar, within error for XRD measurements of grain size. However, after only 1 h of annealing, the difference in grain sizes highlight their relative thermal stability; the Cu-Zr-Hf-Nb-Ti alloy has an average grain size of 43 nm, while the Cu-Zr-Hf-Mo-W and Cu-Zr-Hf-Mo-Nb alloys both coarsen noticeably to average grain sizes of 95 and 71 nm, respectively. The high thermal stability of the Cu-Zr-Hf-Nb-Ti alloy is further demonstrated by the relatively small grain size of 63 nm after 1 week (168 h) of annealing, while the average grain sizes of the Cu-Zr-Hf-Mo-W and Cu-Zr-Hf-Mo-Nb alloys continue to grow to 98 nm and 102 nm, respectively. It is important to note that these grain sizes approach the resolution limit of roughly 100 nm for XRD measurements of crystallite size, so it is possible that these samples no longer have a nanocrystalline microstructure after 1 week of annealing. Further inspection of these samples using TEM would be necessary to confirm the accuracy of these grain size measurements, i.e. whether the Cu-Zr-Hf-Mo-W and Cu-Zr-Hf-Mo-Nb samples are coarse-grained after this heat treatment, or at the upper end of the nanocrystalline size regime. The decreased thermal stability in the Cu-Zr-Hf-Mo-W and Cu-Zr-Hf-Mo-Nb may be attributed to the early precipitation of second phases during annealing. Figure 3-2(a) shows that the overall volume of second phases throughout the microstructure of the Cu-Zr-Hf-Mo-Nb alloy increases from roughly 0.054 in the as-milled state to 0.089 after only 1 h of annealing. In the Cu-Zr-Hf-Mo-W microstructure, however, the increase in the total second phase volume fraction is greater, growing from 0.06 in the as-milled state to 0.108 after 1 h of annealing, with this value staying relatively constant with further annealing time. With the precipitation and growth of such second phases, there will be much fewer dopant atoms available to segregate to grain boundaries in the Cu-Zr-Hf-Mo-W and Cu-Zr-Hf-Mo-Nb alloys, potentially reducing the thermodynamic stabilization of the microstructure and allowing for grain growth. Additionally, the average sizes of the second phase particles within the Mo-W alloy are too large to maintain kinetic stabilization of a nanocrystalline microstructure via Zener pinning of the grains [120, 121]. The Cu-Zr-Hf-Mo-Nb coarsens more gradually than the Cu-Zr-Hf-Mo-W alloy, which is likely related to the greater availability of grain boundary segregating species. In contrast, the Cu-Zr-

Hf-Nb-Ti alloy maintains the smallest total second phase volume even after one week of annealing at 950 °C, and at the same time is able to retain a grain size of 63 nm. The correlation of thermal stability and the amount of dopant content available to segregate to the boundaries (i.e., the inverse of the second phase volume percent) amongst the three alloys suggests that boundary segregation is the dominant stabilizing mechanisms in these materials, not Zener pinning.

Due to its superior thermal stability, the Cu-Zr-Hf-Nb-Ti sample was chosen for further investigation via TEM, in order to discern the distribution of each dopant to the grain boundary regions. The grain boundary structure of this alloy is also investigated in detail to determine whether the addition of multiple dopant elements is conducive to the formation of thick amorphous intergranular films. The sample which was annealed for 5 min at 950 °C was chosen for this investigation.

A selected area electron diffraction (SAED) pattern and bright field TEM image of the sample region from which the pattern was taken are shown in Figures 3(b) and 3(c), respectively. The SAED pattern confirms the presence of the NbC and HfC phases previously detected with XRD, while the TEM image confirms the nanocrystalline grain size. Figure 3-3(d) presents the grain size distribution measured in this sample, with an average grain size of 38 nm, which is in agreement with the previously measured XRD average grain size of 43 nm (XRD measurements typically are assumed to have up to 25% error). This sample was also viewed in HAADF STEM conditions, where bright contrast at grain boundaries indicate regions of segregation of higher Z atoms, such as Nb, Zr, and/or Hf, pointed out by the yellow arrows in Figure 3-4.

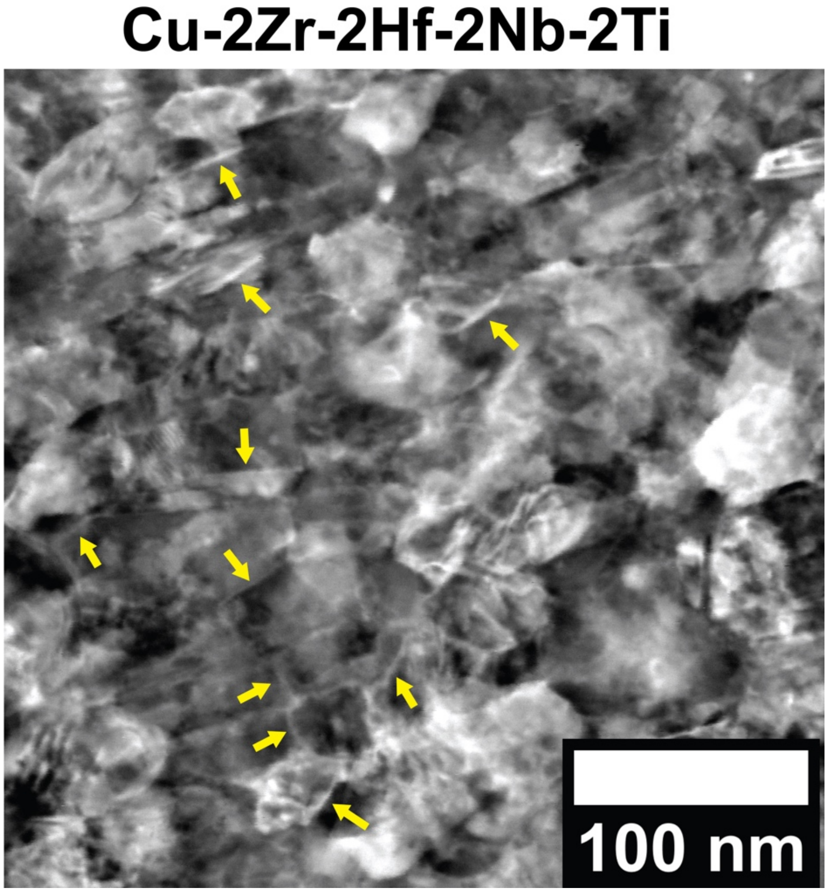

Figure 3-4: HAADF STEM micrograph of the Cu-Zr-Hf-Nb-Ti alloy. Yellow arrows point to regions of bright contrast at grain boundaries, associated with dopant segregation and the possible formation of amorphous complexions.

As seen in the figure, the majority of grain boundaries appear to be decorated with higher Z dopant elements, evidenced by the bright contrast. EDS line scans were performed across grain boundaries with high contrast in order to confirm the presence of dopant segregation. The yellow lines in Figures 5(a) and 5(c) indicate the locations where the line scans shown in Figures 5(b) and (d) were taken, respectively.

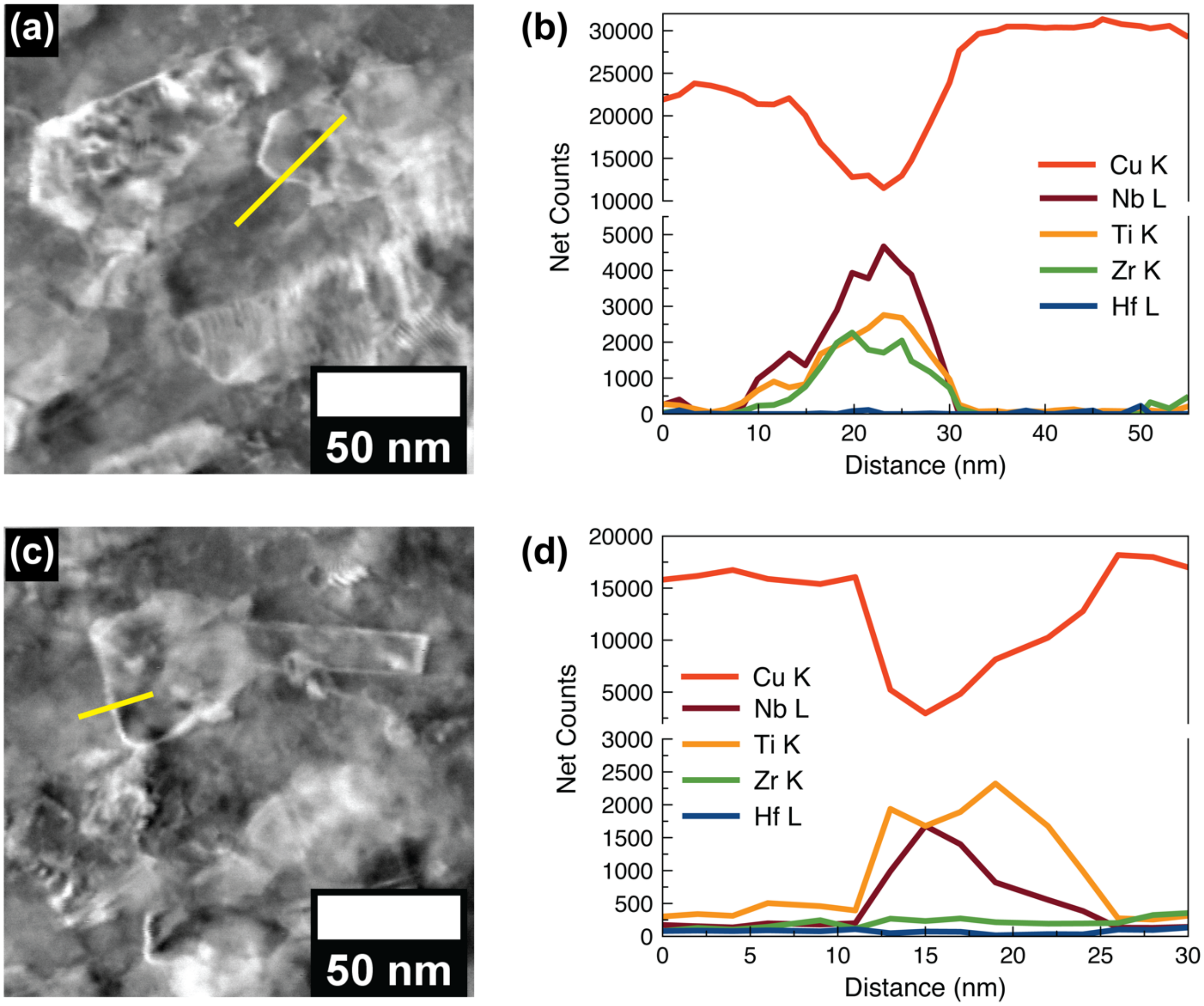

Figure 3-5: (a) HAADF STEM micrograph and (b) corresponding line scan across a grain boundary in Cu-2Zr-2Hf-2Nb-2Ti. The segregation of Nb, Ti, and Zr atoms to this grain boundary is observed, as well as the depletion of Hf. (b) A HAADF STEM micrograph and (c) corresponding line scan demonstrate the variation of possible grain boundary segregation behavior in this alloy, where the boundary is found to be enriched with both Nb and Ti, but depleted of Zr and Hf.

Both EDS scans show heavy segregation to the boundaries, but the dopants which are present changes. In Figure 3-5(b), the segregation of Nb, Ti, and Zr are clearly observed at the grain boundary, confirming the feasibility of forming high-entropy compositions at grain boundaries where at least 4 elements are present. In contrast, the line scan in Figure 3-5(d) demonstrates that only Nb and Ti are present and no Zr segregation is observed. In both cases, Hf was not observed in either the grain boundary or crystalline regions. These observations are representative of XX such measurements of the While the presence of Zr was found to vary across different grain boundaries, the co-segregation of Nb and Ti atoms was found to be consistent across all boundaries characterized. However, segregation of Hf was not found at any grain boundaries in this study. The variation in grain boundary chemistries seen here is similar to that seen in a prior study of Cu-Zr-Hf alloys, but the segregation of Hf atoms to the grain boundaries was observed in those alloys [76]. It is possible that the presence of Hf at grain boundaries is more likely to be observed as the volume fraction of HfC significantly decreases after annealing for a week, as shown in Figure 3-2 (c). It is reasonable to expect that the variation in second phases present throughout the microstructure of the Cu-Zr-Hf-Nb-Ti alloy with annealing time may also incur changes in grain boundary chemistry, and therefore induce grain boundary phase transitions.

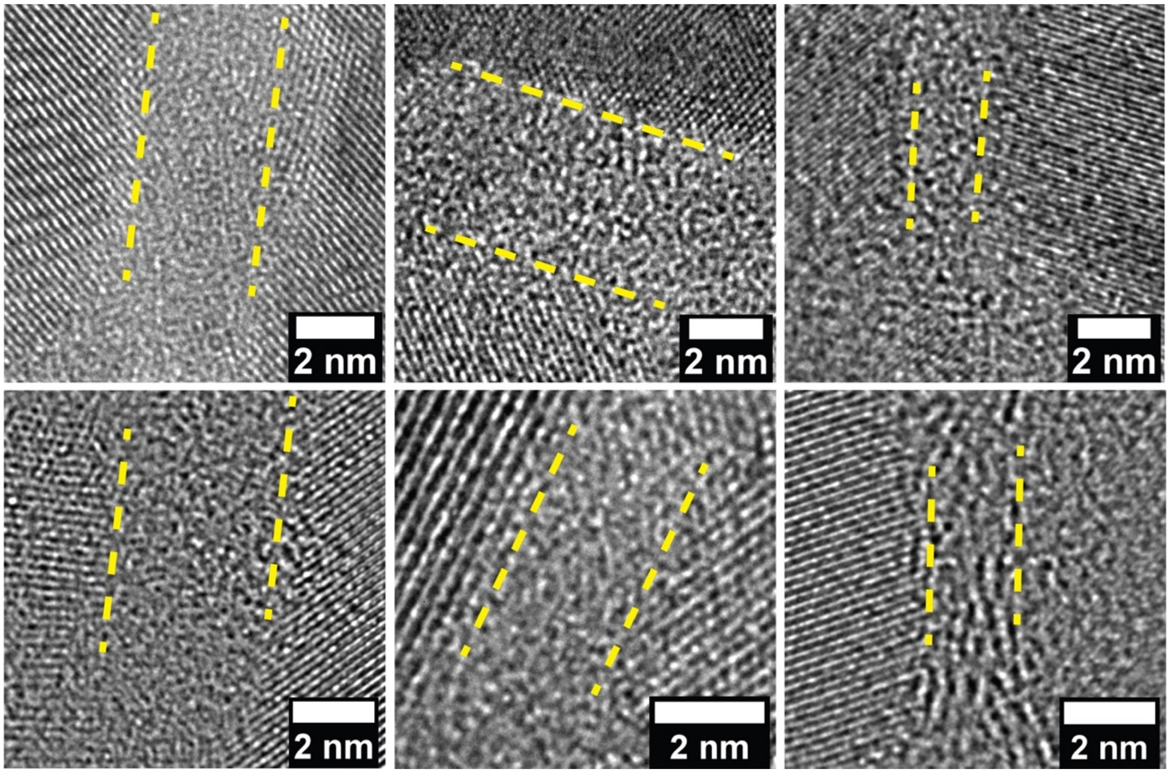

Figure 3-6: HRTEM micrographs of various amorphous complexions found in the Cu-2Zr-2Hf-2Nb-2Ti alloy. Yellow dashed lines are included to highlight the amorphous phase.

HRTEM micrographs of amorphous intergranular films in the Cu-Zr-Hf-Nb-Ti sample annealed for 5 min are shown in Figure 3-6. Yellow dotted lines are included to highlight the boundaries of the amorphous complexion. While amorphous complexions were found at grain boundaries throughout the microstructure of this sample, they are not found at every single grain boundary and some remained ordered. Figures 7(a) and 7(b) show the population of amorphous complexion thicknesses measured for 46 amorphous complexions in cumulative distribution function and histogram form, respectively. It is important to note that all amorphous complexions in this study were observed and measured in an edge-on viewing condition. In addition, thickness measurements were taken from the thinnest observable region of the complexion to ensure consistency. The mean thickness of amorphous complexions in this sample was found to be 2.44

nm, with a standard deviation of 1.36 nm. In order to compare the thicknesses of amorphous complexions found in the Cu-Zr-Hf-Nb-Ti sample with high-entropy grain boundary compositions with those found in previously studied Cu-4Zr-1Hf and Cu-5Zr alloys [76], the complexion thickness distributions for these samples are plotted in Figure 3-7(a) in grey and black, respectively. The average complexion thickness of the ternary sample from the prior study was found to be 1.85 nm. It is apparent that the quinary alloy is able to form much thicker complexions than those formed in the ternary alloy, due to the increase in average complexion thickness by roughly 32%. While the range of complexion thicknesses measured in the ternary and quinary samples are the same, there are a larger number of very thick amorphous complexions in the quinary alloy than in the ternary alloy. For example, roughly 30% of amorphous complexions measured in the quinary sample have a thickness greater than 3 nm, compared to only 10% of those measured in the ternary alloy. This can be attributed to the addition of multiple dopant elements which segregate to Cu grain boundaries in the quinary alloy.

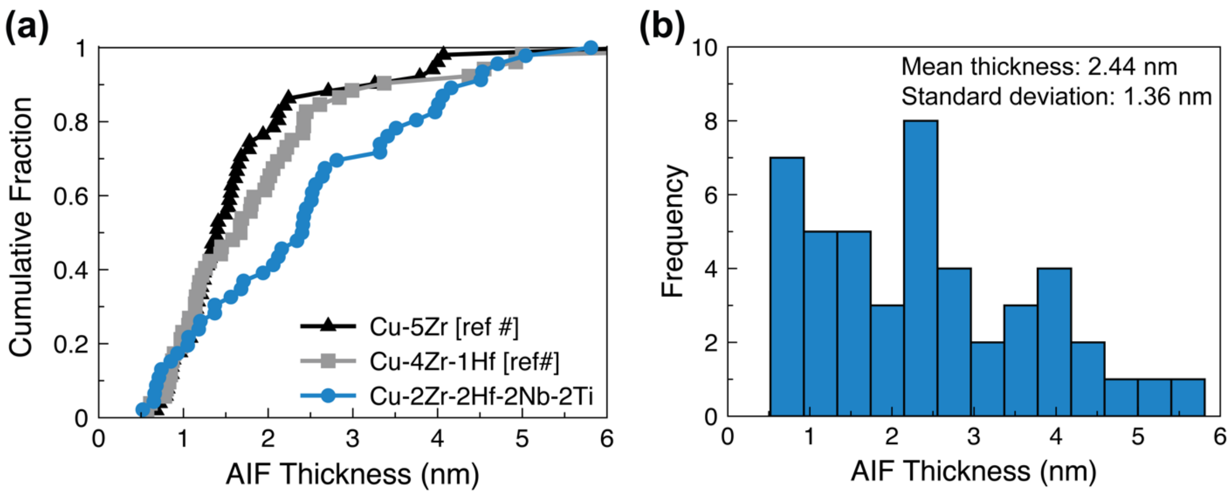

Figure 3-7: (a) Cumulative distribution function of AIF thicknesses measured from the Cu-Zr-Hf-Nb-Ti sample. 46 AIFs were measured from HRTEM micrographs of grain boundaries in an edge-on condition. AIF thicknesses from a prior study of Cu-4Zr-1Hf are plotted alongside the data from the present study to demonstrate the increased amorphous film thickness associated with a more complex grain boundary chemistry. (b) AIF thicknesses measured from the Cu-Zr-Hf-Nb-Ti sample, presented in a histogram. The mean AIF thickness was found to be 2.44 nm, with a standard deviation of 1.36 nm.

While the increased thickness of amorphous complexions found in quinary alloys may be at first attributed to the increase in the global dopant concentration (8 at. % dopant in the quinary, versus 5 at. % in the ternary), it is worth noting that the difference in the distribution of the dopant elements actually allows for a more even comparison. In the Cu-Zr-Hf alloy, Hf atoms were shown to segregate to grain boundaries, however, there was no segregation of Hf atoms to any grain boundaries observed in the Cu-Zr-Hf-Nb-Ti alloy. This implies that a maximum of only 6 at. % of the total 8 at. % of dopant atoms added to the quinary alloy are capable of contributing to the formation of complexions, since only Zr, Nb, and Ti atoms were found at grain boundaries. However, yet another fraction of those dopant atoms which do segregate to grain boundaries are consumed during the formation of second phases. It is therefore reasonable to assume that the difference in the total number of dopant atoms available to contribute to the formation of amorphous complexions is quite small, and cannot fully explain the 32% difference in average amorphous film thickness alone, and it is more likely due to the presence of a greater number of dopant elements.

The increased thickness of amorphous complexions in the quinary alloy may be in part due to the greater number of dopant atoms which are available to segregate to grain boundaries to form amorphous complexions. However, it is important to consider the effects associated with multiple dopant elements present at grain boundaries in order to stabilize the amorphous grain boundary phase, as well as the influence of second phase formation on the formation of amorphous complexions. For example, the prior study on amorphous complexion formation in Cu-Zr-Hf alloys also demonstrated their formation in Cu-4Hf alloys which displayed excellent thermal stability; however, increasing the dopant concentration to 10 at. % Hf actually proved to be detrimental to the thermal stability of the alloy. The formation of a large volume of HfC particles throughout the microstructure was hypothesized to have decreased the amount of dopant available to segregate to grain boundaries, inhibiting the formation of amorphous complexions and therefore limiting the stabilization of grain size in this alloy. Such behavior has been observed in nanocrystalline W-Cr alloys in a study by Donaldson et al., where the precipitation of a Cr-rich phase was found to reduce the thermal stability of the alloy due to the lack of Cr atoms present at grain boundaries [19]. In contrast, a Cu-10 at.% Zr alloy investigated in the prior study proved to be more stable against grain growth than the Cu-5 at.% Zr alloy, implying that Zr atoms may have a stronger tendency to segregate to grain boundaries to facilitate amorphous complexion formation than Hf alloys. These results highlight the fact that the formation of thick AIFs is not as simple as increasing the concentration of dopant atoms in the alloy. The addition of multiple dopant elements to an alloy creates even more complications for grain boundary segregation, where attractive or repulsive forces between dopant atoms themselves may encourage co-segregation of particular elements or cause the depletion of others.

The interaction between dopant elements in ternary and multicomponent alloys in the context of grain boundary segregation is an important topic of consideration in the formation of thick and stable AIFs in metals. Prior studies by Xing et al. have investigated the interactions between dopants and their influence on grain boundary segregation in ternary and multicomponent alloys [122, 123]. It was found that induced co-segregation of dopant atoms can occur, even when a particular dopant element is predicted to desegregate from grain boundaries in the binary counterpart, as was the case in the Pt-Au-Pd alloy investigated [123]. The authors were able to develop a model to predict the segregation behavior of dopant elements in a ternary alloy and whether there would be dopant depletion, site competition, or induced co-segregation of the dopants to grain boundaries. The materials selection rules for the formation of AIFs in binary alloys suggest choosing dopant elements which have a positive ΔH_{seg}, a negative ΔH_{mix}, and an atomic size mismatch of greater than 12% [67]. By these standards, it would be expected that AIFs would not form in a binary Cu-Nb alloy, due to the positive ΔH_{mix} value calculated, indicating that it would be preferable for the precipitation of a Nb-rich phase to occur [124, 125]. However, AIFs were still found to form in the Cu-Zr-Hf-Nb-Ti alloy, with the co-segregation of Nb and Ti to grain boundaries to be a common occurrence. This highlights the complexity associated with effectively selecting dopant elements which will allow for the formation of AIFs, due to the additional interactions between individual dopant elements which must be accounted for. This behavior has been observed in a variety of alloys, where the addition of dopant has been proven to either inhibit or enhance the segregation behavior of the other dopant elements. This phenomenon is well studied and has significant effects on the mechanical behavior of steels. For example, Mo and P are found to co-segregate to grain boundaries in steels, where the concentration of P at grain boundaries increases with that of Mo [126]. In contrast, the addition of C to Fe-P alloys is found to decrease the amount of P segregating to grain boundaries, suppressing the grain boundary embrittlement caused by P segregation [127-129]. However, it was also found that Cr additions increase the grain boundary segregation of P in Fe-C-P alloys, but has no effect in Fe-P alloys [127]. The variation in segregation behavior that can be introduced by the presence of multiple alloying elements may provide an explanation as to why no segregation of Hf was observed in the Cu-Zr-Hf-Nb-Ti sample, while it was previously observed in the ternary Cu-Zr-Hf alloy. This may also explain the relatively poor thermal stability observed in both the Cu-Zr-Hf-Mo-W and Cu-Zr-Hf-Mo-Nb samples investigated in this study. This behavior can also be examined by comparing the volume fractions of second phases containing Mo in the Cu-Zr-Hf-Mo-W and Cu-Zr-Hf-Mo-Nb alloys. During annealing, the maximum amount of Mo_2C which forms in the Mo-Nb alloy is only 3 vol.%, while a much greater maximum 8.4 vol.% forms in the Mo-W alloy. This implies that there may be some repulsive interaction between Mo and W atoms which prevents the segregation of Mo to grain boundaries, limiting the number of dopant atoms available to form amorphous complexions and stabilize the microstructure.

The current guidelines available for materials selection rules to enable the formation of amorphous complexions in binary metallic alloys developed by Schuler and Rupert [67] are largely based on guidelines proposed by Inoue for the formation of bulk metallic alloys (BMGs), including a positive heat of segregation, a negative heat of mixing, and a large atomic size mismatch [68, 69]. These guidelines have been shown to be effective in predicting the formation of amorphous complexions in a variety of binary alloy systems, and do provide an effective baseline for the formation In the context of bulk metallic glasses, these guidelines are considered when developing

BMGs in order to maximize their glass forming ability, as well as the use of three or more elements in order to frustrate the crystallization of the amorphous phase. Glass forming ability is typically characterized by the critical cooling rate required to retain the amorphous structure, or the critical thickness, describing the maximum size of a glassy phase that can be achieved upon cooling, essentially describing the resistance of the glassy phase to transformation back to an ordered phase [86, 130, 131]. Several studies have demonstrated the enhanced glass forming ability with the addition of multiple alloying elements in bulk metallic glass. This effect is expected to carry over to amorphous intergranular films; the thickness of amorphous complexions found in the Cu-Zr-Hf-Nb-Ti alloy investigated in this present study were found to be 32% thicker than those found in a previously studied Cu-Zr-Hf alloy. The increased thickness of the complexions in the present study analogously describe a greater resistance to transformation back to ordered grain boundary complexions, due to the increased chemical and structural disorder induced by the presence of multiple dopant elements. This implies that a lower cooling rate may be utilized in order to retain the amorphous grain boundary structure due to the enhancement of the phase stability. These findings have great implications for the development of bulk nanocrystalline alloys containing amorphous complexions, as a reduction in the cooling rate necessary to retain amorphous complexions would simplify the formation of these materials, enabling their utilization in a variety of appropriate lower temperature applications.

3.4 Conclusions

In this study, three quinary alloys were formed via mechanical alloying and annealed in order to understand the thermal stability and potential for amorphous complexion formation in each alloy. Dopant elements (Mo, W, Nb, Ti) were added to a Cu-Zr-Hf base material in different combinations but with a consistent total doping level. The following conclusions can be drawn:

- Second phase formation was observed in the Cu-Zr-Hf-Mo-W, Cu-Zr-Hf-Mo-Nb, and Cu-Zr-Hf-Nb-Ti alloys investigated in this study, primarily in the form of carbide phases but also with some secondary metallic phases appearing. The grain size of the bulk face centered cubic phase observed in each alloy had a positive correlation with the second phase volume, meaning that precipitation “robbed’ the grain boundaries of potential dopant species so there were fewer atoms available to segregate and reduce excess grain boundary energy. Kinetic stabilization of the microstructure by Zener pinning was not a dominant effect in this study.
- The Cu-Zr-Hf-Nb-Ti was found to have the greatest thermal stability, retaining a grain size of 63 nm after a week of annealing at 950 °C, or >95% of the melting temperature of Cu. The superior thermal stability of this alloy is attributed to the segregation of Zr, Nb, and Ti atoms to grain boundaries, enabling the formation of thick amorphous intergranular films with chemically complex compositions. As a result, the interfacial complexions in this alloy can be termed “high-entropy complexions.” The complexions measured in this study were found to be 32% thicker than those found in a previously studied Cu-Zr-Hf alloy, and 41% thicker than those found in a Cu-Zr alloy from the same study. The increased complexity in grain boundary composition is expected to enhance the stability of the amorphous intergranular film, allowing for the retention of thicker complexions upon quenching from high temperatures.
- The addition of multiple dopant elements significantly effects the segregation behavior. Hf atoms, which were previously found to segregate to grain boundaries in a prior study of Cu-Zr-Hf alloys, did not segregate in the Cu-Zr-Hf-Nb-Ti alloy investigated in the present study, instead being consumed by the carbide second phases. The competition

between elements for grain boundary segregation, as well as the balance between segregation and second phase formation for a specific atomic species, remains an open area for future research.

The results of this work demonstrate the improvement of amorphous intergranular film thickness through the utilization of high-entropy grain boundary compositions. This work also highlights the complications associated with grain boundary segregation and amorphous complexion formation in multicomponent alloys, due to the variety of interactions between different dopant elements. This work motivates experimental and computational studies to further the understanding of alloy selection for the formation of amorphous complexions beyond binary and ternary chemistries, as well as characterizing the arrangement of the various dopant atoms within the amorphous complexions themselves.

4 Critical cooling rates for amorphous-to-ordered complexion transitions in Cu-rich nanocrystalline alloys

4.1 Introduction

In Chapters 2and 3, the dependence of amorphous complexion thickness on the chemical complexity at the grain boundary is demonstrated in a ternary Cu-Zr-Hf alloy and a quinary Cu-Zr-Hf-Nb-Ti alloy. The ability to form thick amorphous complexions is promising in their ability to stabilize nanocrystalline microstructures, as well as improving strength and ductility. However, the stability of these phases has yet to be investigated. Amorphous complexions are able to form and are stable at high temperatures, and very fast quench rates must be utilized in order to retain them at room temperature. This severely limits the utility of nanocrystalline metals with amorphous complexions for lower temperature applications. In Chapter 4, the influence of grain boundary chemistry on the stability of amorphous complexions is explored. A cooling rate gradient through the height of bulk Cu-Zr and Cu-Zr-Hf samples. Amorphous complexion thicknesses were then measured at various heights throughout the binary and ternary alloys, in order to assess the stability of the phase against transformation back to ordered grain boundaries when exposed to a variety of cooling rates. A positive correlation between local cooling rate and complexion thickness is revealed in the binary Cu-Zr alloy. In contrast, the complexion thicknesses in the ternary Cu-Zr-Hf alloy are found to be invariant with local cooling rate, demonstrating an enhancement in stability of the amorphous complexion with increasing chemical complexity. The experimental results are then used to construct time-temperature-transformation diagrams of the amorphous-to-ordered complexion transition for both the binary and ternary alloys. The critical cooling rate necessary to avoid complexion transitions in the ternary alloy is found to be at least three orders of magnitude slower than that for the binary alloy. These results reveal the importance of increasing chemical complexity in improving both the thickness and stability of amorphous complexions. This increases the feasibility of utilizing nanocrystalline metals with amorphous complexions in lower temperature applications.

4.2 Materials and Methods

Cu-3 at.% Zr and Cu-2 at.% Zr-1 at.% Hf alloys were produced from powders of elemental Cu (Alfa Aesar, 99.99%, -170 + 400 mesh), Zr (Micron Metals, 99.7%, -50 mesh), and Hf (Alfa Aesar, 99.8%, -100 mesh). The total global dopant concentration was chosen to be constant at 3 at.% to best compare the complexion transition behavior between the binary and ternary alloys. These samples are simply referred to from here on as Cu-Zr and Cu-Zr-Hf, respectively. The starting powders were ball milled for 10 h in a SPEX SamplePrep 8000M high-energy ball mill using a hardened steel vial and milling media. A ball-to-powder weight ratio of 10:1 was used with 1 wt.% stearic acid added to the powders prior to milling as a process control agent, in order to prevent excessive cold welding of the powders. The individual alloy compositions were confirmed using energy dispersive X-ray spectroscopy (EDS) in a Tescan GAIA3 scanning electron microscope (SEM) equipped with a 150 mm^2 Si drift detector. Following the mechanical alloying process, phase identification and grain size determination for the as-milled powders were performed in a Rigaku SmartLab X-ray diffractometer (XRD). The resulting Cu-Zr and Cu-Zr-Hf alloys had grain sizes of 25 and 29 nm, respectively, measured via Rietveld refinement of XRD patterns using MAUD analysis software [99].

The alloy powders were consolidated to form bulk samples using an MTI Corporation OTF-1200X-VHP4 hot press. The powders were first cold pressed under 25 MPa for 10 minutes in a graphite die. The resulting green bodies were then hot pressed under 50 MPa for 10 hours at a temperature of 900 °C, allowing for full densification of the samples, as well as the segregation of dopant elements to the grain boundaries. According to prior work by Donaldson and Rupert investigating the densification behavior of Cu-4Zr alloys with amorphous complexions, the relative density of bulk samples formed under these particular pressing conditions was found to be 99.7% [79]. It is important to note that while amorphous complexions do form at grain boundaries during sintering, they are not retained after this process due to the slow cooling of the bulk piece back to room temperature while in the hot press, which allows time for the glassy interfacial complexion to transition back to an ordered structure. The resulting cylindrical bulk samples had a height of 6.47 mm and a radius of 5.34 mm, and were cut in half lengthwise to form a semi-cylinder, as shown in Figure 4-1(a), prior to subsequent annealing in a tube furnace at 950 °C for 10 minutes to re-form the amorphous complexions. The samples are then removed from the furnace as quickly as possible and placed on an Al heat sink that is cooled by a liquid nitrogen reserve (Figure 4-1(a)). This allows for the sample to be rapidly cooled, while also inducing a gradient of cooling rates as a function of distance from the surface of the heat sink. The surface directly in contact with the aluminum (bottom) will be very quickly quenched compared to the interior (middle) and opposite side of the sample (top). A thin oxide film formed at the surface of the sample upon transfer from the furnace to the Al block was removed prior to further processing. The semi-cylindrical samples were then cut in half once more to expose the center of the sample for characterization in order to investigate the effect of varying the cooling rate on the local grain boundary structure.

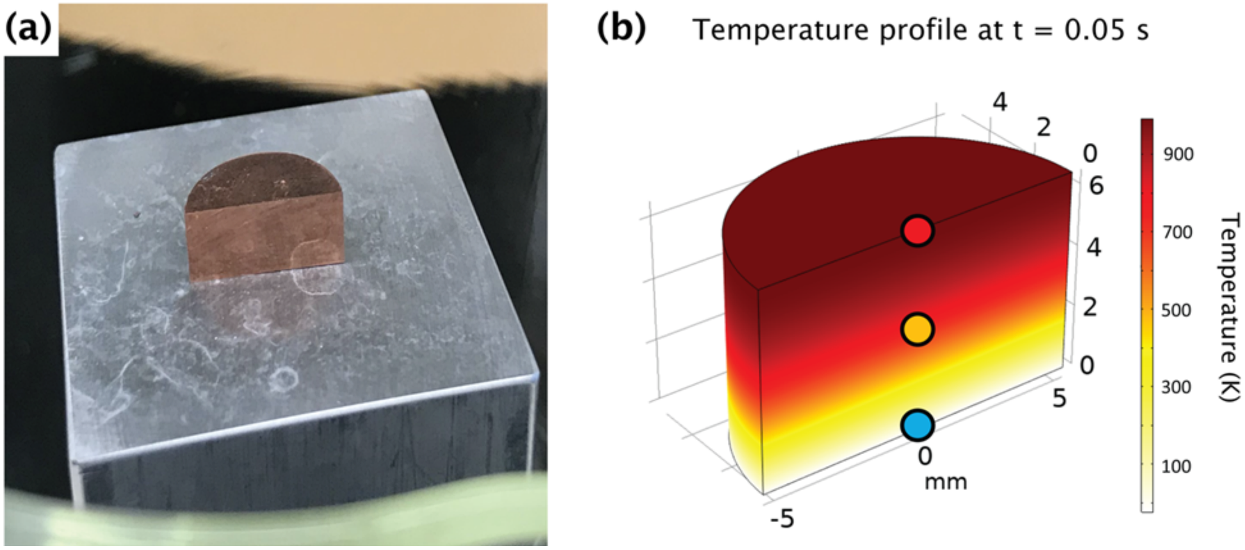

Figure 4-1: (a) Bulk nanocrystalline samples are exposed to variable cooling rates by placing on an Al cooling block in liquid nitrogen, following annealing at 950 °C for 10 min to re-form amorphous intergranular films at grain boundaries. (b) Temperature profile throughout the bulk sample at t = 0.05 s after contacting the cooling block, simulated using COMSOL Multiphysics software. The blue, orange, and red circles represent the fast, medium, and slow quenched locations on the sample, respectively.

The cooling rate gradient induced and its connection to the measured complexion population are expected to reveal the stability of the amorphous complexions against transformation to thinner complexions or ordered grain boundaries. The population of amorphous complexions which form in a particular alloy is associated with the alloy composition and the annealing temperature. However, the high temperature complexion population may differ from what is observed at room temperature, as some amorphous boundaries could transform back to an ordered grain boundary structure if the region is not quenched quickly enough. This is equivalent to what is observed regarding the nucleation of crystalline regions in BMGs when cooled below the critical cooling rate necessary to retain a completely amorphous microstructure [132, 133]. Complexion transformations may be even more sensitive to variations in cooling rate due to the very nanometer length scales at which complexion transitions occur. Therefore, we expect that the section of the sample which is quenched the fastest and is in direct contact with the Al heat sink would be closest to the high temperature microstructure, and will be henceforth referred to as the *fast quench* surface. The center of the sample is referred to as the *medium quenched* region, while the top of the sample farthest from the heat sink is referred to as the *slow quenched* region.

Transmission electron microscopy (TEM) specimens were taken from the Cu-Zr and Cu-Zr-Hf samples at the fast, medium, and slow quenched sections of the sample using the focused ion beam (FIB) lift-out method with a Tescan GAIA3 SEM/FIB. A final 5 kV polish was used on all samples to remove any excess ion beam damage from earlier preparation steps. Microstructural characterization, including bright field TEM (BF TEM), selected area electron diffraction (SAED), high resolution TEM (HRTEM) of the grain boundary structure, measurement of AIF thickness, and high-angle annular dark field STEM (HAADF) were performed using a JEOL JEM-2800 TEM. The thicknesses of at least 20-40 amorphous complexions from the fast, medium, and slow quenched regions of both the Cu-Zr and Cu-Zr-Hf samples were measured by orienting the grain boundaries in an edge-on condition, which was confirmed by ensuring that there is no variation in the thickness of the complexion when viewed in under-focused and over-focused imaging conditions.

4.3 Results and Discussion

4.3.1 Simulation of Temperature Distribution within the Bulk Samples

To provide insight into the cooling rate variation within the sample, a COMSOL Multiphysics simulation of the cooling process was performed, as shown in Figure 4-1(b). A Cu (for the consideration of heat transfer properties) semi-cylinder with the aforementioned sample dimensions was constructed. To replicate the experimental cooling conditions, a temperature of 77 K is assigned to the bottom surface of the sample, representing the location where the specimen contacts the Al cooling block. The cooling block is much larger than the nanocrystalline pieces and in constant contact with the liquid nitrogen reservoir, so the block is assumed to remain at 77 K during cooling of the specimen. Conductive heat transfer occurs from this bottom surface, while the other sample surfaces are cooled by radiation and convection into the air at room temperature.

Figure 4-1(b) shows the temperature profile within a bulk piece 0.05 s after contact with the cooling block. The blue dot represents the fast quench side of the sample which is directly in contact with the Al block, while the orange and red dots represent the medium (middle) and slow (top) quenched regions of the sample, respectively. It is also important to note that temperature and cooling rate data for the fast and slow quenched regions of the sample, as well as the TEM specimen extraction described later, were obtained at a distance of ~100 μm from the surface of the sample in order to avoid the effects of a thin oxide layer which forms on the surface when the hot piece is exposed to air during transfer from the furnace. The temperature of each of these three regions is plotted as a function of time (*t*) in Figure 4-2(a), with $t = 0$ representing the initial contact with the cooling block.

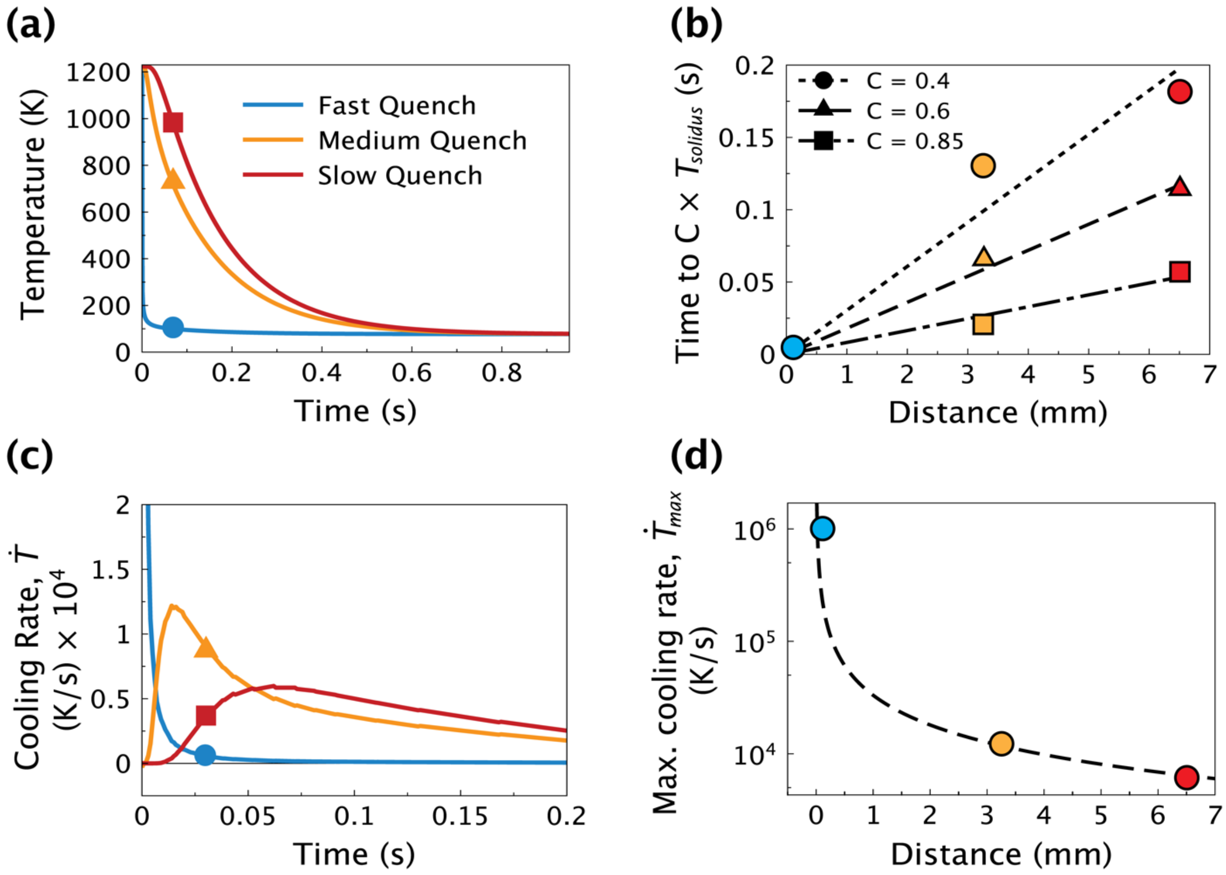

Figure 4-2: (a) Plot of temperature versus time at the fast, medium, and slow quench regions of the bulk samples, as predicted by a simulation of the quenching procedure. (b) Plots of the time for each of the three sample positions to reach a temperature of $0.4T_m$, $0.6T_m$, and $0.85T_m$. $0.85T_m$ represents the highest temperature at which an amorphous-to-ordered complexion transition could potentially occur upon cooling, while $0.4T_m$ represents a possible temperature below which complexion transitions would be restricted due to limited diffusion and atomic rearrangement. (c) Cooling rate as a function of time at the fast, medium, and slow quenched regions of the samples. (d) Maximum cooling rates at the fast, medium, and slow quenched regions as a function of distance from the surface in direct contact with the Al heat sink.

The quenching at different locations can be quantified in a number of ways, with the first being the time required for sample position to reach a given temperature. This would be most useful if specific target temperatures such as the glass transition temperature for the amorphous complexion or the temperature associated with the "nose" (i.e., the temperature where nucleation and growth competition is optimized) of a transition to an ordered complexion from an interfacial

TTT diagram were known. These temperatures are not known currently, although some approximate values can be hypothesized. For example, a prior study by Khalajhedayati and Rupert suggests that the transition to an amorphous complexion for Cu-3Zr occurs somewhere between 750 °C and 850 °C, in the range of roughly 82% to 90% of the solidus temperature for this alloy [71]. This is in agreement with Luo et al. [134], who have predicted that grain boundary premelting transitions can begin at temperatures as low as 60-85% of the melting temperature. The upper bound of relevant temperatures would therefore be roughly $0.85T_m$ or 785 °C, the highest temperature below which transitions from an amorphous to an ordered complexion would be expected. The lower bound of this range at $0.6T_m$ or 474 °C represents a possible intermediate temperature to consider, as ordered complexions would be preferred while there is still enough thermal energy for rapid diffusion. A possible lower bound would be where diffusion has slowed significantly, which we take as a temperature of $0.4T_m$, or 225 °C, to match the description of rough bound for a "high temperature" when considering other diffusion-based processes such as creep. These temperatures are not meant to be exact values of great importance, but rather to give a rough sense of the important cooling times. Figure 4-2(b) displays the time required for each location to reach each of these three temperatures. The entire sample cools to a temperature of $0.4T_m$ in less than 0.2 s (reminding the reader that this is not accounting for the short amount of time required to quickly transfer the sample from the furnace to the heat sink).

To gain a better understanding of the quenching at each position, the derivative of the cooling curves or the cooling rate, $\dot{T}$, is shown in Figure 4-2(c), while Figure 4-2(d) shows the maximum cooling rate, $\dot{T}_{max}$, for each sample position. We note that the maximum cooling rate for the fast quench location, shown in blue, is much faster than the other two locations, so this peak is out of the y-axis range in Figure 4-2(c). The results reported in Figure 4-2 confirm that the chosen method of controlled quenching achieves a variety of cooling rates at different sample positions, with $\dot{T}_{max}\boxed{\dot{T}_{max}}$ ranging from ~5900 K/s in the slow quench region to 1.03×10^6 K/s in the fast quench region, spanning multiple orders of magnitude. These cooling rates are on par with or exceed those necessary to form bulk metallic glasses in Cu-Zr and Cu-Hf alloys via processing methods such as melt spinning [135-137]. The significant differences in the cooling rates between sample positions allows for the investigation of the impact of quench rate for the retention of AIFs in both the binary and ternary nanocrystalline alloys.

4.3.2 Characterization of Microstructure and Grain Boundary Structure

Detailed characterization of the microstructure at each of the fast, medium, and slow quench positions for the Cu-Zr and Cu-Zr-Hf samples was next performed in order to probe grain size and grain boundary segregation state. HAADF micrographs of representative microstructures of each of the three investigated sample positions in the binary and ternary samples are shown in Figure 4-3(a). The average grain sizes for each sample location, plotted in Figure 4-3(b), are nearly identical, confirming that the variations in cooling/quenching rate do not induce a gradient in grain size or provoke abnormal grain growth. The average grain sizes were found to be between 67 nm and 73 nm in all cases, showing very small variations within the expected noise in the measurement. The similar grain sizes mean that the volume of grain boundary material is also nearly the same for all samples investigated in this study. In Figure 4-3(a), the presence of second phase precipitates throughout the microstructures of both the Cu-Zr and Cu-Zr-Hf samples is found to be minimal, and therefore should not significantly influence the amount of dopant that is available to segregate to grain boundaries. More detailed characterization of the limited ZrC and HfC second phases that form in Cu-Zr and Cu-Zr-Hf microstructures can be found in our prior study of these alloys [76]. Bright contrast at the grain boundaries is observed for both samples and at all positions, indicating locations where Zr and/or Hf dopant atoms have segregated during either the powder consolidation and/or annealing steps. Heavily doped boundaries are likely sites for the formation of amorphous complexions, as increased local composition above a critical threshold value can lead to the transition to an amorphous structure at high temperatures [138]. The fact that the samples have the same global dopant concentration, grain size, grain boundary volume fraction, segregation state, and carbide content allows for a direct comparison of complexion populations between samples, with only the complexity of the grain boundary chemistry (binary versus ternary) and quench rate (fast, medium, or slow) changing.

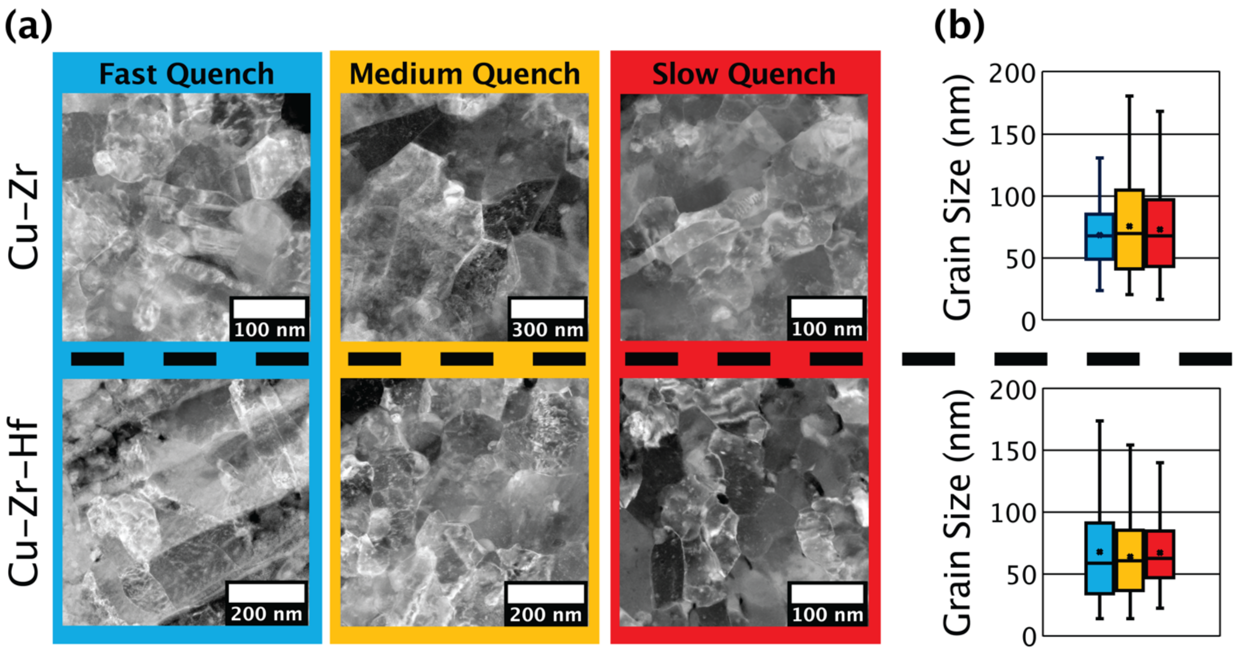

Figure 4-3: (a) HAADF images of the microstructures in the fast, medium, and slow quenched regions for the Cu-Zr and Cu-Zr-Hf samples. (b) Box and whisker plots of grain sizes from the three regions in both samples show nearly identical grain size distributions in all regions. Dots within the box represent the mean grain size for each region, while horizontal lines represent the median grain size.

HRTEM of the grain boundaries was next performed. We focused on identifying interfaces which had maintained the amorphous complexion structure and then the subsequent measurement of the thicknesses of these structures. Micrographs of representative amorphous complexions found in the Cu-Zr alloy are shown in Figure 4-4. Very thick amorphous complexions are found regardless of the maximum cooling rate at each sample position. However, we emphasize that there are boundary-to-boundary variations in amorphous complexion thickness, which has been shown previously to be related to variations in dopant concentration that depend on boundary character [138]. It is also important to note that not every grain boundary within the microstructure is an amorphous complexion, as some doped but ordered interfaces are still found. We observe here that amorphous complexions are more likely to form at grain boundaries where high levels of dopant segregation are observed, such as those of high contrast noted in Figure 4-3(a), a finding that is consistent with prior work on these alloys [35, 36].

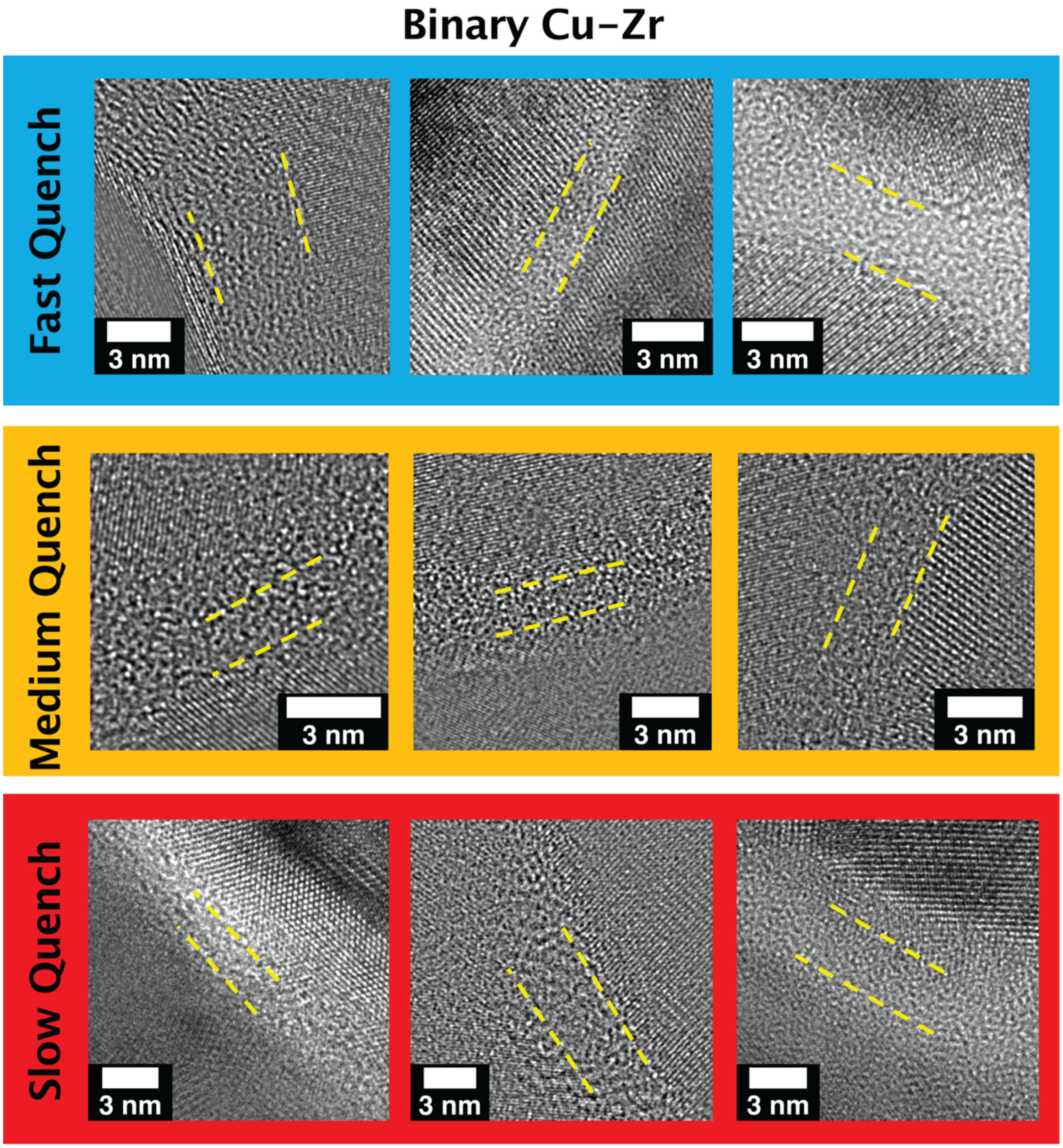

Figure 4-4: HRTEM micrographs of amorphous complexions found in the fast, medium, and slow quench regions of the Cu-Zr sample. Yellow dotted lines denote the edges of the amorphous complexion between abutting grains.

Figure 4-5 shows a micrograph of an interesting grain found in the fast quench region of the Cu-Zr sample which had the majority of its boundaries in an amorphous state. The overlay of red and blue dashed lines on the micrograph represent ordered and amorphous grain boundaries, respectively. This grain demonstrates the efficacy of rapid quenching for freezing in many thick amorphous complexions within the microstructure. It is important to note that measurements of complexion thickness, presented later in the work, are not taken from low magnification images such as the one shown in Figure 4-5. Measurements of amorphous complexion thickness are obtained at very high magnification and exclusively from those boundaries in an edge-on condition, verified by ensuring there is no variation in thickness when viewing the amorphous boundary in under- and over-focused imaging conditions. Additionally, amorphous complexion thickness measurements are taken from the thinnest observed region in order to ensure consistency in the reported measurements.

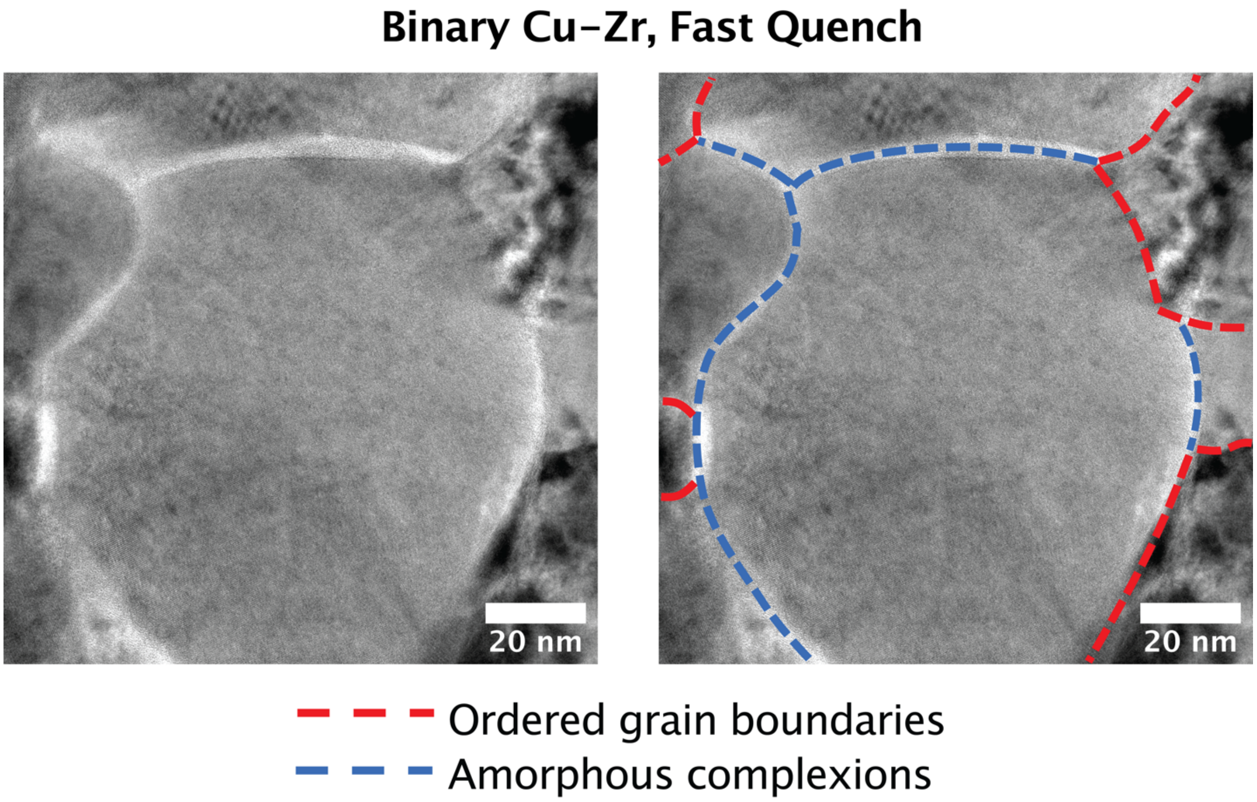

Figure 4-5: TEM micrograph of a grain found in the fast quench region of the Cu-Zr sample that is predominantly surrounded by amorphous grain boundary complexions. Ordered grain boundaries and amorphous complexions are indicated in the micrograph on the right by red and blue dotted lines, respectively.

Representative micrographs of amorphous complexions found in the Cu-Zr-Hf alloy from the fast, medium, and slow quenched regions are shown in Figure 4-6. Again, thick amorphous complexions are found in all locations. The rapid cooling rates during the bulk sample quench against the Al heat sink apparently allow amorphous complexions to be stabilized for both alloy systems. In order to compare the effect of these varying cooling rates on amorphous complexion populations in the two bulk samples, 20-45 amorphous complexions were isolated and the thickness measured in an edge-on condition from the fast, medium, and slow quench regions of the binary and ternary samples. Cumulative distribution functions of amorphous complexion thickness at each of the three positions in the Cu-Zr sample are shown in Figure 4-7(a). These complexion thickness distributions reveal an obvious dependence of the ability to retain thick amorphous complexions on the local cooling rate. The fast quench side of the sample sustains by far the thickest amorphous complexions (average thickness of 2.9 nm, with a number of very thick amorphous films above 4 nm), while the thinnest ones are found on the slow quench side of the sample (average thickness of 1.3 nm).

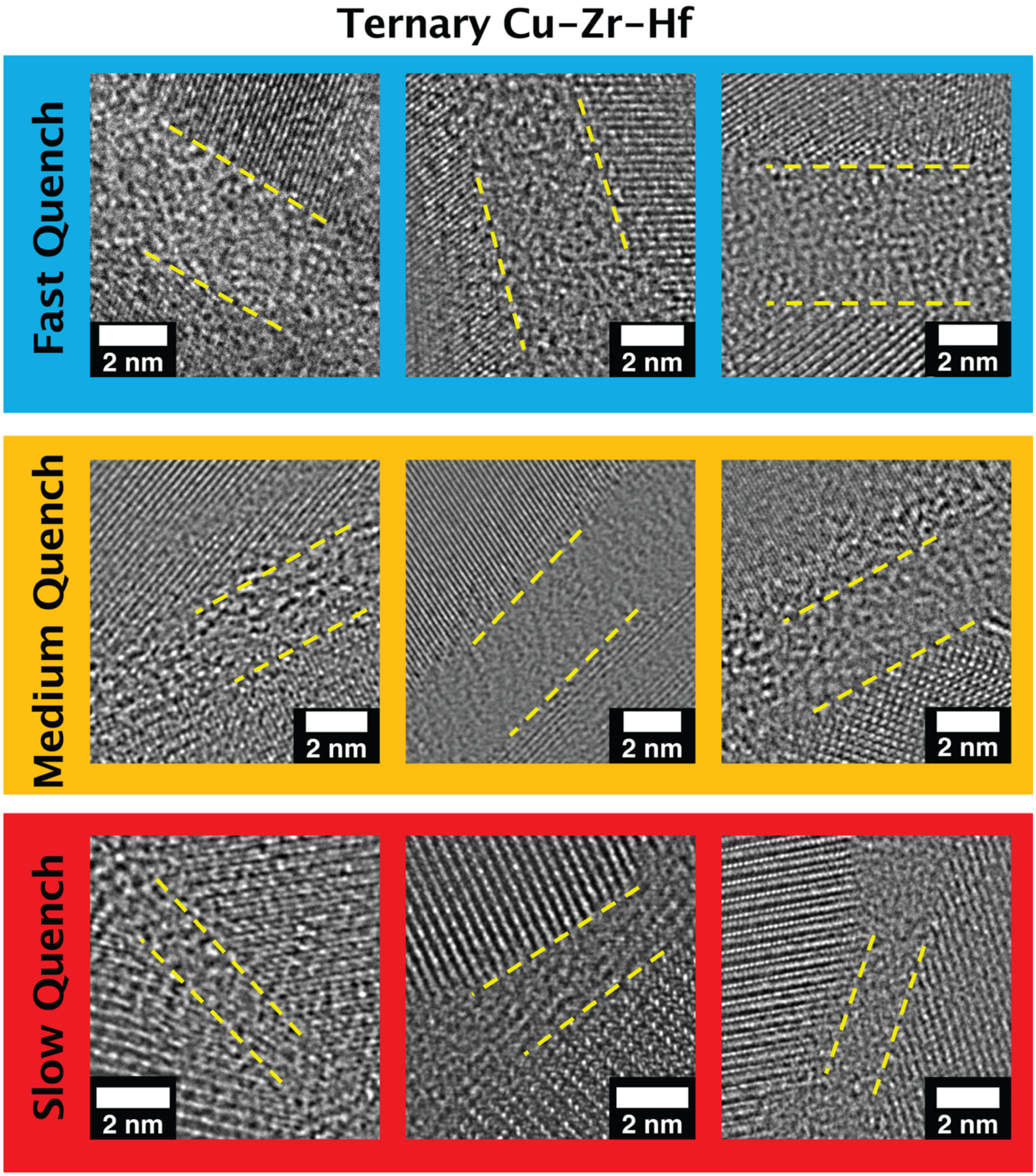

Figure 4-6: HRTEM micrographs of amorphous complexions found in the fast, medium, and slow quench regions of the Cu-Zr-Hf sample.

To put the amorphous complexion thickness populations into perspective, we compare these results with the amorphous complexion thickness results from a prior study where a Cu-4Zr powder sample encapsulated under vacuum in a quartz tube was quenched by dropping into a water bucket from the same annealing temperature [76]. While the sample was quickly put into the quenching medium in [76], there was likely some delay in the reduction of the temperature of the powder particles. The distribution of amorphous complexion thicknesses measured in the quenched powder sample are also plotted in Figure 4-7(a), with an average thickness of 1.6 nm. The rapid quenching method used in this study allows for a larger number of thick amorphous complexions to be sustained in the Cu-3Zr microstructure, with roughly double the average complexion thickness compared to the Cu-4Zr powders quenched in a quartz vial. While amorphous complexions were achieved in all specimens through the careful selection of dopant elements which segregate to grain boundaries, the results of this study highlight the importance of processing conditions, in particular cooling rate, to capture thick amorphous complexions by preventing transitions to thinner amorphous films or ordered grain boundary phases altogether.

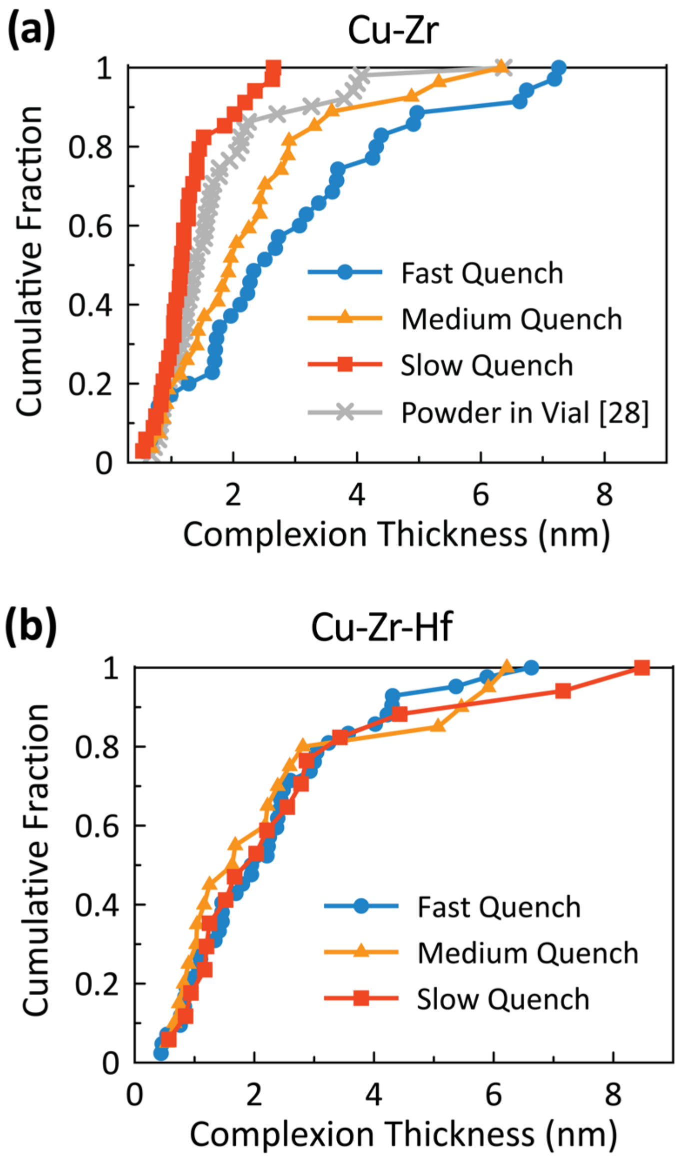

Figure 4-7: (a) Cumulative distribution function of complexion thickness populations in the Cu-Zr sample at the fast, medium, and slow quench regions, as well as from a Cu-4Zr powder sample quenched in a quartz tube investigated in Ref. [76]. (b) Cumulative distribution function of complexion thickness populations in the Cu-Zr-Hf sample at the fast, medium, and slow quench regions, indicating that the average complexion thicknesses in this sample are independent of cooling rate.

In contrast, the complexion thickness distributions for the Cu-Zr-Hf alloy shown in Figure 4-7(b) show no dependence on the cooling rate. This resistance to transforming to ordered grain boundaries under identical cooling profiles can be attributed to the resulting reduction in the energy for the amorphous phase with a more complex chemistry, moving from two elements at the grain boundary to three, which further stabilizes the amorphous grain boundary phases that are able to form [34, 139, 140]. The addition of three or more alloying elements is a widely used method of improving the stability of bulk metallic glasses, whereby increasing the number of constituent elements enables the formation of a highly dense, randomly packed amorphous structure while hindering the nucleation and growth of a crystalline phase due to the increased difficulty of long-range atomic rearrangements [69, 141]; the same materials design concept appears to also improve the stability of amorphous complexions. We also note that the amorphous complexion populations in the Cu-Zr-Hf sample are nearly identical to that of the fast quench region of the Cu-Zr sample. This similarity suggests that these amorphous complexion populations are likely representative of the high temperature state, while the other two populations in the binary alloy represent states where some of the amorphous boundaries have either become thinner or transformed back into ordered grain boundaries. While our prior study reported that thicker amorphous intergranular films were found in Cu-Zr-Hf than Cu-Zr due to the more complex grain boundary chemistry [76], the difference observed in that study may have been associated more with the slower cooling rate associated with quenching the powders than the difference in compositional complexity. We hypothesize that the amorphous complexion population in the binary alloy in [76] became thinner more quickly than the ternary alloy during the cooling step, rather than there being a difference in the complexion structure at high temperature.

4.3.3 Time-Temperature-Transformation Diagrams for Amorphous-Ordered Complexion Transitions

The equilibrium structure and thickness of a grain boundary complexion is largely determined by the temperature and grain boundary composition, so it is expected that amorphous complexions will thin or even undergo a transition to the ordered structure as the temperature of the material is reduced. However, analogous to bulk phase transitions, this complexion transition would not happen immediately upon cooling due of the time required for an ordered complexion to nucleate and grow along the boundary. We hypothesize that the addition of Hf to a Cu-Zr alloy adds additional chemical complexity to the grain boundary region, making the transition to an ordered grain boundary more difficult and therefore making the complexion more resistant to transformation. The significant differences in the retained amorphous complexion populations in the Cu-Zr for different cooling rates motivate a more in-depth analysis of the amorphous-to-ordered complexion transformation in these two alloys.

The relative stability of the amorphous complexions formed in Cu-Zr and Cu-Zr-Hf can be understood using a TTT diagram similar to the one shown in Figure 4-8(a). The blue, yellow, and red arrows represent the fast, medium, and slow quench cooling paths, respectively. Conditions that provoke transition to thinner amorphous or ordered grain boundary complexions in the binary Cu-Zr alloy are represented by the shaded green region, while the more stable ternary Cu-Zr-Hf alloy transformation region appears as a shaded purple region. With our hypothesis that the complexion population at the fast quench region of the Cu-Zr sample is representative of the high temperature grain boundary structure, the transformation region is drawn to the right of the fast cooling curve. This indicates that this region is cooled at a rate which is greater than the critical cooling rate (R_c) necessary to retain the population of thick, premelted boundaries formed during annealing. However, at regions quenched slower than R_c, represented by the slow and medium quench curves, amorphous complexions undergo a complexion transition, resulting in thinner complexion populations. In contrast, the nose of the curve representing the transition to thinner amorphous or ordered complexions in the ternary Cu-Zr-Hf alloy is shifted to the right on Figure 4-8(a), indicating that the premelted grain boundary containing three elements is more stable against crystallization for a longer period of time as compared to the binary alloy. Therefore, R_c is reduced and the cooling rates of the fast, medium, and slow quenched cooling rates are sufficient to avoid the complexion transition for Cu-Zr-Hf, as evidenced by the identical amorphous grain boundary thickness distributions that are observed.

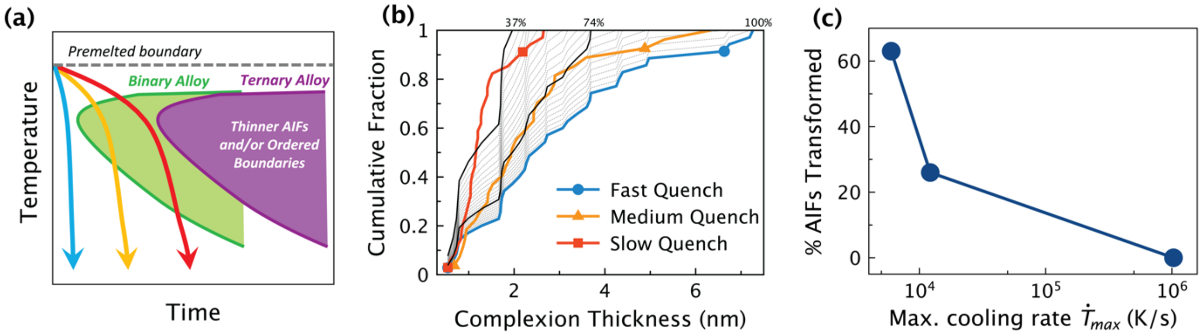

Figure 4-8: (a) Schematic of a time-temperature-transformation (TTT) diagram for the binary Cu-Zr and ternary Cu-Zr-Hf alloys. Blue, orange, and red cooling paths correspond to the fast, medium, and slow quench regions, respectively. The complexion transition region for the ternary alloy is shifted to the right, indicating that AIFs formed in this alloy are more stable against transitions to thinner amorphous films or ordered grain boundaries than those in the binary alloy. (b) Cumulative distribution function of complexion thicknesses in Cu-Zr, where the dashed lines represent subsets of the data from the fast quench sample. The distribution subsets denoted by solid black lines aligned with measurements of the medium and slow quench curves and represent the bottom 74% and 37% of the fast quench data, indicating that 26% and 63% of the amorphous boundaries in these regions have transformed, respectively. (c) Plot of the percentage of AIFs which have transformed to thinner films or ordered boundaries as a function of local maximum cooling rate.

We note that the schematic view in Figure 4-8(a) does not distinguish between the different complexion transitions that can result during cooling. An amorphous complexion of a given thickness at the annealing temperature would want to take on a smaller thickness at a lower temperature, but this transition would take time to occur. Therefore, a more complete TTT diagram would have many such transition regions defined, one each for each amorphous complexion thickness and another for the final reversion to an ordered structure. Such a representation would be unwieldy but also only hold exactly true for one given boundary. Another interface with a different segregation composition and a different crystallography would have these transition regions positioned at slightly different locations [35, 138, 142]. Since we are looking at the behavior of a larger population of amorphous interfacial films, we simplify this view to have all transitions to either thinner amorphous films or to an ordered structure outlined by a single transition region for each alloy. A more complete description of the connection between the thickness of a single amorphous complexion and temperature is available in a number of prior studies, expressed as grain boundary phase diagrams [55, 85, 143].

The extent to which amorphous complexions in the medium and slow quench regions of the Cu-Zr samples have transformed to thinner or ordered boundaries during cooling can be estimated by comparing the amorphous complexion thickness distributions between the different quench rates. Because the complexion population in the fast quench region of the binary alloy matches the invariant amorphous complexion populations found in the ternary alloy, we make the assumption that it is representative of the equilibrium complexion thickness population at high temperatures (i.e., no thick amorphous-to-thin amorphous or amorphous-to-ordered complexion transitions have occurred). To represent the transition of a fraction of the original amorphous complexions, the thickest measurements are removed one by one from the fast quench population and the remaining populations are replotted as cumulative distribution functions in Figure 4-8(b). In this figure, the dashed grey lines represent subsets of the fast quench complexion thickness data, where the bottom X% of the high temperature or fast quenched distribution is plotted, meaning that 100-X% of the amorphous boundaries have become thinner, either remaining amorphous but with reduced thickness or transforming to an ordered structure. Using these curves, we can estimate the fraction of complexions in the medium and slow quenched regions which have transformed. The medium quench region is best fit by X = 74%, implying that 26% of the original amorphous complexions have transformed. Similarly, the slow quench region is best fit by X = 37%, implying that 63% of the original complexions have transformed. We note that this analysis makes no specific claims about the behavior of any given boundary or implies any specific transition, other than the general shift of the statistical thickness distribution to the left as amorphous complexion thickness in general decreases. Figure 4-8(c) reports the fraction of amorphous complexions in the Cu-Zr alloy that have transformed to either a thinner amorphous or ordered complexion plotted as a function of the local maximum cooling rate, showing that the number of amorphous complexions which transform increases as the cooling rate decreases.

A quantitative comparison of R_c for the transformation of thick, disordered to thinner or complexions boundaries in the Cu-Zr and Cu-Zr-Hf alloys can be demonstrated with TTT curves analogous to those developed for bulk metallic glasses. In order to construct these curves, we again must that the population of complexions in the fast quench regions are representative of the high temperature grain boundary structure. In addition, it is assumed that this region has cooled at a rate only just sufficient to avoid the complexion transition, and therefore the cooling path of the fast quench region narrowly misses the nose of the TTT curve for the binary alloy. TTT curves constructed for both the Cu-Zr and Cu-Zr-Hf alloy are shown in Figure 4-9. The temperature corresponding to the nose of the crystallization TTT curve for bulk metallic glasses has been previously shown to be roughly the average of the glass transition temperature and liquidus temperature, T_l, for the alloy [144, 145], indicated by the $0.5(T_g+T_l)$ line. The T_l of a bulk metallic glass is analogous to the solidus temperature of the alloys in this study ($T_{solidus}$). T_g is most closely analogous to the temperature at which ordered complexions transform to amorphous complexions (T_{AIF}), which is taken to be $0.85T_{solidus}$ to account for the upper temperature limit at which an amorphous-to-crystalline complexion transition can occur. [134]. The nose of the two TTT curves are placed at a temperature halfway between these limits, at 879 °C. The nose of the binary alloy transition region is positioned to be tangential to the fast quench cooling path, suggesting that while no complexion transition occurred, any reduction in quench rate would have led to a decrease in amorphous complexion thickness. This is an inherently conservative assumption. Although the cooling rates in our experiment are not constant, estimated constant cooling rate R_c curve is plotted alongside actual cooling curve of the fast quench region to provide an estimate that a constant cooling rate of $\sim 6\times10^6$ K/s would be needed to avoid the complexion transition. The medium and slow quench regions of the bulk binary sample cool at considerably slower rates and traverse through the transformation region in the TTT curve, resulting in reconfiguration of the AIFs in these regions to either thinner AIFs or ordered complexions.

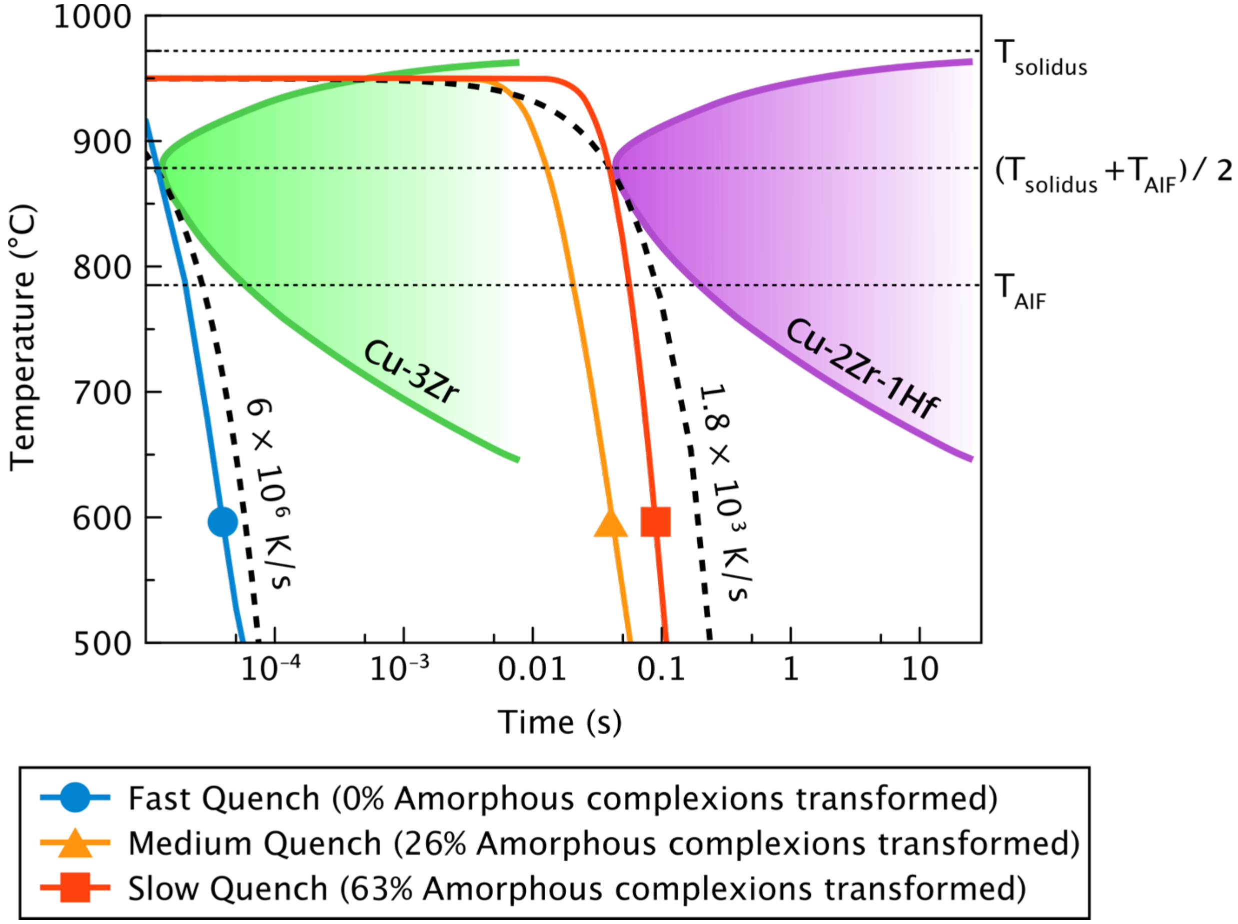

Figure 4-9: TTT curves for Cu-Zr and Cu-Zr-Hf, with plotted cooling paths for the fast, medium, and slow quench regions obtained using COMSOL. T_{nose} *for both transition regions is set as the average of the solidus temperature,* $T_{solidus}$*, and the highest temperature at which amorphous complexions begin to form upon heating,* T_{AIF}*. Estimates of the critical cooling rates necessary to avoid complexion transitions for the binary and ternary alloys are found to be* $6{\times}10^6$ *K/s and* $1.8{\times}10^3$ *K/s, respectively, corresponding to a critical cooling rate for the ternary alloy that is roughly 3000 times slower than that for the binary alloy.*

A similar TTT curve for the Cu-Zr-Hf alloy is drawn further to the right on this figure, indicating the observed resistance to the complexion transition. The fact that the quenching curves do not pass through the complexion transition region on the schematic illustration is justified by the complexion thickness distributions measured in the ternary alloy and the observation that these distributions appear to be insensitive to cooling rate within the boundaries probed here. To again make a conservative estimate, we again assume that the nose of the transition region would have begun at a time immediately after the time taken for the slow quench region of the sample to reach T_{nose}. Again overlaying a constant cooling curve, we calculate that the R_c of the ternary alloy with be ~1.8×10^3 K/s. Comparison of the estimated R_c values therefore suggests that the ternary alloy can be cooled over 3000 times slower and still retain the complexion population that is representative of the high temperature equilibrium structure, demonstrating a significant improvement in the stability of thick amorphous complexions with increasing chemical complexity. It is important to note that the magnitude of reduction in R_c is not strongly dependent on any of the assumptions made about the location of T_{nose} for these TTT curves. For example, if a much lower T_{nose} value of 225 °C (corresponding to $0.4T_{solidus}$ below which diffusion would be very slow) is alternatively chosen, R_c in the Cu-Zr-Hf sample is still roughly three orders of magnitude lower than R_c for the Cu-Zr sample.

The reduction of R_c by a significant factor helps explains the observed difference in amorphous film thickness between Cu-Zr and Cu-Zr-Hf alloys in our prior investigation on powder specimens in Ref. [76]. In this prior work, fewer complexion transitions occurred, leading to an amorphous complexion population that was thicker and closer to the high temperature distribution. In addition, the complexions found in the fast quench region of the binary sample and throughout the entire ternary sample are the thickest stable amorphous intergranular films reported to date. With an average thickness of 2.9 nm, the amorphous complexions are ~40% thicker than the complexion population observed in the ternary sample in Ref. [76]. With an eye toward future work and more rigorous confirmation of the high temperature structure, we expect that the most accurate evidence would come from in situ TEM heating experiments to directly observe equilibrium amorphous complexion thicknesses at high temperature.

The choice of elements with a positive enthalpy of mixing, negative enthalpy of segregation, a large atomic size mismatch, and the use of multiple constituent elements are all guidelines suggested to maximize the glass-forming ability (GFA) of metallic glasses. A variety of parameters, including but not limited to the inverse of R_c, are used to quantify the GFA of bulk metallic glasses. Improvements to GFA have been associated with the addition or substitution of dopant elements in these materials, analogous to the improvements in amorphous complexion stability reported in this study. For example, Yu et al. [146] demonstrated an improvement in GFA of a binary Cu-Zr alloy upon addition of a third and fourth element, evidenced by both a dramatic decrease in R_c as well as an increase in the critical casting diameter. The selection of elements with a positive enthalpy of segregation, negative enthalpy of mixing, and multiple constituent elements has also been shown to promote the formation of amorphous complexions at grain boundaries in prior studies [67, 76]. However, the impact of the implementation of each of these criteria has not been proven to improve the stability of the amorphous complexions or shown to resist transition back to the ordered structure prior to this study. While the present results demonstrate a significant reduction in R_c is achieved with the addition of a second dopant element, to achieve a ternary grain boundary composition, we note that this improved stability is achieved despite the fact that Zr and Hf have very similar atomic radii (Zr: 160 pm, Hf: 156 pm), with an atomic radius difference of 2.5%. This is consistent with several studies of bulk metallic glasses that have also shown that the replacement of a fraction of Zr with an appropriate amount of Hf can lead to a significant improvement in GFA [96, 147, 148]. One such example is a study of an Fe-based bulk metallic glass, where the GFA of the base alloy containing 8 at.% Zr was improved upon substituting 3 at.% Hf for 3 at.% Zr, with a reduction in glass transition temperature used to show the effect [148]. The results of this study confirm that increasing the compositional complexity of the grain boundary region helps to prevent the local atomic rearrangements necessary for the amorphous complexion to crystallize into an order boundary structure.

The ability to sustain thick amorphous complexions in a bulk material through the reduction of R_c also holds significant important from a materials processing perspective. While the presence of amorphous complexions has been shown to improve the fracture toughness, strength, and ductility of nanocrystalline materials, these features must be sustained within the material's microstructure in order to impart these effects [18, 70, 74]. A simple practical observation from this work is that bulk samples were produced that contained thick amorphous complexions with a stable thickness distribution throughout the specimen, opening the doorway for larger nanocrystalline specimens with improved properties.

4.4 Conclusions

In this study, amorphous grain boundary complexions were investigated in binary and ternary Cu-rich alloys with an eye toward evaluating their relative stability against transformation while cooling from a high temperature. Bulk Cu-3Zr and Cu-2Zr-1Hf alloys were created by sintering mechanically alloyed powders, and were then annealed and quenched in a special manner in order to induce a cooling rate gradient. The fast, medium, and slow quench regions of both bulk samples were inspected using HRTEM to characterize and tabulate the thicknesses of the amorphous complexions. The following conclusions can be drawn:

- Amorphous complexions formed at all positions throughout both the binary and ternary bulk samples. The quenching method utilized in this study, in which bulk samples are placed on an Al heat sink immersed in liquid nitrogen, retained much thicker amorphous complexions compared to previous studies where powder samples of similar compositions were quenched into water baths inside of quartz vials. The increased amorphous film thickness in this study is attributed to achieving cooling rates greater than the critical cooling rate necessary to avoid amorphous complexions transforming back to thinner films or ordered boundaries.

- Amorphous complexions in the Cu-Zr-Hf sample were significantly more stable against complexion transitions to thinner or ordered grain boundaries compared to the AIFs in Cu-Zr. On average, the complexions in the binary alloy were thinner at slower cooling rates, while the complexion thickness population for the ternary alloy was found to be invariant with cooling rate. The addition of a third element serves to stabilize the amorphous grain boundary complexion, therefore reducing the critical cooling rate necessary to prevent the amorphous-to-ordered complexion transformation. The value of the critical cooling rate was found to be at least three orders of magnitude slower in the ternary alloy compared to the binary alloy.

The results of this study demonstrate the enhanced stability of thick amorphous complexions with complex grain boundary chemistries. This finding makes nanocrystalline alloys with amorphous complexions accessible by a greater range of conditions and enables applications that might benefit from the unique properties of amorphous complexions, such as enhanced thermal stability, fracture toughness, and resistance to radiation damage. These findings demonstrate that complexion TTT diagrams are valuable tools for understanding complexion transitions and the stability of complexion networks. The results of this study motivate further experimental and computational work to construct TTT diagrams for a variety of complexion transitions, as well as the investigation of the stability of amorphous complexions which form in more compositionally complex alloys.

5 Conclusions

Nanocrystalline metals are highly desirable materials to use in a variety of applications in which high strength, radiation tolerance, and resistance to corrosion. The enhancement of these properties with the refinement of grain size is due to the associated increase in interfacial material. However, the large amount of grain boundary material limits the use of nanocrystalline metals in suitable applications for two main reasons, namely, the thermal instability of the microstructure due to the high amount of grain boundary excess energy, and also the lack of ductility. The recent classification and characterization of grain boundary complexions has opened the door to manipulating the grain boundary structure and chemistry as a means of tuning bulk material properties. In the context of nanocrystalline metals, amorphous complexions have been previously shown to impart significant improvements to thermal stability, strength, radiation tolerance, and ductility, with these effects being further enhanced with increasing complexion thickness.

The goal of this thesis is to improve the utility of nanocrystalline metals through the introduction of thick amorphous complexions at grain boundaries, in order to maximize their microstructural stability and beneficial properties. The manipulation of grain boundary chemistry was hypothesized to both further reduce the grain boundary energy, as well as increase the structural and chemical disorder at grain boundaries to frustrate crystallization and lead to the formation and retention of thick amorphous complexions. Additionally, the formation of compositionally complex complexions was hypothesized to increase the stability of the complexion itself, allowing for easier formation and making them more resistant to transformation upon cooling to lower temperatures where they are no longer the stable grain boundary phase. The main conclusions of this thesis are reviewed below.

In Chapter 2, the effects of adding an additional dopant element to a previously studied binary Cu-Zr alloy known to form amorphous complexions is investigated. Hf was chosen as a dopant due to its similarity in reactivity and atomic size to Zr, allowing for the direct investigation of increasing only the chemical complexity on both the thermal stability and amorphous complexion formation behavior. Ternary Cu-Zr-Hf alloys in varying compositions were formed via mechanical alloying and subsequent annealing at 950 °C, or 98% of the solidus temperature, to study the thermal stability behavior and allow for the formation of grain boundary complexions. Binary Cu-Zr and Cu-Hf alloys were formed in the same manner in order to compare and contrast the dopant distribution in the various alloys. The Cu-Zr and Cu-Zr-Hf alloys were found to be highly resistant to grain growth, retaining nanocrystalline microstructures even after two weeks of annealing at high temperature. However, the Cu-Hf alloys were found to be less thermally unstable with increasing Hf additions, due to the wicking away of atoms available to segregate to Cu grain boundaries by HfC phase which formed during mechanical alloying. We find that the ternary Cu-Zr-Hf alloys form thicker amorphous complexions than both the binary Cu-Zr and Cu-Hf alloys with nearly identical global dopant compositions, due to the co-segregation of Zr and Hf atoms to grain boundaries. This demonstrates the potential for utilizing grain boundary composition as a means to improve the thickness of amorphous complexions.

In Chapter 3, the ideas explored in Chapter 2 are extended to investigate complexion formation in quinary alloys. Two additional dopant elements are added to a base Cu-Zr-Hf alloy, to study whether the further complication of grain boundary chemistry would lead to the formation of thicker amorphous complexions. Cu-Zr-Hf-Mo-W, Cu-Zr-Hf-Mo-Nb, and Cu-Zr-Hf-Nb-Ti alloys were formed via mechanical alloying, and subject to a 500 °C anneal for 5 hours to encourage segregation of dopant elements, followed by a high temperature anneal at 950 °C for 5 minutes, 1 hour, and 1 week to allow for the transformation of grain boundaries to an amorphous structure and also probe the thermal stability of each alloy. The Cu-Zr-Hf-Mo-W and Cu-Zr-Hf-Mo-Nb alloys exhibited the lowest thermal stability, associated with the high volume fraction of second phases which formed in these alloys. In contrast, the Cu-Zr-Hf-Nb-Ti alloy which formed the least amount of second phases exhibited the highest thermal stability, retaining a grain size of 63 nm after a week of annealing at >95% of the melting temperature. The Cu-Zr-Hf-Nb-Ti alloy annealed for 5 minutes at 950 °C demonstrated inhomogeneous segregation of Zr, Nb, and Ti atoms to grain boundaries, allowing for the formation of high-entropy grain boundary compositions. However, unlike the previously studied Cu-Zr-Hf alloy, no Hf segregation to grain boundaries was found in this alloy. The grain boundary structure of this alloy was studied, and it was found that the amorphous complexion thickness was found to be 32% thicker than those measured in the Cu-Zr-Hf sample, and 41% thicker than those in the Cu-Zr sample studied in the previous chapter. The results presented in this chapter serve to further solidify the correlation between the chemical complexity at grain boundaries and amorphous complexion thickness. However, these results also highlight the complications associated with proper dopant selection when forming an alloy capable of forming amorphous complexions, as the interactions between dopant atoms themselves can influence their segregation behavior, leading to enhanced enrichment or depletion of particular dopant elements which was not previously observed in binary analogs.

In Chapter 4, the stability of the amorphous complexions themselves was studied as a function of chemical complexity. Bulk Cu-Zr and Cu-Zr-Hf alloys were formed and exposed to a gradient cooling rate, in order to investigate the sensitivity of the amorphous complexions against transformation to thinner or ordered grain boundaries when exposed to different cooling rates. The average thickness of amorphous complexions exposed to varying local cooling rates was used as a metric to probe the grain boundary phase stability. It is found that the thickness of complexions found in Cu-Zr alloys is found to be dependent on the local maximum cooling rate. In contrast, the thicknesses of complexions found in Cu-Zr-Hf alloys were found to be invariant with cooling rate. This demonstrates that the increased chemical complexity at grain boundaries increases the stability of the amorphous complexion against transformation to thinner or ordered grain boundaries, allowing for the use of lower cooling rates to retain the equilibrium thickness at high temperatures. Using this data in combination with COMSOL Multiphysics simulations of the bulk sample quench, time-temperature-transformation diagrams are constructed for the complexion transformations in the binary and ternary alloys. It is found that the addition of a second dopant element reduces the critical cooling rate necessary to retain thick amorphous complexions by at least three orders of magnitude.

In conclusion, the results presented in this thesis highlight the significant effects of careful alloy selection on the formation of thick, amorphous complexions which are highly stable against transformation. The presence of amorphous complexions simultaneously addresses the issues of limited thermal stability and ductility in nanocrystalline metals, and the increased stability of this grain boundary phase in multicomponent alloys increases the potential for the widespread utility of nanocrystalline metals in a wide variety of suitable applications.

6 Future Work

The results presented in this thesis have highlighted the importance of grain boundary chemistry and its influence on grain boundary structure, which in turn significantly effects the properties of the material on the bulk scale. However, there are several areas of research which are left unexplored.

6.1 Materials selection criteria for the formation of amorphous complexions in multicomponent alloys.

As demonstrated by the results presented in this thesis, the complication of alloy chemistry and interactions between multiple dopant elements can serve to enhance segregation behavior or cause the depletion of a particular element at grain boundaries. Computational studies of the segregation of dopants in multicomponent alloys would allow for a more systematic investigation of the formation of amorphous complexions in these materials, and would also allow us to probe the effects of varying the atomic size mismatch and heat of mixing with other dopants as opposed to only the atoms in the bulk phase.

6.2 High-resolution characterization of grain boundary complexion chemistry.

The use of high-resolution STEM imaging, EDS, and EELS techniques would allow for a more detailed view of the segregation of dopant elements to grain boundaries, and the repulsive or attractive interactions between these dopants which would lead to grain boundary enrichment or depletion. It would also allow for a quantitative idea of the exact dopant compositions necessary to induce a transition to an amorphous grain boundary, as well as the distribution of dopant elements within the complexion itself. Detailed characterization of dopant distribution would also allow for observations of gradients of short-range order within an amorphous complexion, which has been previously demonstrated both experimentally and computationally [149-151]. The influence of temperature and grain boundary composition on regions of short-range order within high-entropy complexions can be explored.

6.3 Observation of complexion transitions.

In Chapter 2 of this thesis, various estimates of the temperatures at which grain boundaries experienced a transition from ordered to amorphous were made, based largely off of ex-situ observations of alloys annealed and quenched at a variety of temperatures. In-situ heating experiments of alloys would allow for the direct visualization of a complexion transition at a particular grain boundary with a known dopant concentration and misorientation, allowing for the determination of an exact temperature at which these transitions are expected to occur. Such information would be invaluable in verifying the accuracy of complexion phase diagrams which are currently being designed for a variety of alloy systems.

6.4 Complexion formation in other crystal structures.

The results presented in this thesis demonstrate the formation of thick amorphous complexions in Cu-based alloys. However, it is of interest to extend this application to non-FCC crystal systems. In particular, the formation of thick amorphous complexions in multicomponent Fe-based alloys would have significant implications on the use of these materials in structural applications.

7 References

[1] K.S. Kumar, H. Van Swygenhoven, S. Suresh, Mechanical behavior of nanocrystalline metals and alloys, Acta Materialia 51(19) (2003) 5743-5774.
[2] D.A. Konstantinidis, E.C. Aifantis, On the "Anomalous" hardness of nanocrystalline materials, Nanostructured Materials 10(7) (1998) 1111-1118.
[3] X.Y. Zhang, M.H. Shi, C. Li, N.F. Liu, Y.M. Wei, The influence of grain size on the corrosion resistance of nanocrystalline zirconium metal, Materials Science and Engineering: A 448(1) (2007) 259-263.
[4] N. Nita, R. Schaeublin, M. Victoria, Impact of irradiation on the microstructure of nanocrystalline materials, Journal of Nuclear Materials 329-333 (2004) 953-957.
[5] G. Palumbo, S.J. Thorpe, K.T. Aust, On the Contribution of Triple Junctions to the Structure and Properties of Nanocrystalline Materials, Scripta Metallurgica Et Materialia 24(7) (1990) 1347-1350.
[6] E.O. Hall, The Deformation and Ageing of Mild Steel: III Discussion of Results, Proceedings of the Physical Society. Section B 64(9) (1951) 747-753.
[7] N.J. Petch, The Cleavage Strength of Polycrystals, Journal of the Iron and Steel Institute 174 (1953) 25-28.
[8] Z.C. Cordero, B.E. Knight, C.A. Schuh, Six decades of the Hall–Petch effect – a survey of grain-size strengthening studies on pure metals, International Materials Reviews 61(8) (2016) 495-512.
[9] D. Tabor, The Hardness of Metals, Clarendon Press, Oxford, 1951.
[10] M.A. Meyers, A. Mishra, D.J. Benson, Mechanical properties of nanocrystalline materials, Progress in Materials Science 51(4) (2006) 427-556.
[11] H.V. Atkinson, Overview no. 65: Theories of normal grain growth in pure single phase systems, Acta Metallurgica 36(3) (1988) 469-491.
[12] S. Simões, R. Calinas, M.T. Vieira, M.F. Vieira, P.J. Ferreira, In situ TEM study of grain growth in nanocrystalline copper thin films, Nanotechnology 21(14) (2010) 145701.
[13] H. Natter, M. Schmelzer, M.S. Löffler, C.E. Krill, A. Fitch, R. Hempelmann, Grain-Growth Kinetics of Nanocrystalline Iron Studied In Situ by Synchrotron Real-Time X-ray Diffraction, The Journal of Physical Chemistry B 104(11) (2000) 2467-2476.
[14] M. Ames, J. Markmann, R. Karos, A. Michels, A. Tschöpe, R. Birringer, Unraveling the nature of room temperature grain growth in nanocrystalline materials, Acta Materialia 56(16) (2008) 4255-4266.
[15] V.Y. Gertsman, R. Birringer, On the room-temperature grain growth in nanocrystalline copper, Scripta Metallurgica et Materialia 30(5) (1994) 577-581.
[16] J.A. Haber, W.E. Buhro, Kinetic Instability of Nanocrystalline Aluminum Prepared by Chemical Synthesis; Facile Room-Temperature Grain Growth, Journal of the American Chemical Society 120(42) (1998) 10847-10855.
[17] I.-J. Bae, S. Baik, Abnormal Grain Growth of Alumina, Journal of the American Ceramic Society 80(5) (2005) 1149-1156.
[18] Z. Pan, T.J. Rupert, Amorphous intergranular films as toughening structural features, Acta Materialia 89(Supplement C) (2015) 205-214.
[19] O.K. Donaldson, K. Hattar, T. Kaub, G.B. Thompson, J.R. Trelewicz, Solute stabilization of nanocrystalline tungsten against abnormal grain growth, Journal of Materials Research (2017) 1-13.

[20] J. Weissmüller, Alloy effects in nanostructures, Nanostructured Materials 3(1) (1993) 261-272.
[21] M.N. Polyakov, T. Chookajorn, M. Mecklenburg, C.A. Schuh, A.M. Hodge, Sputtered Hf–Ti nanostructures: A segregation and high-temperature stability study, Acta Materialia 108 (2016) 8-16.
[22] Y.Z. Chen, A. Herz, Y.J. Li, C. Borchers, P. Choi, D. Raabe, R. Kirchheim, Nanocrystalline Fe–C alloys produced by ball milling of iron and graphite, Acta Materialia 61(9) (2013) 3172-3185.
[23] H.A. Murdoch, C.A. Schuh, Estimation of grain boundary segregation enthalpy and its role in stable nanocrystalline alloy design, Journal of Materials Research 28(16) (2013) 2154-2163.
[24] K.A. Darling, M.A. Tschopp, B.K. VanLeeuwen, M.A. Atwater, Z.K. Liu, Mitigating grain growth in binary nanocrystalline alloys through solute selection based on thermodynamic stability maps, Computational Materials Science 84(Supplement C) (2014) 255-266.
[25] E. Nes, N. Ryum, O. Hunderi, On the Zener drag, Acta Metallurgica 33(1) (1985) 11-22.
[26] C. Schwarze, R. Darvishi Kamachali, I. Steinbach, Phase-field study of zener drag and pinning of cylindrical particles in polycrystalline materials, Acta Materialia 106(Supplement C) (2016) 59-65.
[27] W.B. Li, K.E. Easterling, The influence of particle shape on zener drag, Acta Metallurgica et Materialia 38(6) (1990) 1045-1052.
[28] J.W. Cahn, The impurity-drag effect in grain boundary motion, Acta Metallurgica 10(9) (1962) 789-798.
[29] M.I. Mendelev, D.J. Srolovitz, Impurity effects on grain boundary migration, Modelling and Simulation in Materials Science and Engineering 10(6) (2002) R79.
[30] I. Toda-Caraballo, C. Capdevila, G. Pimentel, C.G. De Andrés, Drag effects on grain growth dynamics, Computational Materials Science 68 (2013) 95-106.
[31] D. Amram, C.A. Schuh, Interplay between thermodynamic and kinetic stabilization mechanisms in nanocrystalline Fe-Mg alloys, Acta Materialia 144 (2018) 447-458.
[32] C.C. Koch, R.O. Scattergood, M. Saber, H. Kotan, High temperature stabilization of nanocrystalline grain size: Thermodynamic versus kinetic strategies, Journal of Materials Research 28(13) (2013) 1785-1791.
[33] M. Saber, H. Kotan, C. Koch, R. Scattergood, Thermal stability of nanocrystalline Fe–Cr alloys with Zr additions, Materials Science and Engineering: A 556 (2012) 664–670.
[34] P.R. Cantwell, M. Tang, S.J. Dillon, J. Luo, G.S. Rohrer, M.P. Harmer, Grain boundary complexions, Acta Materialia 62(Supplement C) (2014) 1-48.
[35] M. Tang, W.C. Carter, R.M. Cannon, Diffuse interface model for structural transitions of grain boundaries, Physical Review B 73(2) (2006) 024102.
[36] S.J. Dillon, M. Tang, W.C. Carter, M.P. Harmer, Complexion: A new concept for kinetic engineering in materials science, Acta Materialia 55(18) (2007) 6208-6218.
[37] T. Frolov, D.L. Olmsted, M. Asta, Y. Mishin, Structural phase transformations in metallic grain boundaries, Nature Communications 4(1) (2013) 1899.
[38] T. Meiners, T. Frolov, R.E. Rudd, G. Dehm, C.H. Liebscher, Observations of grain-boundary phase transformations in an elemental metal, Nature 579(7799) (2020) 375-378.
[39] B. Straumal, R. Valiev, O. Kogtenkova, P. Zieba, T. Czeppe, E. Bielanska, M. Faryna, Thermal evolution and grain boundary phase transformations in severely deformed nanograined Al–Zn alloys, Acta Materialia 56(20) (2008) 6123-6131.

[40] T.T. Sasaki, T. Ohkubo, Y. Takada, T. Sato, A. Kato, Y. Kaneko, K. Hono, Formation of non-ferromagnetic grain boundary phase in a Ga-doped Nd-rich Nd–Fe–B sintered magnet, Scripta Materialia 113 (2016) 218-221.
[41] S.J. Dillon, M.P. Harmer, Demystifying the role of sintering additives with "complexion", Journal of the European Ceramic Society 28(7) (2008) 1485-1493.
[42] J. Nie, J.M. Chan, M. Qin, N. Zhou, J. Luo, Liquid-like grain boundary complexion and sub-eutectic activated sintering in CuO-doped TiO2, Acta Materialia 130 (2017) 329-338.
[43] J. Luo, Liquid-like interface complexion: From activated sintering to grain boundary diagrams, Current Opinion in Solid State and Materials Science 12(5) (2008) 81-88.
[44] Y. Zu, G. Chen, X. Fu, K. Luo, C. Wang, S. Song, W. Zhou, Effects of liquid phases on densification of TiO2-doped Al2O3–ZrO2 composite ceramics, Ceramics International 40(3) (2014) 3989-3993.
[45] G.S. Rohrer, The role of grain boundary energy in grain boundary complexion transitions, Current Opinion in Solid State and Materials Science 20(5) (2016) 231-239.
[46] S.J. Dillon, M.P. Harmer, J. Luo, Grain boundary complexions in ceramics and metals: An overview, JOM 61(12) (2009) 38-44.
[47] A.K. Lawrence, A. Kundu, M.P. Harmer, C. Compson, J. Atria, M. Spreij, Influence of Complexion Transitions on Microstructure Evolution in Specialty Aluminas, Journal of the American Ceramic Society 98(4) (2015) 1347-1355.
[48] S.A. Bojarski, J. Knighting, S.L. Ma, W. Lenthe, M.P. Harmer, G.S. Rohrer, The Relationship between Grain Boundary Energy, Grain Boundary Complexion Transitions, and Grain Size in Ca-Doped Yttria, Materials Science Forum 753 (2013) 87-92.
[49] S.J. Dillon, M.P. Harmer, Relating Grain Boundary Complexion to Grain Boundary Kinetics II: Silica-Doped Alumina, Journal of the American Ceramic Society 91(7) (2008) 2314-2320.
[50] L. Feng, R. Hao, J. Lambros, S.J. Dillon, The influence of dopants and complexion transitions on grain boundary fracture in alumina, Acta Materialia 142 (2018) 121-130.
[51] S.J. Dillon, M.P. Harmer, Relating Grain-Boundary Complexion to Grain-Boundary Kinetics I: Calcia-Doped Alumina, Journal of the American Ceramic Society 91(7) (2008) 2304-2313.
[52] P.R. Cantwell, T. Frolov, T.J. Rupert, A.R. Krause, C.J. Marvel, G.S. Rohrer, J.M. Rickman, M.P. Harmer, Grain Boundary Complexion Transitions, Annual Review of Materials Research 50(1) (2020) 465-492.
[53] S.A. Bojarski, M.P. Harmer, G.S. Rohrer, Influence of grain boundary energy on the nucleation of complexion transitions, Scripta Materialia 88 (2014) 1-4.
[54] M. Tang, W.C. Carter, R.M. Cannon, Grain boundary order-disorder transitions, Journal of Materials Science 41(23) (2006) 7691-7695.
[55] N. Zhou, Z. Yu, Y. Zhang, M.P. Harmer, J. Luo, Calculation and validation of a grain boundary complexion diagram for Bi-doped Ni, Scripta Materialia 130 (2017) 165-169.
[56] P.R. Cantwell, S. Ma, S.A. Bojarski, G.S. Rohrer, M.P. Harmer, Expanding time–temperature-transformation (TTT) diagrams to interfaces: A new approach for grain boundary engineering, Acta Materialia 106 (2016) 78-86.
[57] J. Luo, Grain boundary complexions: The interplay of premelting, prewetting, and multilayer adsorption, Applied Physics Letters 95(7) (2009) 071911.
[58] P.L. Williams, Y. Mishin, Thermodynamics of grain boundary premelting in alloys. II. Atomistic simulation, Acta Materialia 57(13) (2009) 3786-3794.

[59] R. Brydson, S.C. Chen, F.L. Riley, S.J. Milne, X. Pan, M. Rüble, Microstructure and chemistry of intergranular glassy films in liquid-phase-sintered alumina, Journal of the American Ceramic Society 81(2) (1998) 369-379.
[60] H. Song, R.L. Coble, Morphology of Platelike Abnormal Grains in Liquid-Phase-Sintered Alumina, Journal of the American Ceramic Society 73(7) (1990) 2086-2090.
[61] W. Jo, D.-Y. Kim, N.-M. Hwang, Effect of Interface Structure on the Microstructural Evolution of Ceramics, Journal of the American Ceramic Society 89(8) (2006) 2369-2380.
[62] D.R. Clarke, On the Equilibrium Thickness of Intergranular Glass Phases in Ceramic Materials, Journal of the American Ceramic Society 70(1) (1987) 15-22.
[63] X. Shi, J. Luo, Grain boundary wetting and prewetting in Ni-doped Mo, Applied Physics Letters 94(25) (2009) 251908.
[64] J. Luo, V.K. Gupta, D.H. Yoon, H.M. Meyer, Segregation-induced grain boundary premelting in nickel-doped tungsten, Applied Physics Letters 87(23) (2005) 231902.
[65] J.D. Schuler, O.K. Donaldson, T.J. Rupert, Amorphous complexions enable a new region of high temperature stability in nanocrystalline Ni-W, Scr. Mater. 154 (2018) 49-53.
[66] S. Divinski, M. Lohmann, C. Herzig, B. Straumal, B. Baretzky, W. Gust, Grain-boundary melting phase transition in the Cu-Bi system, Physical Review B 71(10) (2005) 104104.
[67] J.D. Schuler, T.J. Rupert, Materials selection rules for amorphous complexion formation in binary metallic alloys, Acta Materialia 140(Supplement C) (2017) 196-205.
[68] A. Inoue, Stabilization of metallic supercooled liquid and bulk amorphous alloys, Acta Materialia 48(1) (2000) 279-306.
[69] A. Inoue, Stabilization of Supercooled Liquid and Opening-up of Bulk Glassy Alloys, Proceedings of the Japan Academy, Series B 73(2) (1997) 19-24.
[70] A. Khalajhedayati, Z. Pan, T.J. Rupert, Manipulating the interfacial structure of nanomaterials to achieve a unique combination of strength and ductility, Nature Communications 7 (2016) ncomms10802.
[71] A. Khalajhedayati, T.J. Rupert, High-Temperature Stability and Grain Boundary Complexion Formation in a Nanocrystalline Cu-Zr Alloy, JOM 67(12) (2015) 2788-2801.
[72] L. Lu, N.R. Tao, L.B. Wang, B.Z. Ding, K. Lu, Grain growth and strain release in nanocrystalline copper, Journal of Applied Physics 89(11) (2001) 6408-6414.
[73] S.K. Ganapathi, D.M. Owen, A.H. Chokshi, The kinetics of grain growth in nanocrystalline copper, Scripta Metallurgica et Materialia 25(12) (1991) 2699-2704.
[74] J.T. Zhao, J.Y. Zhang, L.F. Cao, Y.Q. Wang, P. Zhang, K. Wu, G. Liu, J. Sun, Zr alloying effect on the microstructure evolution and plastic deformation of nanostructured Cu thin films, Acta Materialia 132 (2017) 550-564.
[75] V. Turlo, T.J. Rupert, Grain boundary complexions and the strength of nanocrystalline metals: Dislocation emission and propagation, Acta Materialia 151 (2018) 100-111.
[76] C.M. Grigorian, T.J. Rupert, Thick amorphous complexion formation and extreme thermal stability in ternary nanocrystalline Cu-Zr-Hf alloys, Acta Materialia 179 (2019) 172-182.
[77] J. Luo, H. Wang, Y.-M. Chiang, Origin of Solid-State Activated Sintering in Bi2O3-Doped ZnO, Journal of the American Ceramic Society 82(4) (1999) 916-920.
[78] E. Jud, C.B. Huwiler, L.J. Gauckler, Sintering Analysis of Undoped and Cobalt Oxide Doped Ceria Solid Solutions, Journal of the American Ceramic Society 88(11) (2005) 3013-3019.

[79] O.K. Donaldson, T.J. Rupert, Amorphous Intergranular Films Enable the Creation of Bulk Nanocrystalline Cu–Zr with Full Density, Advanced Engineering Materials 21(9) (2019) 1900333.
[80] J.E. Ludy, T.J. Rupert, Amorphous intergranular films act as ultra-efficient point defect sinks during collision cascades, arXiv e-prints, 2015, p. arXiv:1506.06783.
[81] J.D. Schuler, C.M. Grigorian, C.M. Barr, B.L. Boyce, K. Hattar, T.J. Rupert, Amorphous intergranular films mitigate radiation damage in nanocrystalline Cu-Zr, Acta Materialia 186 (2020) 341-354.
[82] J.W. Gibbs, On the Equilibrium of Heterogeneous Substances, Transactions of the Connecticut Academy of Arts and Sciences 3 (1874-1878) 108-248, 343-542.
[83] N. Zhou, T. Hu, J. Huang, J. Luo, Stabilization of nanocrystalline alloys at high temperatures via utilizing high-entropy grain boundary complexions, Scripta Materialia 124 (2016) 160-163.
[84] N. Zhou, T. Hu, J. Luo, Grain boundary complexions in multicomponent alloys: Challenges and opportunities, Current Opinion in Solid State and Materials Science 20(5) (2016) 268-277.
[85] N. Zhou, J. Luo, Developing grain boundary diagrams for multicomponent alloys, Acta Materialia 91 (2015) 202-216.
[86] Y.C. Kim, J.C. Lee, P.R. Cha, J.P. Ahn, E. Fleury, Enhanced glass forming ability and mechanical properties of new Cu-based bulk metallic glasses, Materials Science and Engineering: A 437(2) (2006) 248-253.
[87] W.L. Johnson, Bulk Glass-Forming Metallic Alloys: Science and Technology, MRS Bulletin 24(10) (1999) 42-56.
[88] T.A. Baser, M. Baricco, Fe-based bulk metallic glasses with Y addition, Journal of Alloys and Compounds 434-435 (2007) 176-179.
[89] J. Wang, R. Li, N. Hua, T. Zhang, Co-based ternary bulk metallic glasses with ultrahigh strength and plasticity, Journal of Materials Research 26(16) (2011) 2072-2079.
[90] X.F. Zhang, H.X. Li, Z.Q. Jiang, S.H. Yi, Effect of Minor Si and Ag Additions on Glass-Forming Ability of Ti-Cu-Co-Zr-Sn-Be Bulk Metallic Glass, Materials Science Forum 688 (2011) 400-406.
[91] H. Men, S.J. Pang, T. Zhang, Glass-forming ability and mechanical properties of Cu50Zr50−xTix alloys, Materials Science and Engineering: A 408(1) (2005) 326-329.
[92] J. Schiøtz, K.W. Jacobsen, A Maximum in the Strength of Nanocrystalline Copper, Science 301(5638) (2003) 1357-1359.
[93] L. Lu, Y. Shen, X. Chen, L. Qian, K. Lu, Ultrahigh Strength and High Electrical Conductivity in Copper, Science 304(5669) (2004) 422.
[94] O.J. Kleppa, S. Watanabe, Thermochemistry of alloys of transition metals: Part III. Copper-silver, -titanium, -zirconium, and -hafnium at 1373 K, Journal of Electronic Materials 20(12) (1991) 391-401.
[95] I.A. Figueroa, H. Zhao, S. González, H.A. Davies, I. Todd, Bulk glass formability for Cu–Hf–Zr–Ag and Cu–Zr–Ag–Si alloys, Journal of Non-Crystalline Solids 354(47) (2008) 5181-5183.
[96] D. Qiao, A. Peker, Enhanced glass forming ability in Zr-based bulk metallic glasses with Hf Addition, Intermetallics 24 (2012) 115-119.
[97] P.R. Subramanian, D.E. Laughlin, The Cu-Hf (Copper-Hafnium) System, Bulletin of Alloy Phase Diagrams 9(1) (1988) 51-56.

[98] D. Arias, J.P. Abriata, Cu-Zr (Copper-Zirconium), Bulletin of Alloy Phase Diagrams 11(5) (1990) 452-459.
[99] L. Lutterotti, R. Vasin, H.-R. Wenk, Rietveld texture analysis from synchrotron diffraction images. I. Calibration and basic analysis, Powder Diffraction 29(1) (2014) 76-84.
[100] H.P. Klug, L.E. Alexander, X-Ray Diffraction Procedures for Polycrystalline and Amorphous Materials, John Wiley & Sons, Inc., New York, 1975.
[101] K.A. Darling, A.J. Roberts, Y. Mishin, S.N. Mathaudhu, L.J. Kecskes, Grain size stabilization of nanocrystalline copper at high temperatures by alloying with tantalum, Journal of Alloys and Compounds 573(Supplement C) (2013) 142-150.
[102] T. Chookajorn, C.A. Schuh, Nanoscale segregation behavior and high-temperature stability of nanocrystalline W–20at.% Ti, Acta Materialia 73 (2014) 128-138.
[103] S.-Y. Choi, S.-J.L. Kang, S.-Y. Chung, Abnormal Grain Growth and Intergranular Amorphous Film Formation in BaTiO3, Journal of the American Ceramic Society 90(2) (2007) 645-648.
[104] S.-H. Hong, D.-Y. Kim, Effect of Liquid Content on the Abnormal Grain Growth of Alumina, Journal of the American Ceramic Society 84(7) (2004) 1597-1600.
[105] H. Yang, L. Gao, G. Shao, R. Xu, P. Huang, Grain boundary glassy phase and abnormal grain growth of silicon nitride ceramics, Ceramics International 27(5) (2001) 603-605.
[106] S.J. Dillon, M.P. Harmer, Diffusion Controlled Abnormal Grain Growth in Ceramics, Materials Science Forum 558-559 (2007) 1227-1236.
[107] L. Takacs, Ball Milling-Induced Combustion in Powder Mixtures Containing Titanium, Zirconium, or Hafnium, Journal of Solid State Chemistry 125(1) (1996) 75-84.
[108] M. Hillert, Inhibition of grain growth by second-phase particles, Acta Metallurgica 36(12) (1988) 3177-3181.
[109] M. Guttmann, Equilibrium segregation in a ternary solution: A model for temper embrittlement, Surface Science 53(1) (1975) 213-227.
[110] H. Nielsen Ralph, G. Wilfing, Zirconium and Zirconium Compounds, Ullmann's Encyclopedia of Industrial Chemistry 39 (2010) 753-776.
[111] R. Tricot, The metallurgy and functional properties of hafnium, Journal of Nuclear Materials 189(3) (1992) 277-288.
[112] L. Xu, Y. Xiao, A. van Sandwijk, Z. Zhao, J. Li, Q. Xu, Y. Yang, Zirconium and hafnium separation with molten salt extraction in Sn–Cu–Zr–Hf and Cu–Zr–Hf alloy systems, Separation Science and Technology 51(10) (2016) 1664-1674.
[113] Y. Hu, T.J. Rupert, Atomistic modeling of interfacial segregation and structural transitions in ternary alloys, Journal of Materials Science 54(5) (2019) 3975-3993.
[114] M. Kapoor, T. Kaub, K.A. Darling, B.L. Boyce, G.B. Thompson, An atom probe study on Nb solute partitioning and nanocrystalline grain stabilization in mechanically alloyed Cu-Nb, Acta Mater. 126 (2017) 564-575.
[115] Z. Pan, T.J. Rupert, Formation of ordered and disordered interfacial films in immiscible metal alloys, Scripta Materialia 130 (2017) 91-95.
[116] M. Yoshitake, K. Yoshihara, Surface segregation of substrate element on metal films in film/substrate combinations with Nb, Ti and Cu, Surface and Interface Analysis 18(7) (1992) 509-513.
[117] N.Q. Vo, S.W. Chee, D. Schwen, X. Zhang, P. Bellon, R.S. Averback, Microstructural stability of nanostructured Cu alloys during high-temperature irradiation, Scripta Materialia 63(9) (2010) 929-932.

[118] L. Lutterotti, M. Bortolotti, G. Ischia, I. Lonardelli, H.R. Wenk, Rietveld texture analysis from diffraction images
Tenth European Powder Diffraction Conference, De Gruyter, Berlin, Boston, 2007, pp. 125-130.

[119] C. Suryanarayana, Mechanical alloying and milling, Progress in Materials Science 46(1) (2001) 1-184.

[120] G.S. Rohrer, “Introduction to Grains, Phases, and Interfaces—an Interpretation of Microstructure,” Trans. AIME, 1948, vol. 175, pp. 15–51, by C.S. Smith, Metallurgical and Materials Transactions A 41(5) (2010) 1063-1100.

[121] K. Okada, T. Sakuma, The Role of Zener's Pinning Effect on the Grain Growth in Al₂O₃-ZrO₂, Journal of the Ceramic Society of Japan 100(1160) (1992) 382-386.

[122] W. Xing, A.R. Kalidindi, C.A. Schuh, Preferred nanocrystalline configurations in ternary and multicomponent alloys, Scripta Materialia 127 (2017) 136-140.

[123] W. Xing, A. Kalidindi, D. Amram, C. Schuh, Solute Interaction Effects on Grain Boundary Segregation in Ternary Alloys, Acta Materialia 161 (2018).

[124] M.A. Atwater, K.A. Darling, A Visual Library of Stability in Binary Metallic Systems: The Stabilization of Nanocrystalline Grain Size by Solute Addition: Part 1, 2012.

[125] K.E.E. D.A. Porter, M. Sherif, Phase Transformations in Metals and Alloys (Revised Reprint), CRC Press, New York, 2009.

[126] L. Li, E.-B. Liu, Q.-F. Li, Z. Li, Non-equilibrium grain boundary cosegregation of Mo and P, Applied Surface Science 252(11) (2006) 3989-3992.

[127] H. Erhart, H.J. Grabke, Equilibrium segregation of phosphorus at grain boundaries of Fe–P, Fe–C–P, Fe–Cr–P, and Fe–Cr–C–P alloys, Metal Science 15(9) (1981) 401-408.

[128] W. Yu-Qing, C.J. McMahon, Interaction of phosphorus, carbon, manganese, and chromium in intergranular embrittlement of iron, Materials Science and Technology 3(3) (1987) 207-216.

[129] J.R. Rice, J.-S. Wang, Embrittlement of interfaces by solute segregation, Materials Science and Engineering: A 107 (1989) 23-40.

[130] Z.P. Lu, C. Liu, A New Glass-Forming Ability Criterion for Bulk Metallic Glasses, Acta Materialia 50 (2002) 3501-3512.

[131] W.B. Sheng, Correlations between critical section thickness and glass-forming ability criteria of Ti-based bulk amorphous alloys, Journal of Non-Crystalline Solids 351(37) (2005) 3081-3086.

[132] J. Shen, Y.J. Huang, J.F. Sun, Plasticity of a TiCu-based bulk metallic glass: Effect of cooling rate, Journal of Materials Research 22(11) (2007) 3067-3074.

[133] W. Fu, Y. Sun, W. Zhang, The Effect of Cooling Rate on Microstructure and Mechanical Properties of Zr-Based Bulk Metallic Glasses, Advances in Materials Science and Engineering 2013 (2013) 826758.

[134] J. Luo, X. Shi, Grain boundary disordering in binary alloys, Applied Physics Letters 92(10) (2008) 101901.

[135] I.A. Figueroa, J.D. Plummer, G.A. Lara-Rodriguez, O. Novelo-Peralta, I. Todd, Metallic glass formation in the binary Cu–Hf system, Journal of Materials Science 48(4) (2013) 1819-1825.

[136] D. Wang, Y. Li, B.B. Sun, M.L. Sui, K. Lu, E. Ma, Bulk metallic glass formation in the binary Cu–Zr system, Applied Physics Letters 84(20) (2004) 4029-4031.

[137] V.I. Tkatch, A.I. Limanovskii, S.N. Denisenko, S.G. Rassolov, The effect of the melt-spinning processing parameters on the rate of cooling, Materials Science and Engineering: A 323(1) (2002) 91-96.
[138] Z. Pan, T.J. Rupert, Effect of grain boundary character on segregation-induced structural transitions, Physical Review B 93(13) (2016) 134113.
[139] E.W. Hart, Grain Boundary Phase Transformations, in: H. Hu (Ed.), The Nature and Behavior of Grain Boundaries: A Symposium held at the TMS-AIME Fall Meeting in Detroit, Michigan, October 18–19, 1971, Springer US, New York, NY, 1972, pp. 155-170.
[140] R. Kirchheim, Reducing grain boundary, dislocation line and vacancy formation energies by solute segregation. I. Theoretical background, Acta Materialia 55(15) (2007) 5129-5138.
[141] N. Chen, L. Martin, D.V. Luzguine-Luzgin, A. Inoue, Role of Alloying Additions in Glass Formation and Properties of Bulk Metallic Glasses, Materials (Basel) 3(12) (2010) 5320-5339.
[142] M. Tang, W.C. Carter, R.M. Cannon, Grain Boundary Transitions in Binary Alloys, Physical Review Letters 97(7) (2006) 075502.
[143] X. Shi, J. Luo, Developing grain boundary diagrams as a materials science tool: A case study of nickel-doped molybdenum, Physical Review B 84(1) (2011) 014105.
[144] J. Basu, S. Ranganathan, Glass forming ability and stability: Ternary Cu bearing Ti, Zr, Hf alloys, Intermetallics 17(3) (2009) 128-135.
[145] A.I. C. Suryanarayana, Bulk Metallic Glasses, 22 November 2017 ed.2017.
[146] P. Yu, H.Y. Bai, W.H. Wang, Superior glass-forming ability of CuZr alloys from minor additions, Journal of Materials Research 21(7) (2006) 1674-1679.
[147] H. Wang, H. M. Fu, H. F. Zhang, Z. Q. Hu, A Practical Thermodynamic Method to Calculate the Best Glass-forming Composition for Bulk Metallic Glasses, 8(2) (2007) 171.
[148] S.F. Guo, Y.Y. Sun, J. Pan, L. Liu, The effect of Hf substitution for Zr on glass forming ability and magnetic property of FeCoZrMoBAlY bulk metallic glasses, Journal of Alloys and Compounds 458(1) (2008) 214-217.
[149] X.F. Zhang, R. Wang, Short-range order in nanoscale amorphous intergranular films in liquid-phase sintered silicon carbide, Applied Physics Letters 89(21) (2006) 211902.
[150] M. Baram, S.H. Garofalini, W.D. Kaplan, Order in nanometer thick intergranular films at Au–sapphire interfaces, Acta Materialia 59(14) (2011) 5710-5715.
[151] Z. Pan, T.J. Rupert, Spatial variation of short-range order in amorphous intergranular complexions, Computational Materials Science 131 (2017) 62-68.